UTS UNIVERSITY OF TECHNOLOGY SYDNEY

Light field modulation and orthogonal illumination strategies for volumetric imaging

by Sitong Wu
Thesis submitted in fulfilment of the requirements for
the degree of

Doctor of Philosophy

under the supervision of Dayong JIn

University of Technology Sydney
Faculty of Science

March 2025

Certificate of Original Authorship

I, Sitong Wu, declare that this thesis is submitted in fulfilment of the requirements for the award of Doctor of Philosophy, in the School of Mathematical and Physical Sciences, Faculty of Science, at the University of Technology Sydney.

This thesis is wholly my own work unless otherwise reference or acknowledged. In addition, I certify that all information sources and literature used are indicated in the thesis.

This document has not been submitted for qualifications at any other academic institution.

This research is supported by the Australian Government Research Training Program.

Signature: Production Note:
Signature removed prior to publication.

Date: 31/March

Table of contents

1 Introduction

1.1 Light Field Modulation Techniques in Microscopic Imaging

Light field modulation is one of the most important techniques in modern microscopy for volumetric imaging of different scales of biological structures[1-4]. This technique is used to achieve high spatiotemporal resolution[4] and large-volume field-of-view imaging[5], which are primary goals in advanced microscopy. Light field modulation relies on controlling the distribution of light properties. By modulating the spatial, temporal, spectral, and polarization properties of light as shown in ***Figure 1-1***, researchers can bypass traditional limitations of resolution, increase signal-to-noise ratio (SNR), or record subtle biological dynamics in three-dimensional (3D) space[6, 7]. Light field modulation technology is the basis for breakthroughs such as super-resolution microscopy[8], light-sheet microscopy, and time-resolved imaging[9, 10], and it makes it easier to achieve greater insight into multi-scale bio-imaging[11].

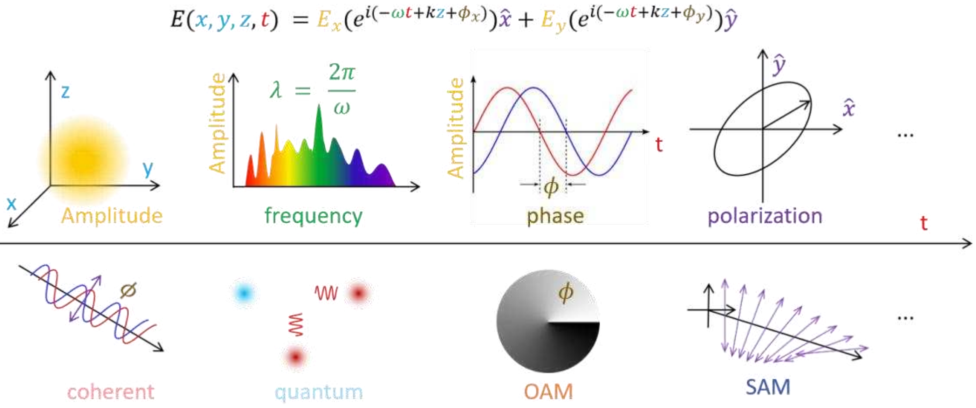

Figure 1-1. Schematic Diagram of the Basic Properties of Light. Orbital angular momentum (OAM), and spin angular momentum (SAM).

Light field modulation technology can be categorized into near-field and far-field approaches[12, 13]. Near-field modulation typically involves evanescent waves, surface plasmon polaritons, and localized optical interactions within sub-wavelength distances. Far-field modulation includes structured illumination, light-sheet microscopy, and spatial light modulation, where light travels as radiative waves and can be modulated for longer distances. In this paper, I primarily discuss far-field modulation for the microscopic imaging of different spatial scales. These far-field modulation schemes enable high-resolution, 3D imaging of biological structures and make it possible for advancements in multi-scale volumetric microscopy.

One important approach to light field modulation involves precisely controlling the spatial distribution of light intensity[14], along with parameters such as polarization[15], phase[16], SAM and OAM[17]. By encoding these properties in space, the interaction between light and matter can be selectively adjusted, enabling enhanced control over excitation, scattering, and absorption processes in imaging, optical manipulating, optical communication, optical sensing, and so on. In fluorescence microscopy, spatially modulated excitation patterns, such as structured illumination, Bessel beams, and optical lattices, are used to encode fluorescence intensity distributions, selectively exciting specific cellular structures and improving contrast, resolution, and depth penetration in highly scattering biological environments. Additionally, by modulating the polarization of the light field, it becomes possible to measure the anisotropy of fluorescent dipoles, thereby revealing the spatial orientation of subcellular-level fine structures[18]. Phase modulation of the light field has two main applications. The first is in adaptive optics, where correcting wavefront distortions reduces the effects of diffraction and scattering on imaging accuracy. The second is label-free imaging, in which phase variations caused by the sample's refractive index distribution enable three-dimensional reconstruction of the sample's structure. Beyond microscopy, spatially modulated light fields are also applied in optical manipulation, such as holographic optical tweezers and vortex optical tweezers; quantitative measurements at microscopic scales, such as angular momentum measurement; optical communication, including structured light modulation communication; and quantum information technologies, such as encoding information using entangled photon pairs.

A second primary way of modulating the light field is temporal modulation, where the time-domain characteristics of the light field are altered. Temporal modulation is widely applied in modalities such as fluorescence lifetime imaging microscopy (FLIM) and time-gated imaging, where the time-dependent response of light when interacting with matter is quantified and interpreted. By leveraging fluorescence lifetime as another parameter beyond spectral information, scientists are capable of resolving imaging signals in the spatial domain and, hence, revealing alterations in the microenvironment of biological samples[19]. Ultra-fast spectroscopic imaging also employs pulsed lasers to probe light-matter interactions on femtosecond and picosecond time scales. Pump-probe spectroscopy[20] and time-resolved transient absorption[21] imaging allow scientists to capture real-time snapshots of ultra-fast electron transitions, vibrational relaxation, and energy transfer in materials. By temporally modulating the light field, one can uncover time-domain characteristics of light-matter interactions (e.g., fluorescence lifetime) and, through modalities such as ultrashort pulse modulation, enable the detection of ultra-fast processes.

Most of the light field modulation schemes in microscopy inherently integrate spatial and temporal control, allowing for the manipulation of light in 4D. Spatial modulation is typically combined with temporal variations, enabling structured illumination patterns to change over time, while time-domain modulation is often synchronized with spatial scanning to achieve a spatial distribution of time-domain properties. For static samples, spatiotemporal modulation of the light field can be interchangeable. For example, spatial intensity modulation can be achieved through temporal integration, a principle commonly used in light sheet illumination and other microscopic imaging techniques. In the dynamic imaging of biological samples, researchers must consider the impact of sample movement on time-series data, balancing the trade-off between spatial and temporal resolution. Additionally, in ultrashort pulse research, the optical pulse envelope exists and interacts in a tightly coupled manner across both temporal and spatial dimensions, typically spanning durations from picoseconds (10^{-12} s) to femtoseconds (10^{-15} s). Under these conditions, temporal modulators are unable to keep pace with the speed of pulse lasers. Therefore, one can utilize the spatiotemporal coupling properties, employing dispersive optical elements in the spatial domain to manipulate the pulse spectrum, thereby controlling the temporal distribution of the optical field. A typical implementation is the 4f system[22], as illustrated in the ***Figure 1-2***. Through spatiotemporal coupling modulation, one can generate spatiotemporally non-diffracting light sheets, vortex envelopes, and other advanced optical fields, offering significant potential as breakthrough technologies for next-generation microscopy imaging[23, 24].

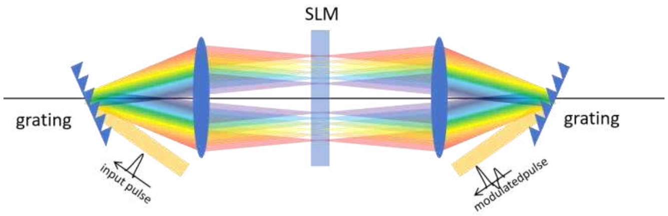

Figure 1-2. Schematic diagram of the system for modulating the temporal profile of laser pulses using a spatial light modulator.

Light field modulation can be precisely designed to accommodate different spatial and temporal scales in biological imaging. Across spatial dimensions, it enables high-resolution imaging from single cells to organoids and even small animals through structured illumination, adaptive optics, light-sheet microscopy, and multi-photon excitation, ensuring optimal resolution, penetration depth, and contrast. On the temporal scale, molecular activities, fluorescence lifetimes, and biological processes at different time scales from nanoseconds to milliseconds can be obtained through temporal or frequency-domain light field modulation. By integrating spatiotemporal control, light field modulation advances the development of multi-scale imaging technologies, enabling the capture of structural and functional biological information based on user requirements. The classification of microscopic imaging techniques based on light field modulation can be seen in ***Figure 1-3***.

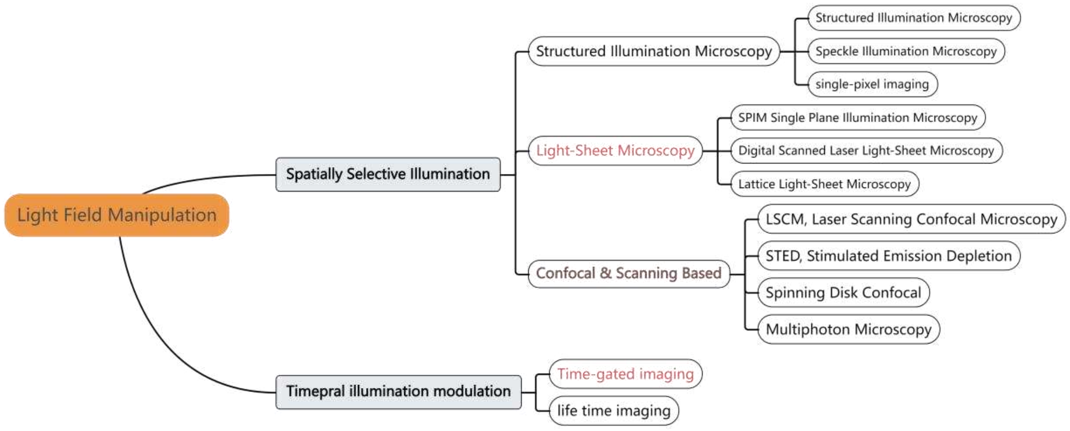

Figure 1-3. Light field modulation strategies in modern microscopes.

In this chapter, I primarily discuss spatiotemporal control principles, methods, and devices used for light field modulation to achieve designed illumination. This includes techniques such as structured illumination, light-sheet illumination, and dynamically adaptive beam shaping, which are designed to enhance contrast, resolution, and imaging efficiency across different spatial and temporal scales. I also explore the applicable imaging scales, ranging from macroscopic tissue imaging to high-resolution subcellular microscopy. Additionally, I introduce several microscopic imaging techniques based on light field modulation, including super-resolution fluorescence microscopy, high-speed volumetric imaging, and fiber encoded imaging.

In this section, I primarily consider transparent samples and disregard refractive index variations. The absorption, diffraction, and scattering effects caused by the sample's refractive index distribution are typically addressed in adaptive optics and other label-free imaging techniques. When these effects become significant in large-scale imaging, such as organoid imaging and deep tissue imaging, adaptive optical methods or longer wavelengths are employed. Additionally, the refractive index distribution also reflects the internal structure of the sample, which will be discussed later in the context of label-free imaging. Furthermore, time-gated techniques play a crucial role in selectively capturing fluorescence signals and minimizing background interference, enhancing contrast and resolution in dynamic imaging applications. These techniques, often combined with each other enable improved depth sectioning and functional imaging in complex biological systems.

1.2 Spatial-temporal Light Field Modulation

1.2.1 Properties of Spatial Light Field

The concept of the light field in computational imaging was first introduced by computer vision researchers, notably E. H. Adelson and J. R. Bergen in 1991[25], who defined the Plenoptic Function $L(x, y, z, \theta, \phi, \lambda, t)$ as a seven-dimensional representation of light, incorporating spatial position, incident angles, phase, wavelength, and time. While later works proposed adding dimensions such as polarization or OAM, it is important to distinguish between the "light field" as a radiometric function and the "optical field," which is fundamentally described by complex amplitude, polarization, and frequency (or time). OAM, for example, arises from phase modulation and is not an independent degree of freedom. Extensions beyond the classical dimensions are useful for specific applications but should be interpreted with care.

A spatial optical field is a distribution of electromagnetic waves in space, characterized by amplitude, phase, polarization, wavefront curvature, and spatial coherence. These properties define how light propagates, interacts with matter, and is manipulated in applications such as imaging, optical communication, and wavefront shaping.

The electric field of a monochromatic optical wave propagating along the z-axis in space is represented as:

$$\mathbf{E}(x,y,z,t) = E_x e^{i(-\omega t+kz+\phi_x)}\hat{x} + E_y e^{i(-\omega t+kz+\phi_y)}\hat{y} \tag{1-1}$$

Where:

E_x, E_y are the amplitudes of the electric field components in the x and y directions.

ϕ_x, ϕ_y are the phases of each component.

$\hat{x}$, $\hat{y}$ are the unit vectors defining the polarization plane.

$k = \frac{2\pi}{\lambda}$ is the wavenumber.

ω is the angular frequency of light.

Coherence describes the ability of an optical wave to maintain a well-defined phase relationship over time and space. It is a fundamental property of light that influences interference, diffraction, and imaging systems. Coherence is classified into temporal coherence (correlation in time) and spatial coherence (correlation across different points in space). The coherence time τ_c is the time over which the phase correlation is maintained, given by:

$$\tau_c = \frac{1}{\Delta \upsilon} \tag{1-2}$$

Where $\Delta \upsilon$ is the spectral bandwidth of the source. The coherence length L_c is the distance a wave travels before losing phase correlation:

$$L_c = \frac{c}{\Delta \upsilon} \tag{1-3}$$

Where c is the speed of light. A perfectly monochromatic wave ($\Delta \upsilon = 0$) has infinite coherence time, but real sources have finite coherence. Coherent light forms interference fringes in space when the following conditions are met:

(1) Stable Phase Relationship – The interfering waves must have a constant phase difference over time.

(2) Same or Nearly Identical Wavelengths – The light sources should have the same frequency or a narrow bandwidth to maintain temporal coherence.

(3) Same Polarization Component – The interfering waves must have at least one common polarization component to ensure effective interference.

An implicit condition is that only beams from the same source can satisfy the above conditions. The frequency and phase mismatches and variations in non-coherent beams will disrupt stable interference, causing the interference fringes to disappear.

For two waves E_1 and E_2 interfering at the same point, the total optical field is:

$$E_{\text{total}} = E_1 + E_2 = A_1 e^{i\phi_1} + A_2 e^{i\phi_2} \tag{1-4}$$

$$\begin{aligned} I &= |E_{\text{total}}|^2 \\ &= \left|A_1 e^{i\phi_1} + A_2 e^{i\phi_2}\right|^2 \\ &= A_1^2 + A_2^2 + 2A_1A_2\cos(\Delta\phi) \end{aligned} \tag{1-5}$$

For fully coherent light, the polarization state can be described using a Jones vector:

$$\boldsymbol{E} = \begin{bmatrix} \boldsymbol{E}_x e^{i\phi_x} \\ \boldsymbol{E}_y e^{i\phi_y} \end{bmatrix} \tag{1-6}$$

1.2.2 Computational Methods for Light Field Propagation

Far-field spatial light field modulation is based on the principles of light field propagation. By modulating the known phase and intensity distribution of the initial light field, the light field distribution at a specific spatial position after propagation can be calculated. The methods for light field propagation and their applicable ranges are shown in ***Table 1-1***.

Table 1-1 Methods for calculating light field propagation.

Method	**Suitable Propagation Range**	**Common Applications**
Fresnel Diffraction	Intermediate-range, paraxial approximation	Lens-based imaging, structured illumination
Fraunhofer Diffraction	Far-field, large observation distance	Fourier optics, holography
Rayleigh-Sommerfeld Diffraction	Near-field to intermediate-range, no paraxial assumption	Accurate modeling of diffraction, wavefront reconstruction
Angular Spectrum Method	Near-field and far-field, wavefront shaping	Phase modulation, adaptive optics
Beam Propagation Method (BPM)	Waveguides, optical fibers, gradual refractive index variations	Optical fiber design, integrated photonics
Finite-Difference Time-Domain (FDTD) / Finite Element Method (FEM)	Subwavelength-scale, complex optical structures	Full-wave electromagnetic simulations, nano-optics

For far-field light field propagation, we primarily use the angular spectrum method and the Fresnel method.

1.2.2.1 Fresnel Diffraction Propagation

Fresnel diffraction is an approximation of wave propagation derived from the Huygens-Fresnel principle[26]. It is valid for near-field diffraction, where the distance z satisfies the Fresnel approximation conditions:

$$z \gg \frac{(x-x_0)^2+(y-y_0)^2}{\lambda} \tag{1-7}$$

The Fresnel diffraction integral describes how an initial wavefront propagates to a distance z can be calculated as:

$$U(x,y,z) = \frac{e^{ikz}}{i\lambda z} \iint U(x_0,y_0,0) e^{\frac{ik}{2z}[(x-x_0)^2-(y-y_0)^2]} dx_0 dy_0 \tag{1-8}$$

Where:

$U(x_0,y_0,0)$ is the wavefront at the initial plane,

$U(x,y,z)$ is the propagated wavefront at distance,

k is the wave number,

λ is the wavelength.

In Fourier optics, the Fresnel diffraction integral can be rewritten using the Fourier transform:

$$U(x,y,z) = \mathcal{F}^{-1}[\mathcal{F}[U(x_0,y_0,0)] \cdot H_{\text{Fresnel}}(f_x,f_y,z)] \tag{1-9}$$

Where the Fresnel transfer function is:

$$H_{\text{Fresnel}}(f_x,f_y,z) = e^{ikz} e^{-i\pi\lambda z(f_x+f_y)} \tag{1-10}$$

In the equation, f_x and f_y represent the spatial frequencies in the x and y directions, respectively.

1.2.2.2 Angular Spectrum Propagation

The angular spectrum method is a more general approach to wave propagation, applicable to both near-field and far-field cases[27]. It represents the wavefront as a superposition of plane waves, each characterized by a spatial frequency component (f_x,f_y).

Using the Fourier transform, the propagation of a wavefront is given by:

$$U(x,y,z) = \mathcal{F}^{-1}[\mathcal{F}[U(x_0,y_0,0)] \cdot H_{AS}(f_x,f_y,z)] \tag{1-11}$$

where the angular spectrum transfer function is:

$$H_{\text{AS}}(f_x,f_y,z) = e^{ik\sqrt{1-(\lambda f_x)^2-(\lambda f_y)^2 \cdot z}} \tag{1-12}$$

The angular spectrum method accurately models wavefront curvature and evanescent waves, making it suitable for:

(1) High numerical aperture (NA) optical systems,

(2) Short propagation distances,

(3) Heterogeneous media simulations.

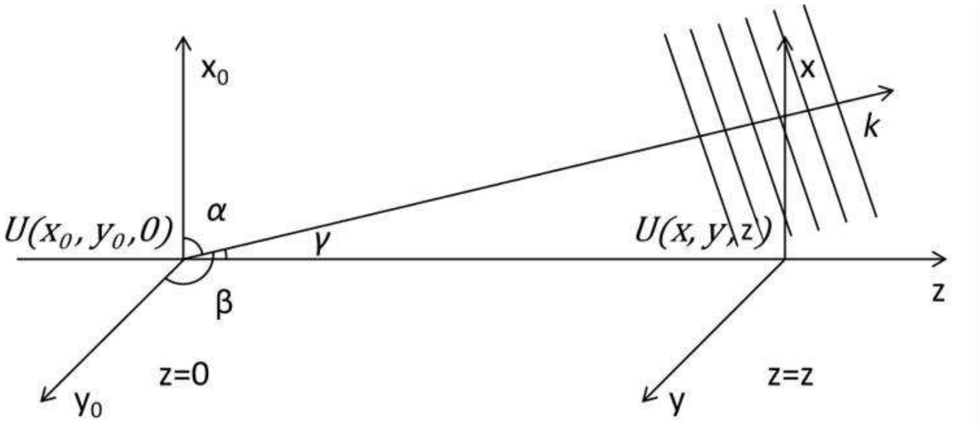

Figure 1-4. Propagation of Complex Amplitude in Free Space.

This method provides an exact solution to the Helmholtz equation without paraxial approximations, unlike Fresnel diffraction.

1.2.3 Devices for spatial Light field Manipulation

Since light propagation can be computationally modeled, manipulating the initial light field provides a direct means of controlling its evolution in space and time. By precisely modulating parameters such as phase, amplitude, and polarization at the source, it is possible to tailor the propagation characteristics, enhance imaging resolution, correct aberrations, and optimize energy delivery in complex environments.

Modern optics has developed a range of devices to achieve this level of control, enabling advanced applications in imaging, display technologies, optical computing, and holography. Programmable light field control devices, including SLMs (LC-SLM, DMD(Digital Micromirror Device)), DM(Deformable Mirror), etc., allow for flexible control of light field distribution, thereby achieving complex illumination or dynamic modulation of the light field. Static light field modulation devices include lenses, mirrors, prisms, polarization elements, phase plates, masks, diffractive devices, waveguide devices, and metasurfaces. Once designed, these static devices can achieve fixed light field modulation functions.

1.2.3.1 Programmable Spatial Light Modulators

SLMs[28] primarily refer to devices capable of spatial encoding of wavefronts, including two types: liquid crystal-based and micro-mirror-based. Below, I introduce the diverse applications of spatial light modulation based on these two types of devices.

A. Liquid Crystal Spatial Light Modulator (LC-SLM)

Phase Modulation Based on Liquid Crystal

The principle of liquid crystal light modulation is primarily based on the anisotropy of liquid crystal molecules and the electro-optic effect. When an external electric field is applied to the liquid crystal molecules, their orientation changes, thereby affecting the propagation characteristics of light, such as phase, amplitude, or polarization state. Liquid crystal light modulation is typically achieved using an LC-SLM to control the wavefront or intensity of the incident light.

When an electric field is applied to the liquid crystal layer, the liquid crystal molecules undergo realignment, causing the optical axis direction to change, thereby altering the effective refractive index n_{eff}.

Phase delay formula:

$$\Delta\phi = \frac{2\pi d}{\lambda}(n_{eff} - n_o) \tag{1-13}$$

Where:

d is the thickness of the liquid crystal layer

λ is the wavelength of the incident light

n_{eff} is the effective refractive index under the applied electric field

n_o is the original refractive index

By adjusting the applied voltage, n_{eff} can be dynamically controlled, thereby achieving phase modulation.

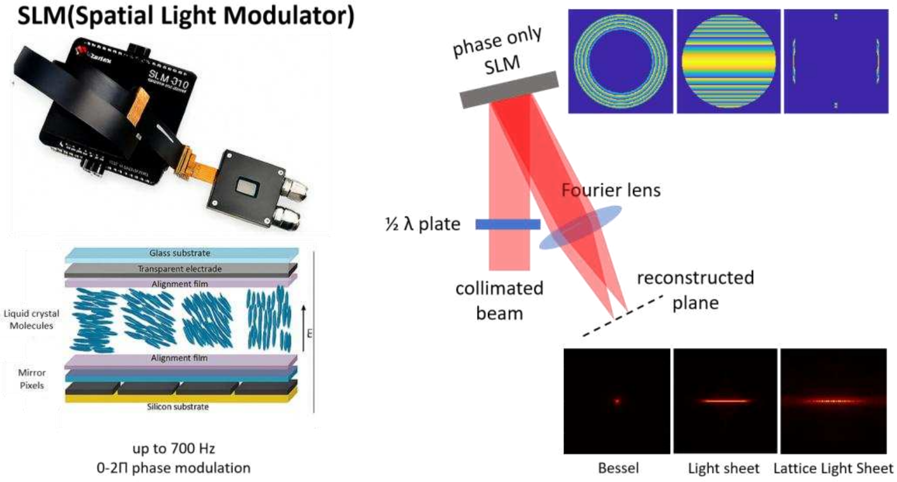

Figure 1-5. Structure and Optical Field Modulation Method of a Phase-Only SLM.

Intensity Modulation Based on Liquid Crystal

The phase modulation of the LC-SLMs only affects linearly polarized light in a specific direction. In ***Figure 1-5***, the half-wave plate is used to align the polarization direction with the modulation direction of the SLM. LC-SLMs are categorized into complex amplitude modulators and pure phase modulators. Complex amplitude modulation is relatively straightforward in intensity control. It typically employs a dual-layer liquid crystal structure, where one layer modulates the phase while the other adjusts the transmittance to control the amplitude of the optical field. The modulation optical path of the amplitude-type spatial light modulator (SLM) is shown in ***Figure 1-6***.

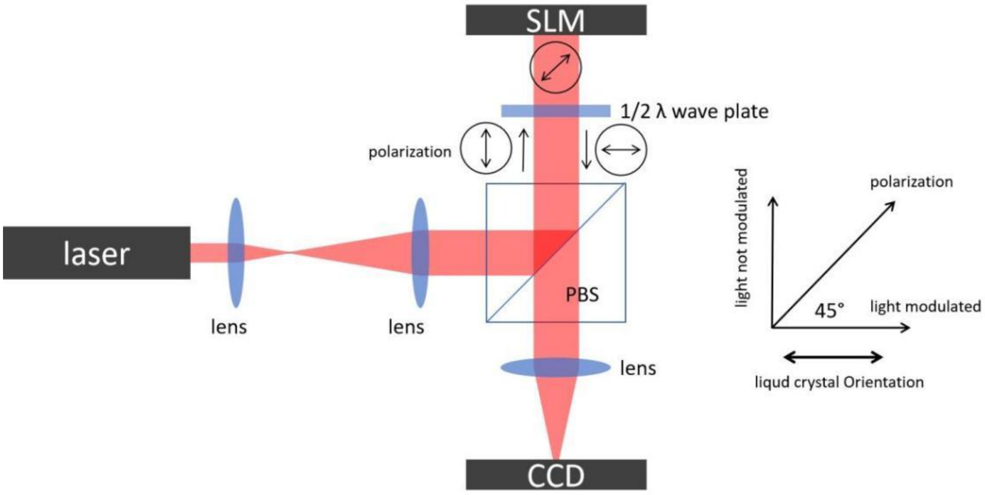

Figure 1-6. Optical Path Design of an Intensity-Modulation SLM.

I aim to modulate the optical field's all characteristics, with the most fundamental complex amplitude attributes being amplitude and phase. Typically, the SLMs I use are pure phase modulators, which cannot directly modulate amplitude. Some researchers have employed cascaded SLMs to achieve simultaneous amplitude and phase modulation, but this approach is both costly and systemically complex. Consequently, several complex amplitude modulation methods based on a single pure phase SLM have been developed[29].

Computational Holographic Imaging Method

The computational holographic imaging method, such as the Gerchberg–Saxton(GS)[30] algorithm, enables the generation of a desired complex amplitude distribution at the target plane by iteratively computing the corresponding phase distribution on a phase-only SLM. Since the propagation function and target optical field are known, the required complex amplitude on the SLM can be inferred. However, as the SLM can only modulate phase, the amplitude component is discarded, and the phase is used to compute the propagated optical field.

To optimize modulation, only the optical field within the field of view (FOV) is controlled, while iterative variations are accumulated outside this region. In each iteration, the propagated optical field within the FOV is replaced with the desired target field before continuing the process, leading to the formation of the intended optical distribution. The algorithm flowchart is shown in the Figure 1-7.

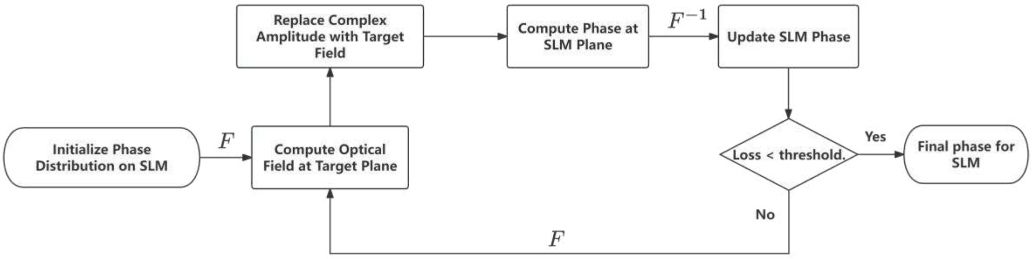

Figure 1-7. Process of Calculating the Required Phase for Complex Amplitude Modulation Using the GS Method.

This method is flexible and allows for both amplitude and phase modulation using a single phase-only SLM. However, it requires multiple iterations, making it computationally intensive, and The phase reconstruction is not sufficiently accurate. Despite these challenges, it remains a widely used approach in holographic imaging and wavefront shaping due to its adaptability and effectiveness in generating complex optical fields.

Holographic Grating Method

The complex amplitude of the optical field can be expressed as:

$$E = Ae^{i\phi} \tag{1-14}$$

Where:

A represents the amplitude of the optical field.

ϕ represents the phase of the optical field.

The principle of the holographic grating method is based on the interference fringes generated by the superposition of a plane wave and the target optical field. The grating records both the phase information and intensity distribution of the target optical field. When the reference plane wave is incident on the holographic grating again, the first-order diffraction reconstructs the target optical field. The transmittance function of the grating can be expressed as[31]:

$$H(x,y) = \frac{1}{2} - \frac{1}{2}\mathrm{sign}[\cos(\pi\Phi + 2\pi G) - \cos(\pi U)] \tag{1-15}$$

Where:

G represents the spatial frequency of the grating.

The sign function is used to generate a binary transmission pattern. The cosine terms introduce a periodic carrier frequency to encode the desired optical field properties. To properly encode the target amplitude and phase into the SLM, the transformation follows:

$$U = \frac{arcsin(|A|)}{\pi}, \quad \Phi = \frac{\Phi}{\pi} \tag{1-16}$$

Where:

Amplitude Encoding: The function $arcsin(|A|)$ maps amplitude values onto a phase-only modulation domain.

Phase Encoding: The phase Φ is normalized to a scale compatible with SLM constraints.

Macro-pixel Method

The Macro-pixel Method is a technique for complex amplitude modulation using a single phase-only SLM. Its core idea is to group the SLM pixels into small regions, called Macro-pixels, and utilize phase encoding within these regions to simultaneously control both amplitude and phase[32].

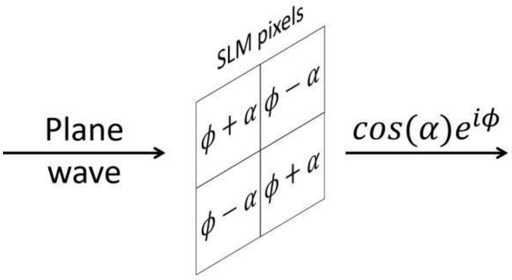

Figure 1-8. Macro-pixel method for complex wave modulation.

We can decompose complex amplitude into the superposition of two pure phase functions:

$$A = cos(\alpha) \tag{1-17-1}$$

$$\mathrm{E}_1 = e^{i(\phi+\alpha)} \tag{1-17-2}$$

$$\mathrm{E}_2 = e^{i(\phi-\alpha)} \tag{1-17-3}$$

From the above equation, I can merge four pixels into a single Macro pixel, with phases $\phi+\alpha$ and $\phi-\alpha$ loaded diagonally. Where ϕ is the phase to be loaded, and α is obtained by calculating $arccos(A)$. The actual phase loaded onto the SLM is shown in the Figure 1-8. The synthesized Macro pixel can simultaneously achieve both amplitude and phase modulation, but it reduces the pixel resolution of the SLM.

Blazed Grating Diffraction Method

The blazed grating diffraction method achieves intensity modulation by adjusting the blaze angle, which controls the diffraction efficiency in different regions. By varying the blaze angle, different areas of the light field can be assigned distinct diffraction efficiencies, effectively modulating the light intensity.

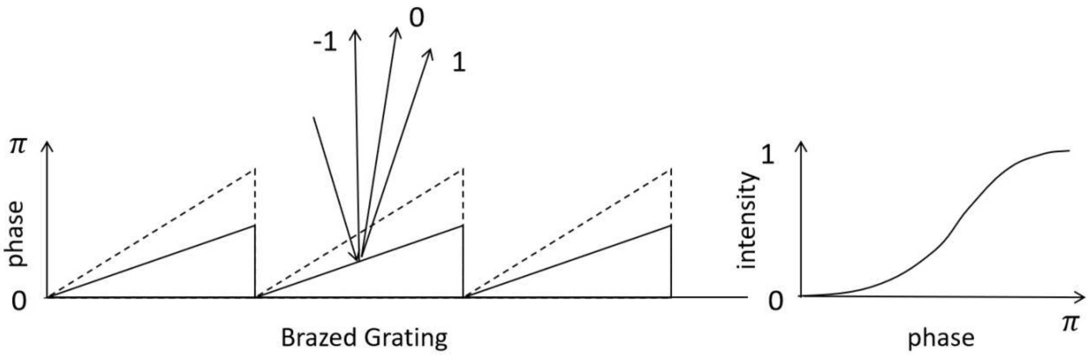

Figure 1-9. On the left is a schematic diagram of the blazing grating phase loaded onto the SLM, and on the right is a cosine curve illustrating the variation of the first-order diffraction intensity with the grating phase.

Other Modulation Based on Liquid Crystal

In addition to amplitude and phase modulation, LC-SLMs enable various advanced modulation techniques, including:

Polarization Modulation via polarizing beam splitter (PBS) Splitting: By using a PBS, the incident light beam can be split into two orthogonally polarized components. Although the LC-SLM can only modulate light in a single polarization direction, we can obtain orthogonal polarization modulation by rotating the polarization of the beam after modulation. The LC-SLM modulates the phase of one or both components, enabling controlled polarization modulation. This technique is widely used in polarization holography, optical encryption, and adaptive optics.

OAM Modulation: Liquid crystal devices can generate and manipulate vortex beams carrying OAM by applying helical phase masks or forked gratings. By encoding different topological charges on the LC-SLM, various OAM modes can be created, making this method useful in optical communication, quantum optics, and high-resolution microscopy.

SLM Zero-Order Diffraction Problem

SLMs, especially LC-SLMs, often suffer from zero-order diffraction, which appears as an undesired bright spot at the center of the diffraction pattern. This occurs due to:

(1) Unmodulated background light passing through the system.

(2) Imperfect phase encoding, where parts of the light field remain unaffected.

(3) SLM pixel structure, which introduces residual zero-order components.

Methods to Suppress Zero-Order Diffraction

There are several methods to suppress zero-order diffraction by superimposing a blazed grating onto the phase modulation pattern as shown in ***Figure 1-10***. This shifts the diffracted orders away from the zero-order position, effectively redirecting the energy into higher diffraction orders.

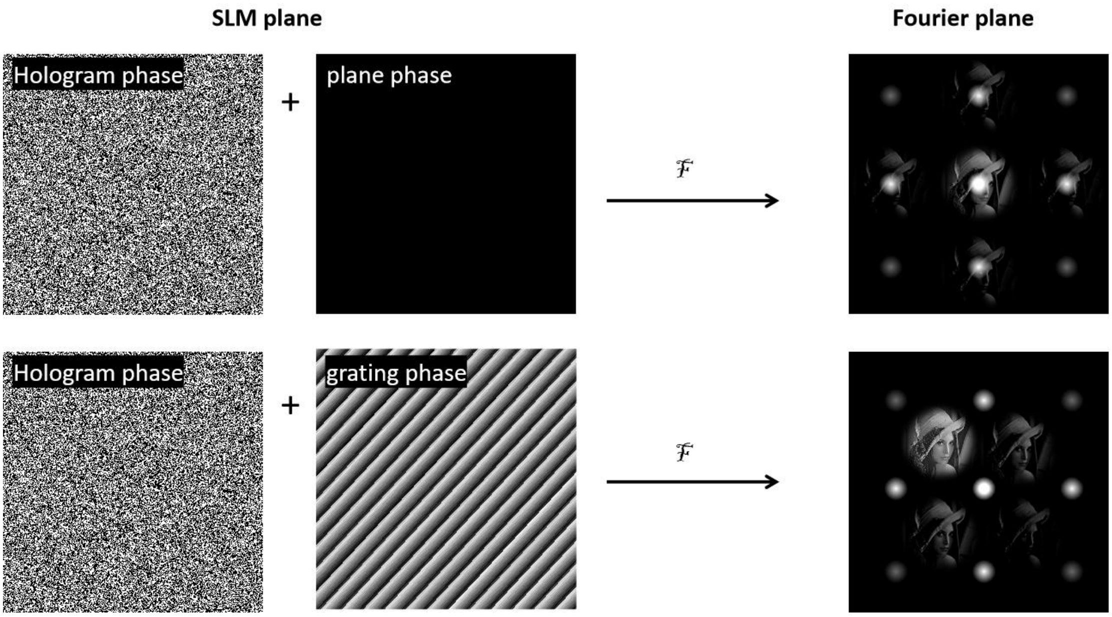

Figure 1-10. Schematic diagram of the method for avoiding intrinsic diffraction from the SLM by using a grating-based phase shift.

B. Digital Micro-mirror Devices

DMDs are micro-electromechanical systems (MEMS) that consist of an array of tiny, individually controllable mirrors. These mirrors can tilt between two states, typically +12°and -12°, to modulate light. DMDs are widely used in digital projection, structured illumination, holography, and optical computing due to their high speed and precision.

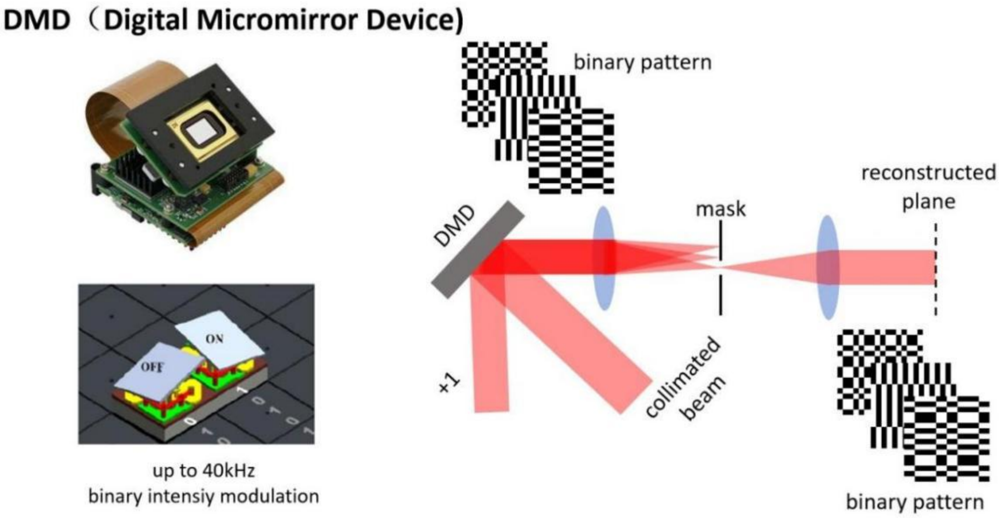

Figure 1-11. Structure of DMD and Amplitude Optical Field Modulation Method.

Binary Amplitude Modulation Principle

Since each mirror in a DMD has only two states (ON or OFF), the device inherently performs binary amplitude modulation rather than continuous grayscale modulation. When a mirror is in the ON state, it reflects light towards the desired direction, whereas in the OFF state, the light is deflected away.

To achieve grayscale intensity control, temporal or spatial dithering techniques are used:

(1) Temporal Modulation (Pulse Width Modulation, PWM): The mirror rapidly switches between ON and OFF states within a single frame period, and the time spent in each state determines the effective intensity.

(2) Spatial Modulation (Error Diffusion & Dithering): The grayscale is approximated by arranging pixels in a specific pattern where the proportion of ON mirrors in a region represents the desired intensity.

Frequency-Based Grayscale Modulation

To accelerate the conversion of grayscale images into binary distributions, frequency-based methods are used. These methods ensure smooth intensity transitions while maintaining high-speed modulation:

(1) Error Diffusion Algorithm[33]: This distributes quantization error across neighboring pixels to create a visually continuous tone.

(2) Halftoning with Blue Noise Masking[34]: Uses precomputed patterns to approximate grayscale perception.

(3) Fourier-based Frequency Optimization[35]: Converts grayscale images into binary patterns while preserving spatial and frequency-domain characteristics.

Phase Modulation Based on DMD

Since each micromirror in a DMD can only be in an ON or OFF state, direct phase modulation is not possible as in LC-SLMs. However, binary-phase encoding and grating-based phase modulation techniques allow DMDs to control phase effectively.

Here, I mainly introduce the Lee hologram method, which is also the mainstream approach for phase modulation using a DMD. Lee Hologram Method for binary amplitude off-axis holography, which is widely used for generating phase-modulated images with DMDs. The amplitude hologram $t(x, y)$ is generated using the Lee method, where an off-axis reference wave encodes the desired phase distribution[36]:

$$t(x, y) = 0.5\big[1 + \cos\big(2\pi(x - y)\alpha - \varphi(x, y)\big)\big] \tag{1-18}$$

Where:

α is the carrier frequency (spatial frequency of the grating).

x, y are the spatial coordinates of the hologram.

$\varphi(x,y)$ represents the desired phase distribution.

The carrier frequency α is carefully chosen to ensure off-axis diagonal encoding, which helps in minimizing crosstalk between diffraction orders. A high enough frequency separates the -1$_{st}$ order from the 0th order beam, allowing efficient filtering.

Since DMDs operate in binary amplitude mode (ON/OFF states), the amplitude hologram $t(x,y)$ must be thresholded to generate a binary hologram. The thresholding function is:

$$h(x,y) = \begin{cases} 1, & t(x,y) > 0.5 \\ 0, & \text{otherwise} \end{cases} \tag{1-19}$$

The Lee method provides an effective way to encode phase-only holograms into binary amplitude holograms, enabling DMD-based holographic imaging and beam shaping. By introducing a carrier frequency and applying thresholding, it efficiently reconstructs the desired optical field in a selected diffraction order. The code of Lee's hologram method is shown in 6.1.

C. Other Controllable Spatial Optical Field Modulation Devices

In addition to LC-SLMs and DMDs, several other devices offer controllable spatial optical field modulation, including:

(1) Deformable Mirrors (DMs): These consist of a reflective membrane controlled by an array of actuators, enabling high-precision wavefront shaping for applications such as adaptive optics, laser beam correction, and high-resolution imaging. The advantage of a deformable mirror is that it can modulate phase in a nearly continuous manner in space, which more closely approximates a far-field spatial light field. However, its drawbacks include a limited number of pixels, speed constraints, and the inability to directly control the amplitude profile.

(2) galvolens: Scanning mirrors consist of high-speed oscillating reflective surfaces and can be arranged into 2D scanning systems, where the beam is scanned by altering the mirror's angle. They are divided into conventional scanning mirrors and resonant mirrors, which can achieve frequencies of several hundred Hz and several kHz, respectively. Their advantages include fast modulation speed, ease of control, large aperture, high precision, and low cost. However, they introduce aberrations, especially due to the spatial separation between the X and Y axes, which lead to field curvature and distortion. Typically, scanning lenses or long-focusing lenses are used to mitigate these issues, although they cannot be completely eliminated. In Chapter 3, we proposed compensating for the distance between the X and Y axes using a cylindrical lens configuration, which, in our application scenario, resolves the deviation in the XY scanning angles. I addressed this issue and provided a solution in Chapter 3.

(3) Acousto-Optic Deflectors (AODs): Utilize sound waves in a crystal medium to create dynamic diffraction gratings, allowing for fast beam steering, frequency modulation, and optical signal processing in fields such as laser scanning, optical trapping, and optical communication. The advantage is that the modulation frequency can be extremely high, reaching the MHz range, but

the drawback is that it introduces aberrations.

(4) MEMS: MEMS 2D scanning mirrors use electrostatic, electromagnetic, piezoelectric, or thermal actuation to control beam steering with high precision. They operate in resonant mode for high-speed scanning in LiDAR and laser displays or in quasi-static mode for stable beam steering in optical communication and adaptive optics. These mirrors offer low power consumption, miniaturization, and fast response, making them ideal for compact optical systems. Advanced MEMS fabrication enables multi-axis scanning and dynamic optical field control, enhancing applications in biomedical imaging, projection systems, and AR/VR displays.

(5) Other: Beyond the devices mentioned above, various dynamic optical modulation devices, such as rotating mirrors, polarizers, waveplates, diffraction gratings, voice coil motors (VCM), piezoelectric actuators, and tunable-focus lenses (liquid, membrane, acoustic-optic), enable precise beam control and adaptive focusing. These devices can be chosen based on requirements such as modulation mode, speed, aperture, modulation range, and more.

1.2.3.2 Static Optical Field Modulation Devices

A. Optical Lens, Prisms, and Mirrors

Static optical field modulation devices are passive optical components that permanently alter the phase, amplitude, or direction of light based on their intrinsic properties without requiring external control. Common examples include lenses, which focus or diverge light by introducing controlled phase delays; prisms, which refract and disperse light for spectral decomposition and beam steering; and concave or convex mirrors, which modify wavefront curvature through reflection, widely used in telescopes and optical resonators. These devices provide stable and precise light control, making them essential in imaging systems, laser beam shaping, and optical communication.

B. Diffractive Devices

Diffractive devices manipulate light through engineered microstructures and interference effects, enabling various optical functions. Diffractive Optical Elements (DOEs) create controlled diffraction patterns for beam shaping, splitting, and focusing, while Holographic Optical Elements (HOEs) reconstruct specific wavefronts using recorded interference patterns. These components, due to their customized functionality, integration, and lightweight design, can be easily applied to AR/VR devices or other projection systems.

C. Metasurfaces

Metasurfaces are ultrathin, subwavelength-structured optical devices that manipulate light at the nanoscale by engineering phase, amplitude, and polarization through precisely designed nanostructures. Unlike traditional optical elements, metasurfaces rely on resonant interactions and geometric phase effects to tailor wavefronts with high precision. By spatially arranging plasmonic or dielectric nanostructures, metasurfaces enable functionalities such as beam shaping, holography, polarization control, and vortex beam generation. Their ability to achieve arbitrary wavefront modulation in a compact form factor makes them highly promising for applications in flat optics, high-resolution imaging, and ultracompact optical systems.

D. Optical Waveguides and Photonic Crystals

Waveguides and photonic crystals guide and control the propagation of light through confined structures, allowing for efficient routing and manipulation of optical signals.

Planar waveguides: Used in integrated photonic circuits for high-speed data transmission.

Photonic crystal fibers: Feature periodic structures that enable unique light-guiding properties.

1.2.4 Temporal Light Field Modulation

Temporal light field modulation involves controlling and manipulating the properties of light over time to achieve precise temporal and spatial resolution. Various techniques are employed in fields such as ultrafast imaging, fluorescence lifetime measurement, and optical signal processing. Below are some of the key methods:

1.2.4.1 Time-Gated Imaging

Time-gated filtering selectively captures photons within a specific time window after excitation, allowing precise temporal control over detected signals. This method effectively suppresses unwanted background noise, such as autofluorescence, scattered light, or short-lifetime fluorescence, thereby significantly enhancing contrast and SNR in fluorescent microscopy.

Time-gated imaging does not require optical filters to separate signals, allowing it to effectively eliminate laser scattering even when fluorescence emission occurs at nearby wavelengths. By precisely controlling the detection time window, it selectively captures photons from longer-lived fluorescence while suppressing short-lived laser reflections and unwanted background signals. This makes time-gated imaging particularly useful for fluorescence lifetime imaging (FLIM).

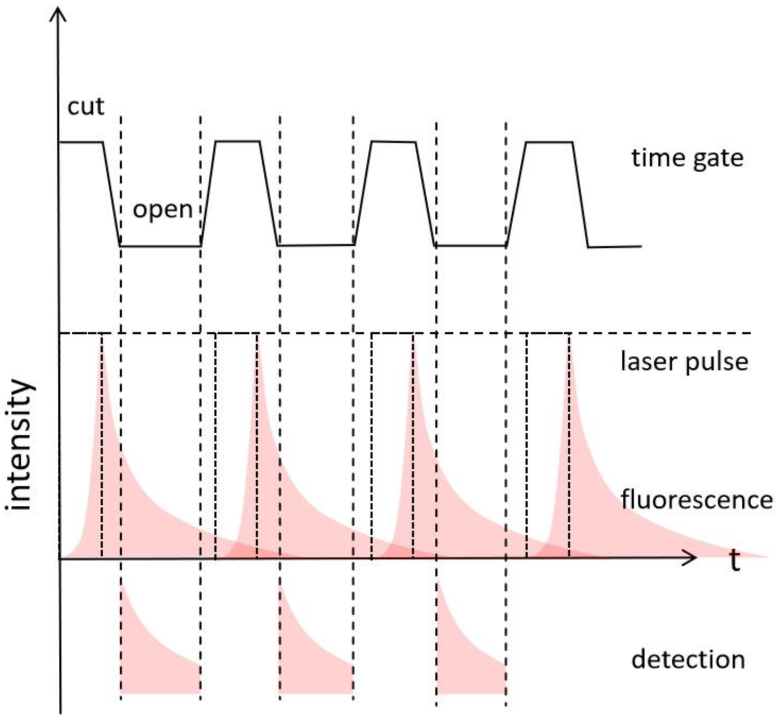

Figure 1-12. Principle of time-gated imaging.

Time-gated lifetime imaging measures fluorescence decay by controlling the relative phase shift between the excitation laser pulse and the detection window, enabling selective photon capture at different time delays. By collecting photon counts at multiple phases and performing deconvolution between the detection window and the excitation pulse, the fluorescence lifetime distribution is extracted. This technique offers high photon throughput and enables wide-field direct imaging, making it ideal for FLIM, material science, and deep-tissue imaging. However, it struggles with nanosecond-scale lifetimes due to the finite detection gate width and requires precise temporal synchronization. Despite this, time-gated lifetime imaging remains a powerful method for high-contrast, time-resolved optical measurements in biological and material sciences.

1.2.4.2 Time-Correlated Single-Photon Counting (TCSPC)

For nanosecond-scale lifetimes, the TCSPC method is used. This technique employs short-pulse lasers (with durations in the nanosecond (ns), picosecond (ps), or femtosecond (fs) range) to excite the sample. The system measures the arrival time delay of individual photons relative to the excitation pulse using a high-precision timing circuit. By accumulating and statistically analyzing the number of detected photons at different time delays, a fluorescence decay curve (lifetime distribution) is generated. This approach offers high temporal resolution and is widely applied in FLIM, single-molecule detection, and time-resolved spectroscopy.

1.2.4.3 Other Temporal Light-field Modulation

Most optical field control in the time domain is achieved through pulse modulation, which can be extended into the time-frequency domain. By integrating this with SLMs, full spatiotemporal light modulation can be realized. Additionally, phase, OAM, and other time-dependent parameters can be dynamically controlled, enabling advanced applications in ultrafast optics, structured light, and time-resolved imaging.

Another approach to time-domain modulation involves manipulating the propagation speed of light, leveraging effects such as dispersion-based pulse compression and mode dispersion in optical fibers. In dispersive media, spectral components travel at different speeds. This allows pulses to be stretched, compressed, or shaped. These effects are widely used in ultrafast laser generation, time-stretch imaging, and supercontinuum generation. In multimode fibers, different optical modes propagate at distinct speeds, leading to mode dispersion, which can be utilized for ultrafast imaging, time-division multiplexing (TDM), and high-speed optical signal processing. These techniques provide precise spatiotemporal light control, expanding applications in ultrafast optics[37], high-speed communication[38], and optical computing[39].

1.2.5 Devices for temporal Light field Manipulation

1.2.5.1 Acousto-Optic Modulation (AOM)

AOM utilizes an RF-driven acoustic wave to create a dynamic refractive index grating in an acousto-optic crystal, enabling optical frequency shifting, beam deflection, and pulse intensity modulation. With switching speeds in the MHz to GHz range, AOMs are widely used in Q-switching, mode-locking, time-resolved spectroscopy, laser pulse shaping, and optical communication. Their high-speed response makes them essential for applications requiring precise optical control.

1.2.5.2 Electro-Optic Modulation (EOM)

EOMs rely on an external electric field to induce changes in the refractive index of an electro-optic material (e.g., $LiNbO_3$), allowing for high-speed phase and amplitude modulation. With modulation capabilities reaching the GHz range, EOMs play a crucial role in coherent optical communication, laser pulse control, chirped pulse amplification (CPA), frequency comb stabilization, and high-speed optical computing. Their ultrafast response makes them indispensable in modern photonic systems.

1.2.5.3 Optical Chopper Modulation

Optical choppers use a mechanical rotating disk with slits to periodically block and unblock a laser beam, generating an intensity-modulated optical signal. Operating at frequencies from Hz to kHz, they are commonly used in lock-in detection, signal demodulation, and fluorescence lifetime measurements. Optical choppers are widely applied in Raman spectroscopy, photothermal imaging, and optical pump-probe experiments, where precise timing and modulation of light are required.

1.2.5.4 Pulsed Laser

Pulsed lasers produce optical pulses ranging from nanoseconds to femtoseconds, enabling high-energy and high-intensity applications. Depending on the type, Q-switched lasers generate high-energy nanosecond pulses for laser machining, LIBS, and LIDAR, while mode-locked lasers produce ultrashort femtosecond pulses crucial for time-resolved imaging, multiphoton microscopy, and frequency comb generation. Additionally, regenerative amplifiers amplify femtosecond pulses for high-intensity applications like high-field physics and attosecond science. Pulsed lasers are widely used in ultrafast spectroscopy, nonlinear optics, biomedical imaging, and industrial laser processing, making them fundamental in scientific and technological advancements.

1.2.6 Conclusion

In this section, we introduced the equipment and components required for spatiotemporal light field modulation, which form the foundation of modern optical light field control. As an important application of light field modulation technology, microscopic imaging relies on selecting appropriate light field modulation components as its foundation. Next, I will introduce the imaging requirements corresponding to different imaging scales. These requirements can guide us in selecting the appropriate light field modulation techniques for imaging.

1.3 Light Field Modulation for Volumetric Imaging Across Scales

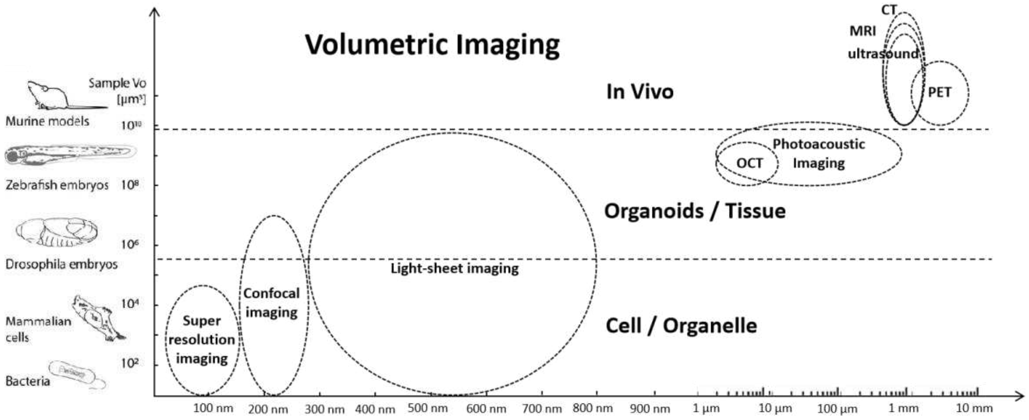

Figure 1-13. Volumetric Imaging Methods and Their Corresponding Spatial Scale Ranges[40].

Biological imaging spans across multiple scales, from whole organisms to subcellular structures, each with distinct challenges related to light scattering, absorption, and motion artifacts. Therefore, biological imaging at different scales requires corresponding optical field modulation techniques. Here, I categorize the spatial scales into three levels: In Vivo, Organoids/Tissue, and Cells/Organelles. This section discusses the challenges of microscopic imaging at these scales and the appropriate methods for each.

1.3.1 Macroscopic Scale

For whole-organism imaging, where sample volumes range from 10^9 to 10^{11} μm^3, the primary challenges are deep tissue penetration, light scattering, and motion artifacts. To compensate for scattering, diffraction, and aberrations caused by the inhomogeneity of biological samples, an adaptive optics (AO) system is typically used for wavefront correction, including illumination light field modulation and imaging plane calibration[41, 42]. On the other hand, non-diffracting light is also applied in thick samples[43]. Due to the non-diffracting properties of beams such as Bessel beams, the illumination light exhibits self-healing characteristics after diffraction, making it less prone to distortion. In recent years, near-infrared II (NIR-II) illumination techniques have emerged in live imaging[44-46]. Due to their longer wavelengths compared to visible light, they experience less scattering, allowing them to penetrate thicker samples. The NIR-II wavelength range spans from 900 nm to 1700 nm, aligning with the water absorption window, which facilitates in vivo imaging.

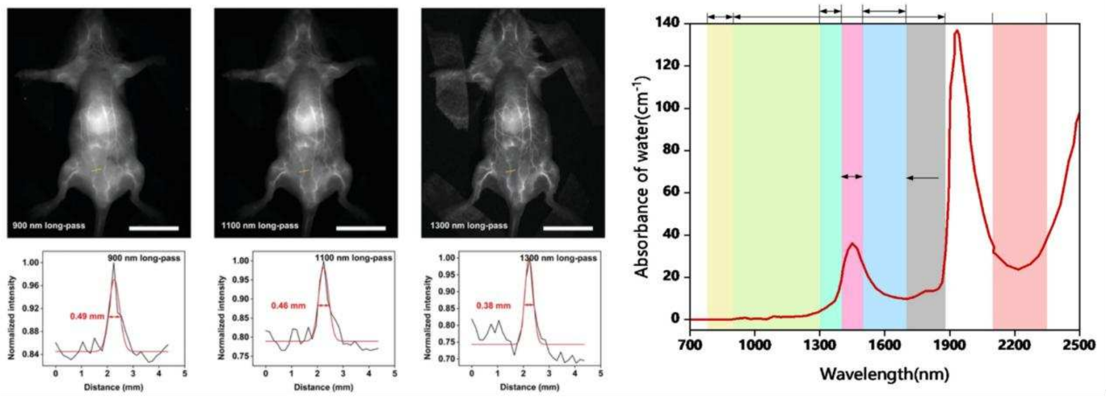

Figure 1-14. Left: The signal-to-noise ratio (SNR) of NIR-II imaging increases with wavelength[47]. Right: The absorption spectrum of water[48].

1.3.2 Mesoscopic Scale

At the mesoscopic scale (sample volumes 10^4 to 10^6 μm^3), biological specimens such as organoids and Drosophila embryos require high-speed volumetric imaging to capture dynamic biological processes while minimizing phototoxicity. In imaging at this scale range, light field modulation is often used for wavefront correction to compensate for aberrations caused by the sample. Compared to in vivo imaging, where scattering is a major issue, smaller-scale imaging primarily faces challenges from diffraction. As a result, non-diffracting beams and AO are commonly applied[49]. Due to the need for rapid volumetric imaging, light-sheet microscopy, particularly non-diffracting light sheets, is frequently utilized such as lattice light sheet and Bessel beam light sheet.

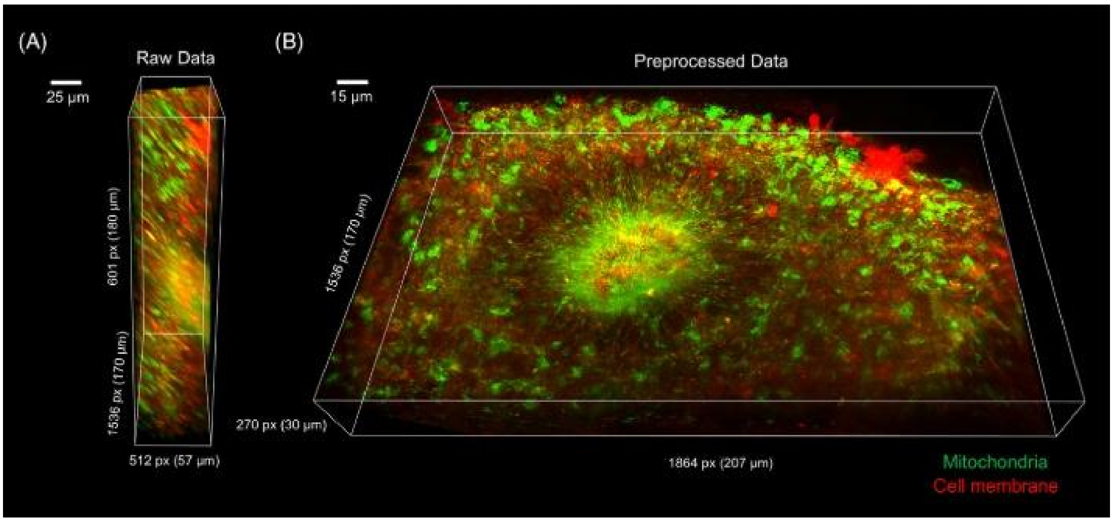

Figure 1-15. 3D imaging of lung organoids using lattice light-sheet microscopy (LLSM)[50].

1.3.3 Microscopic and Subcellular Scale

At the microscopic and subcellular level (sample volumes as small as 10^2 μm^3), achieving nanometer-scale precision while minimizing phototoxicity is a major challenge. At this scale, where samples typically range from a few to tens of micrometers, the effects of scattering and diffraction on imaging are relatively minor. However, the internal structures of these samples measure from a few nanometers to several hundred nanometers. Given that the diffraction limit of visible light is around 200 nm. Therefore, researchers employ super-resolution imaging techniques to enhance optical resolution to the sub-100 nm or even tens of nanometers scale. Super-resolution techniques such as STED and SIM utilize precisely modulated excitation patterns to surpass the optical diffraction limit, STORM/PALM (Stochastic Optical Reconstruction Microscopy / Photoactivated Localization Microscopy) utilize single-molecule localization techniques, enabling detailed visualization of subcellular structures. Super-resolution techniques based on structured illumination will be introduced in the next section.

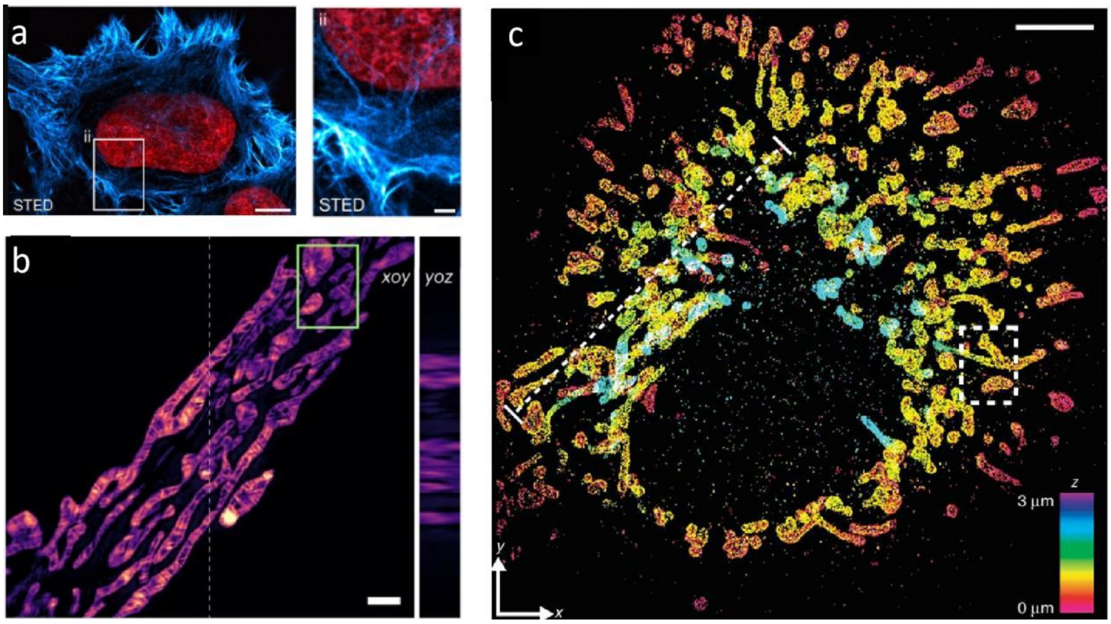

Figure 1-16.(a) Two-color 2D STED image of a fixed HeLa cell labeled for actin (lifeact-AF594, cyan hot) and DNA (JF646-Hoechst, red)[51] (b)Open-3DSIM analyzed the 3D mitochondrial ridge structure in live COS7 cell and showed the process of mitochondrial fusion, separation and apoptosis under a low SNR (10%, 3 ms)[52]. (c) 3D STORM images of mitochondria in a whole mammalian cell[53]. Scale bar: (a): 5 µm 3 µm.(b): 2 µm. (c): 5 µm.

1.3.4 Conclusion

Across all biological imaging scales, light field modulation plays a crucial role in optimizing imaging performance by addressing scale-specific challenges. From adaptive optics and structured light fields for deep tissue imaging to super-resolution microscopy and computational wavefront shaping at the subcellular level, these techniques enable high-resolution, high-contrast imaging while minimizing photodamage. As computational optics and light-field engineering continue to advance, further integration of dynamic phase correction and multimodal imaging strategies will enhance imaging accuracy and depth across all biological systems.

Table 1-2. Light field Modulation Methods for Multi-scale Imaging

Imaging Scale	Resolution	FOV	Main Challenges	Suitable Methods
In Vivo (Organism)	1–10 µm (typical, can be higher)	mm–cm (covers tissues/organs)	Tissue scattering and absorption, motion (breathing, etc.), limited depth	Adaptive Optics (AO), Multi-Photon Microscopy
Organoid/Tissue	1–2 µm (typical)	Hundreds of µm to a few mm	Thick samples, complex 3D structures, rapid volumetric imaging	Light Field Microscopy (LFM), Structured Illumination Microscopy (SIM), Multi-Photon/Two-Photon Microscopy, Lattice Light Sheet Microscopy
Organelle (Subcellular)	<200 nm (super-resolution)	Tens to hundreds of µm (single cell)	High resolution, low phototoxicity, labeling	STED, STORM, PALM, SIM, Two-Photon + AO, Spinning-Disk Confocal Microscopy

1.4 Microscopes using Light-field modulation

From the perspective of optical field modulation, all microscopy systems that do not use wide-field illumination involve forms of light field control, as illustrated in **Figure 1-12**. In this paper, I primarily focus on SIM-based and light-sheet-based methods.

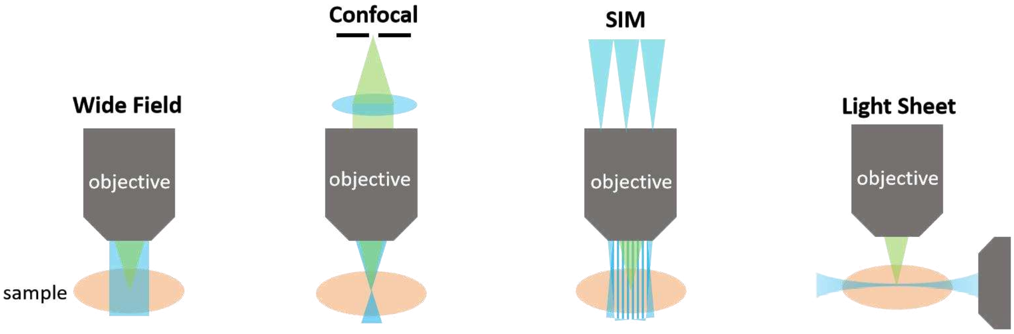

Figure 1-17. Typical Microscopes using Light Field Modulation.

1.4.1 Structured illumination Modulation

1.4.1.1 Optical Diffraction Limit

Light field modulation is a powerful technique in optical imaging, enabling precise control of light's spatial, temporal, spectral, and polarization properties. One critical application of this technology is in Structured Illumination Microscopy (SIM), which employs patterned light fields to surpass the diffraction limit and achieve super-resolution imaging.

This section explores the principles, methods, and applications of light field modulation in SIM, particularly focusing on how modulated light fields contribute to spatial frequency extension and high-resolution imaging.

In traditional microscopy, resolution is constrained by the diffraction limit, as described by Ernst Abbe in the 19th century[54]. The maximum resolvable Lateral Resolution d_{xy} is given by:

$$d_{xy} = \frac{\lambda}{2nsin\theta} = \frac{\lambda}{2NA} \tag{1-20}$$

For Rayleigh Criterion[55] which describes the minimum resolvable distance between two point sources, the Lateral Resolution d_{xy} is given by:

$$d_{xy} = \frac{0.61\lambda}{NA} \tag{1-21}$$

Axial resolution[56] describes the minimum resolvable distance along the optical axis, given by the formula:

$$d_z = \frac{\lambda}{2n(1-cos\theta)} = \frac{\lambda}{2NA^2} \tag{1-22}$$

Where:

d_{xy} : Lateral resolution (minimum resolvable distance)

d_z : Axial resolution (minimum resolvable distance)

λ: Wavelength of the imaging light

n: Refractive index of the medium

θ: Half-angle of the objective lens (maximum light incidence angle)

NA: Numerical Aperture

We already know that the resolution limit of an optical imaging system is determined by its numerical aperture (NA). To better describe the system's imaging resolution, We introduce the concept of the point spread function (PSF).

$$I_{\text{image}}(x,y,z) = PSF(x,y,z) * I_{\text{object}}(x,y,z) \tag{1-23}$$

Where:

$I_{\text{image}}(x,y,z)$ is the measured image;

$*$ presents convolution operation;

$PSF(x,y,z)$ is the 3d point spread function of the system;

$I_{\text{object}}(x,y,z)$ is the light field of object.

Since convolution in the spatial domain corresponds to multiplication in the frequency domain, image processing is often performed in the frequency domain. Therefore, I use the Fourier transform of the PSF, known as the Optical Transfer Function (OTF):

$$OTF(f_x, f_y, f_z) = \mathcal{F}\{PSF(x, y, z)\} \tag{1-24}$$

Where:

$OTF(f_x, f_y, f_z)$ represents the optical transfer function in the spatial frequency domain.

$\mathcal{F}$ denotes the Fourier transform.

Since the OTF is a complex function, it can be decomposed into:

$$OTF(f_x, f_y, f_Z) = MTF(f_x, f_y, f_z) \cdot e^{iPTF(f_x, f_y, f_z)} \tag{1-25}$$

Where:

MTF (Modulation Transfer Function) is $|OTF|$, describes the contrast transmission of different spatial frequencies.

PTF (Phase Transfer Function) is $arg(OTF)$, represents the phase shift introduced by the optical system.

The OTF determines how well an optical system preserves contrast and phase information across spatial frequencies, making it essential for analyzing imaging performance.

1.4.1.2 Structured Illumination Super-Resolution Principle

Structured Illumination Microscopy (SIM) is a super-resolution imaging technique that enhances spatial resolution beyond the optical diffraction limit by using patterned illumination and computational reconstruction[57, 58]. By introducing spatially modulated illumination patterns and leveraging the frequency mixing effect in the Fourier domain, SIM extracts high-frequency components that are normally inaccessible due to diffraction limitations.

The fundamental principle of SIM relies on the spatial frequency shift induced by structured illumination. When a high-frequency structured illumination pattern $I(x)$ is projected onto the sample, the sample's inherent spatial frequencies are heterodyned (mixed) with the illumination pattern, shifting normally undetectable high-frequency components into the observable range of the microscope.

As previously introduced, the angular spectrum theory describes light propagation, and the objective lens effectively performs a Fourier transform on the optical field at the back focal plane (BFP). By utilizing optical field modulation devices, I can generate the desired optical field distribution at the BFP. The Fourier transform of the optical field can be expressed as:

$$U_{sample}(x, y) = \iint U_{BFP}(f_x, f_y) e^{i2\pi(f_x x + f_y y)} df_x df_y \tag{1-26}$$

The optical field at the back focal plane (BFP) and the intensity distribution of the modulated light field corresponding to the structured illumination method are shown in **Figure 1-13** [59].

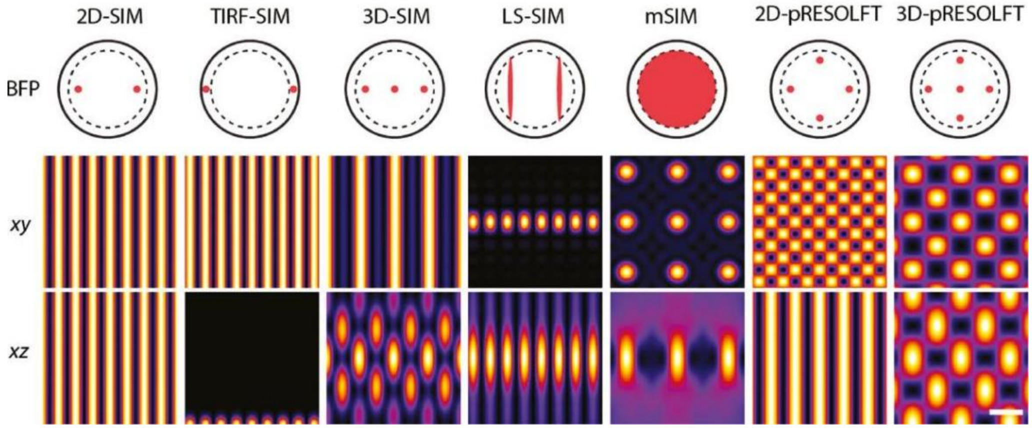

Figure 1-18. Comparison of Structured Illumination Patterns in Different Super-Resolution Microscopy Techniques.

The interaction between the object and the structured illumination in both the spatial domain and the Fourier frequency domain is shown in Figure 1-19.

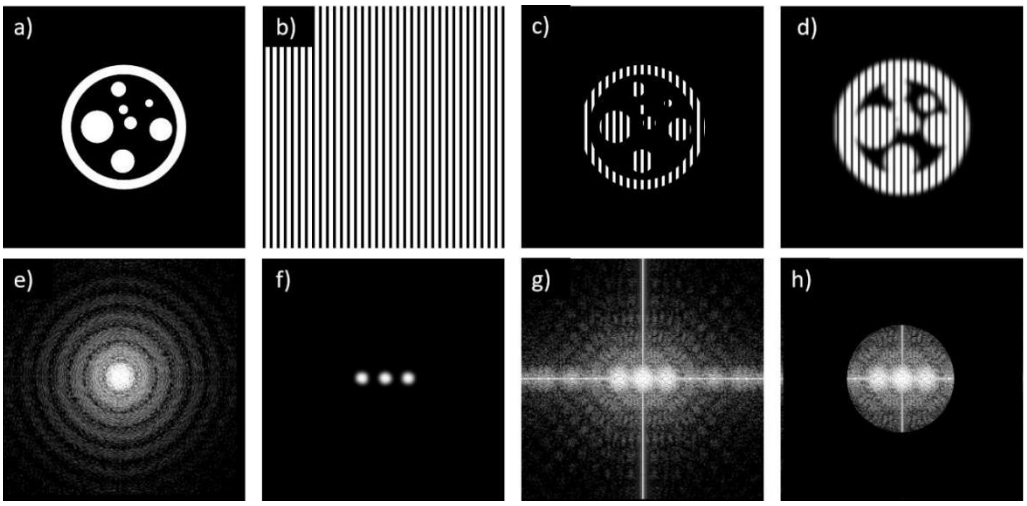

Figure 1-19. Model of two-beam SIM imaging.

a) The sample's spatial distribution is denoted as $S(x)$, representing the object to be imaged.

b) Structured Illumination Pattern $I(x)$.

c) Excited Fluorescence Emission E_m. The structured illumination interacts with the sample, producing an emission pattern:

$$E_m = S(x) \cdot I(x) \tag{1-27}$$

d) Formation of a Single SIM Image. The emitted light passes through the imaging system, where it undergoes convolution with the system's PSF, $h(x)$:

$$(S(x) \cdot I(x)) \otimes h(x) \tag{1-28}$$

e) Fourier Space Representation of the Sample $\tilde{S}(x)$.

f) Fourier Space Representation of the Illumination $\tilde{I}(x)$.

g) Fourier Space Modulation. The detected image is the convolution of the object and the illumination in Fourier space:

$$\widetilde{E_m}(x) = \tilde{S}(x) \otimes \tilde{I}(x) \tag{1-29}$$

h) Fourier Space of a Single SIM Image.

$$(\tilde{S}(x) \otimes \tilde{I}(x)) \cdot \tilde{h}(x) \tag{1-30}$$

1.4.1.3 Structured Illumination Microscopy (SIM) Reconstruction Techniques

SIM enhances spatial resolution by shifting high-frequency information into the system′s optical transfer function (OTF) through patterned illumination. The reconstruction of super-resolved images requires computational processing of multiple phase-shifted images to extract and synthesize these high-frequency components. Over time, SIM reconstruction techniques have evolved into three main categories: Fourier domain reconstruction, iterative reconstruction with regularization, and deep learning-assisted reconstruction, each offering distinct advantages and applications[1].

A. Fourier Domain Reconstruction in SIM

Fourier-based reconstruction is the most widely used method in SIM, leveraging frequency mixing induced by structured illumination to extend the system's spatial bandwidth. The structured light pattern interacts with the sample, generating multiple shifted copies of the high-frequency content in the Fourier domain. These frequency components are then computationally extracted and realigned, effectively expanding the OTF and enhancing image resolution up to twice the diffraction limit.

This approach is highly effective for high-speed, live-cell imaging, as it allows direct frequency-domain manipulation without requiring heavy computation. However, in low-signal conditions, Fourier-based methods may introduce artifacts due to incomplete frequency information and noise amplification. Advanced implementations, such as HiFi-SIM, integrate optimized frequency weighting to reduce artifacts and improve reconstruction fidelity.

B. Iterative Reconstruction and Regularization in SIM

To improve resolution while reducing noise and artifacts, iterative reconstruction algorithms apply constraints such as sparsity, smoothness, and prior knowledge of the sample structure. These methods iteratively refine the estimated high-resolution image by enforcing physically meaningful constraints.

Key regularization techniques include:

(1) Total Variation (TV) Minimization − Reduces noise while preserving sharp edges.

(2) Bayesian Inference − Enhances resolution by incorporating prior knowledge into the reconstruction.

(3) Maximum Likelihood Estimation (MLE) – Optimizes image quality through statistical modeling.

Iterative reconstruction is particularly useful for low-light and high-noise imaging conditions, where direct Fourier-based reconstruction may lead to image degradation. Although computationally intensive, these methods offer enhanced contrast and reduced artifacts, making them ideal for high-fidelity imaging applications.

C. Deep Learning-Assisted SIM Reconstruction

Recent advances in deep learning have introduced data-driven reconstruction techniques for SIM. Convolutional neural networks (CNNs) and generative adversarial networks (GANs) can be trained on large datasets of low-resolution and high-resolution image pairs, learning to intelligently reconstruct missing frequency components, denoise images, and remove artifacts.

Key deep learning-based SIM methods include:

(1) Deep-SIM – Uses CNNs to improve resolution and suppress artifacts in real time.

(2) AI-SIM – Leverages machine learning to reconstruct super-resolved images with minimal computational overhead.

(3) GAN-based SIM – Employs adversarial training to enhance fine details beyond traditional SIM resolution limits.

Deep learning methods have demonstrated remarkable capabilities in real-time imaging, offering fast, high-quality reconstructions without requiring complex phase retrieval algorithms. However, they rely on extensive training datasets and may struggle with generalization across different sample types.

Multi-Angle and Multi-Pattern SIM for 3D Super-Resolution

For 3D SIM, multiple illumination angles and polarization states are used to reconstruct high-resolution volumetric images. By capturing structured illumination patterns from different orientations, high-frequency spatial details in all three dimensions can be recovered. Computational algorithms then integrate the frequency-shifted information from multiple planes to reconstruct a 3D super-resolved image. This approach is particularly useful for imaging thick biological samples, where traditional wide-field or confocal microscopy suffers from depth-dependent resolution loss. Advanced 3D SIM techniques enable high-speed volumetric imaging with improved axial resolution, facilitating studies of live-cell dynamics in biological research.

The development of SIM reconstruction techniques has progressed from Fourier-based frequency extraction to iterative refinement and, most recently, deep learning-assisted reconstruction. Fourier-based methods remain the most computationally efficient, while iterative reconstruction provides enhanced noise robustness. Meanwhile, deep learning approaches are rapidly emerging as powerful tools for real-time SIM imaging, offering new possibilities for biomedical research and super-resolution microscopy. The future of SIM reconstruction will likely integrate these methods to balance computational efficiency, resolution enhancement, and noise suppression for high-speed, high-fidelity imaging.

1.4.2 Light-sheet Modulation

Light-sheet microscopy is one of the most intuitive and straightforward methods for acquiring 3D volumetric imaging[60]. With the advancement of optical microscopy techniques, the demands of biological research on imaging systems have increased, primarily reflecting the need for high resolution, fast imaging speed, 3D volumetric imaging, and in vivo imaging[61]. Light-sheet microscopy meets these requirements in several ways. First, the orthogonal arrangement of the illumination light and the imaging pathway ensures that the imaging system is almost unaffected by the illumination light, allowing for high-contrast imaging. Second, the combination of light-sheet illumination and wide-field detection enables high-throughput, large-field-of-view 3D volumetric imaging. Lastly, the illumination power required is similar to that of conventional wide-field microscopy, making it suitable for live-cell imaging. However, light-sheet imaging has inherent limitations. Firstly, its axial resolution depends on the thickness of the light sheet, and achieving a thinner light sheet often requires sacrificing the FOV. Secondly, the lateral resolution of the light sheet is the same as that of wide-field imaging, limited by the diffraction limit. Finally, due to the requirement for an orthogonal illumination system, the available space in the optical setup is constrained, posing significant challenges for the selection of objective lenses and the design of the sample chamber. Over the past century since its inception, light-sheet microscopy has undergone continuous development. To address the aforementioned limitations, scientists have introduced new advancements, making it more suitable for research in the biological field.

The first recorded system similar with modern light-sheet microscopy can be traced back to 1903[62]. Siedentopf and Zsigmondy developed the system with orthogonal illumination at 90°from the imaging objective lens to study gold particles that were too small to be resolved by conventional microscopes. At this time, light-sheet illumination was primarily used for scattering light imaging. It wasn't until the invention of fluorescence microscopy that it gained significant attention and underwent rapid development[63, 64]. In 1993, Voie et al.[65] developed an optical system for orthogonal plane fluorescence optical sectioning (OPFOS) imaging. This system used a laser as the light source and a cylindrical lens to generate a light sheet to illuminate the guinea pig cochlea. Fluorescence signals were collected by an objective lens positioned orthogonal to the illumination direction, producing optical images with a FOV of 1.5 mm, a lateral resolution of 10 µm, and an axial resolution of 26 μm. Since then, light-sheet microscopy has been primarily used for fluorescence imaging.

The modern era of light-sheet microscopy began In 2004, Huisken et al. [66] introduced Selective Plane Illumination Microscopy (SPIM). The light sheet in this system was generated using a cylindrical lens, and biological samples were embedded in agarose gel and mounted on a four-axis stage (xyz translation and rotational movement). This setup enabled imaging from multiple angles, with the best parts of each angle combined algorithmically to create a sectional image. The study highlighted SPIM's advantages in developmental biology, including low photobleaching and phototoxicity, allowing long-term observation of biological samples. It also provided comprehensive validation using live specimens. Notably, this was the first light-sheet microscope to achieve diffraction-limited resolution[66]. This approach enabled 3D imaging of transparent biological samples while minimizing photodamage. The benefits of SPIM include its ability to support long-term imaging of live embryos, organoids, and tissue samples with minimal phototoxic effects.

Subsequent advancements in light-sheet microscopy have primarily focused on several key areas of improvement. First, enhancing sectioning capabilities, including balancing FOV and light-sheet thickness, as well as mitigating the effects of scattering and absorption on light-sheet illumination. Second, improving lateral resolution to achieve high-resolution or even super-resolution (beyond the optical diffraction limit) sectional images. Third, optimizing system architecture, including simplifying the optical setup to increase operational space and improving the design of sample chambers and scanning methods. Next, the current advancements in light-sheet microscopy from these perspectives will be discussed .

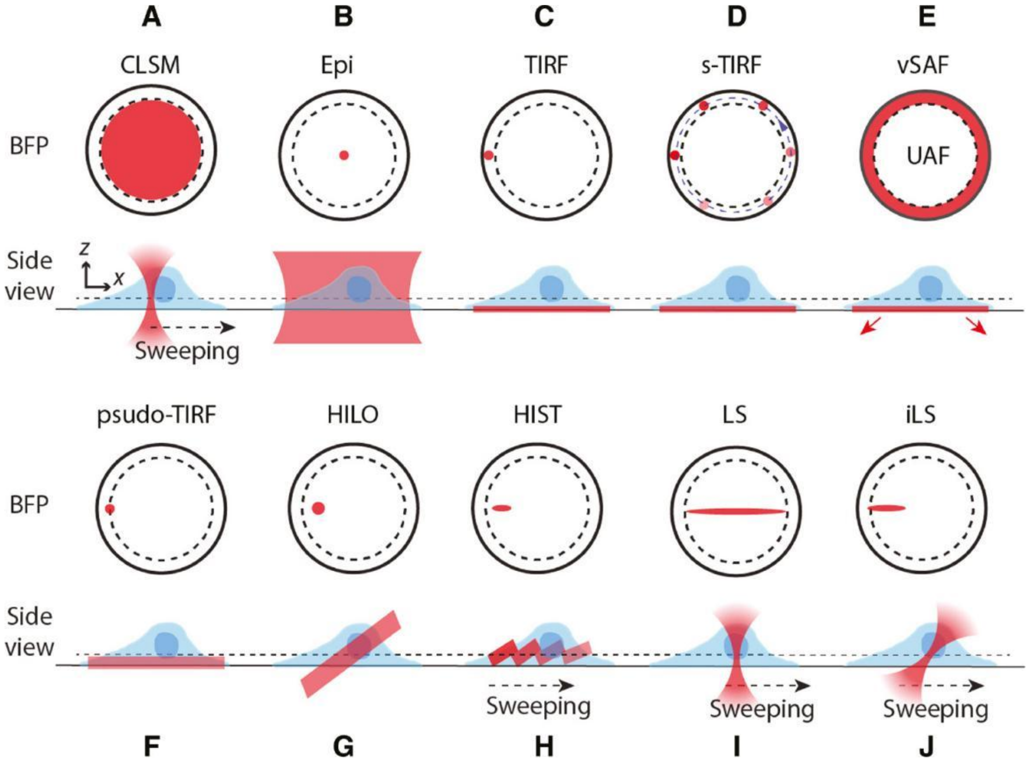

Figure 1-20. Back focal plane Intensity Distribution and Light Sheet Types in Light Sheet Optical Field Modulation.

Basic light-sheet illumination is achieved using a cylindrical lens or a combination of a cylindrical lens and an objective lens. In one dimension, the illumination light is collimated for parallel projection, while in the other dimension, the light beam is focused, forming a thin light sheet near the focal region. The axial resolution is directly related to the thickness of the light sheet. Typically, a Gaussian beam is used, and the beam waist radius of the Gaussian beam directly influences the axial resolution of the light sheet.

The formula for the beam waist radius of a Gaussian beam[67] is:

$$\omega_0 \cong 0.85 * \frac{\lambda}{2*NA} \tag{1-31}$$

Where:

ω_0 is the beam waist radius.

λ is the excitation wavelength.

NA is the numerical aperture of the illumination lens.

Since the illumination in one dimension is collimated, the width of the light sheet corresponds to the aperture of the exit pupil, which is typically much larger than the FOV. Therefore, the FOV for light-sheet illumination is primarily determined by the length of the focused dimension, which can be approximated by the range of the beam waist. The Rayleigh range is:

$$Z_R \cong \frac{\pi\omega_0^2}{\lambda} = \frac{0.7225 *\pi*\lambda}{4NA^2} \tag{1-32}$$

Thus, it can be seen that as the illumination NA increases, the light sheet becomes thinner, but the FOV decreases. Conversely, when the NA decreases, the FOV increases, but the light sheet becomes thicker, resulting in lower axial resolution. The range of resolution and volume size of light-sheet microscopy is as shown in Figure 1-13[40].

1.4.2.1 Improved axial Resolution

From the above equations, We can see the trade-off between FOV and light sheet thickness, but there are methods to achieve both. Certain non-diffracting beams, such as Bessel and Airy beams, exhibit an inherently elongated and diffraction-resistant structure. By sacrificing temporal resolution, these beams can be scanned to create a virtual light sheet, which can also be combined with line-confocal detection for enhanced x resolution. Additionally, axial multi-focus strategies and axial scanning approaches offer effective solutions for generating thin yet extended light sheets, balancing resolution and imaging depth.

A. Non-Diffracting Illumination Strategy

Non-diffracting beams are a class of light beams that maintain a stable wave packet or transverse intensity distribution during propagation. They exhibit unique properties such as non-diffraction, self-healing, and self-acceleration, making them highly advantageous for enhancing far-field imaging performance. The non-diffracting nature suppresses beam spreading caused by diffraction.

Theoretically, these beams are formed by the coherent superposition of plane waves with different angular spectra, where the relative phase differences between waves remain constant. This stability prevents diffraction and allows the wavefront to propagate uniformly.When encountering obstructions, non-diffracting beams can reconstruct the occluded parts through interference, restoring the original wavefront. This self-healing property, combined with the ability to self-accelerate, further enhances their robustness. Experimentally, finite-energy non-diffracting beams are generated by applying an aperture to truncate the angular spectrum. This ensures stable, non-diffracting propagation within a defined spatial region, making them ideal for applications requiring precise and extended light-field control.

Non-diffracting light primarily includes Bessel beams, Airy beams, and vortex beams. Among them, Bessel and Airy beams are particularly suitable for light-sheet illumination due to their elongated and non-diffracting properties.

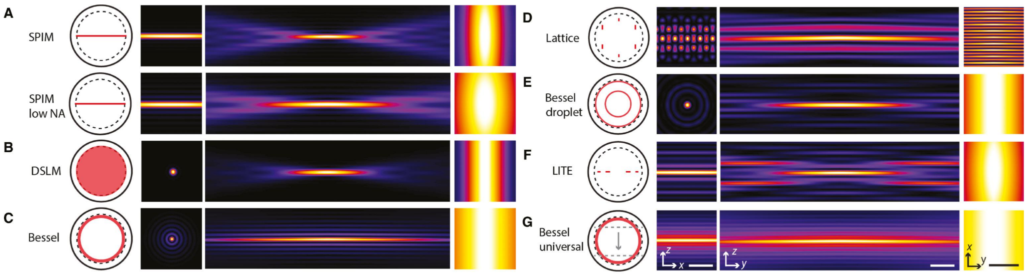

Figure 1-21. Non-diffracting Light Sheet Modulation and Their Back Focal Plane.

Bessel Beams Light-sheet

The transverse intensity distribution of a Bessel beam follows the form of a Bessel function, characterized by high localization during propagation. According to the coherence theory, a Bessel beam is the coherent superposition of plane waves with propagation vectors arranged on a conical surface in angular spectrum space. The amplitude of each plane wave remains constant, while its phase is modulated by the azimuthal angle ϕ, expressed as:

$$A(\phi) \cong A_0\, exp(in\phi) \qquad (1\text{-}33)$$

This formula represents the amplitude of the wave in the angular direction

ϕ, where the initial amplitude A_0 is modulated by a phase factor $exp(in\phi)$, with n as the Bessel beam's order.When the phase difference between the plane waves remains constant, a zeroth-order Bessel beam is formed, with its intensity distribution given by:

$$I(r) \cong |J_0(kr)|^2 \qquad (1\text{-}34)$$

This describes the intensity distribution of a zeroth-order Bessel beam at a radial position r, where J_0 is the zeroth-order Bessel function and $k = \frac{2\pi}{\lambda}$ is the wave vector. This intensity distribution remains unchanged over the propagation distance, demonstrating its non-diffracting property.

The earliest method to generate a Bessel beam in laboratories was the annular aperture method. By placing an annular aperture in the frequency domain and performing a Fourier transform, a Bessel beam could be created. With advancements in spatial light modulation technology, more flexible methods have emerged. For example, using an annular phase plate to modulate the spectrum of a Gaussian beam or plane wave in the frequency domain, followed by Fourier transformation, allows the generation of Bessel beams. This approach facilitates precise control over the beam's propagation characteristics, enhancing its adaptability for various applications.

The earliest use of Bessel light sheets for fluorescence microscopy was by the Betzig's group[68]. Planchon et al. combined Bessel beams with two-photon technology, achieving isotropic resolution of approximately 300 nm, an imaging speed of 200 planes per second, and a FOV of 50 μm[69].

Airy Beams Light-sheet

The Airy function $\mathrm{Ai(x)}$ is a special solution to the wave equation, and the intensity of an Airy beam can be expressed as:

$$I(x) \cong |Ai(x)|^2 \tag{1-35}$$

Where x is the scaling factor determined by the Airy beam itself. The energy of an Airy beam propagates along a parabolic trajectory $\mathrm{s} = (\xi/2)^2$, exhibiting a unique transverse self-acceleration characteristic. In the $\mathrm{x} - \mathrm{z}$ coordinate system, the transverse displacement of the beam is given by:

$$\Delta x \cong \frac{\xi^2}{4} \tag{1-36}$$

Since the integral of the Airy function tends to infinity, the energy of the Airy beam is theoretically infinite and cannot be realized in practice. To generate an Airy beam experimentally, an exponential truncation factor is introduced to limit the beam's energy. Finite-energy Airy beams are typically created using frequency-domain modulation techniques.

In practice, Airy beams are often generated by modulating a plane wavefront using an SLM. The plane wave is modulated with a cubic phase, and then a Fourier transform is applied. At the focal plane of the lens, the Airy beam is formed. This approach enables precise control of the beam properties for experimental applications.

The earliest use of Airy beams was by Tom Vettenburg and colleagues from Kishan Dholakia's group[70]. While Bessel beams also enable an extended field of view, the Airy beam's inherently asymmetric excitation pattern ensures that fluorescence signals are directed constructively, enhancing image contrast and representing a substantial advancement for light-sheet microscopy.

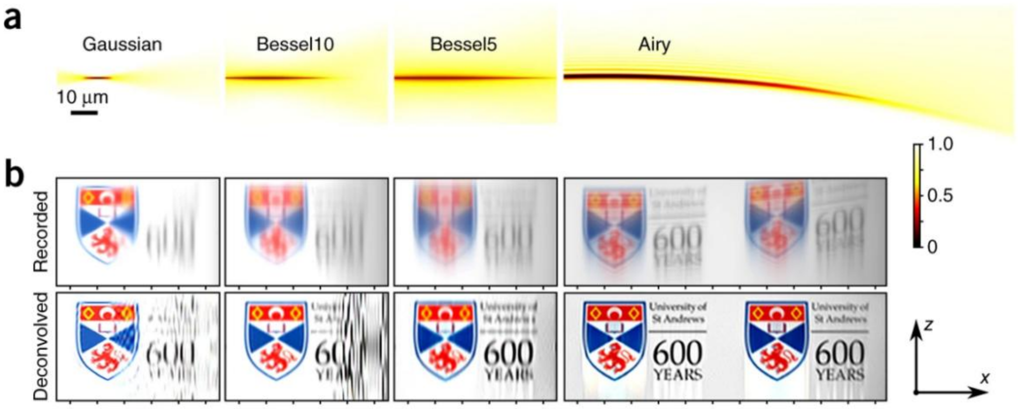

Figure 1-22. Applications of Non-Diffracting Beams in Light-Sheet Microscopy[70]. *(a) x-z plane intensity distribution of Gaussian, Bessel, and Airy beams. (b) Imaging simulation of the three beam types.*

Lattice Light-sheet

Lattice light-sheet microscopy (LLSM) is an advanced imaging technique developed as an extension of Bessel light-sheet microscopy. While Bessel beams provide nondiffracting properties and a long FOV, their inherent side lobes often introduce background fluorescence, reducing image contrast. Lattice light-sheet microscopy overcomes this limitation by using a structured lattice pattern of illumination, which is created through the interference of multiple Bessel beams. This design enhances contrast, reduces phototoxicity, and achieves near-isotropic resolution.

Furthermore, LLSM can achieve super-resolution imaging. During standard imaging, the lattice pattern generates thin, uniform illumination through lateral dithering. In super-resolution mode, the lattice spots undergo phase shifting to expand the spectral range along both the x and z axis, thereby enhancing resolution beyond the diffraction limit.

In 2014, Eric Betzig and his team introduced LLSM in a groundbreaking study published in Science[68]. This innovative technique extended the principles of Bessel beam light-sheet microscopy by employing structured illumination through the interference of multiple Bessel beams, creating a lattice pattern for excitation. The lattice light sheet not only maintained the non-diffracting properties of Bessel beams but also addressed their limitations, such as side-lobe-induced background fluorescence, by significantly enhancing image contrast and reducing phototoxicity.

Betzig's work demonstrated the ability of LLSM to achieve near-isotropic resolution (approximately 230 nm laterally and 370 nm axially) and minimal photobleaching, making it ideal for long-term, live-cell imaging. The study showcased the technique's capabilities through the visualization of dynamic cellular processes in unprecedented detail, such as organelle interactions, cytoskeletal dynamics, and mitosis in live cells. This work marked a transformative step in light-sheet microscopy, combining high-resolution imaging with gentle, non-invasive illumination, and has since become a cornerstone method in biological research.

Multi-focus Strategy

Another way to expand the FOV in light-sheet imaging is by using multiple focal points. Since the usable length of the light sheet is limited to the beam waist near the focal point, employing multiple focal points effectively stitches together several usable beam waists, thereby extending the illumination range, further forming light-sheet illumination through methods such as galvo-lens scanning. The image below illustrates three methods for generating multi-focus light sheets.

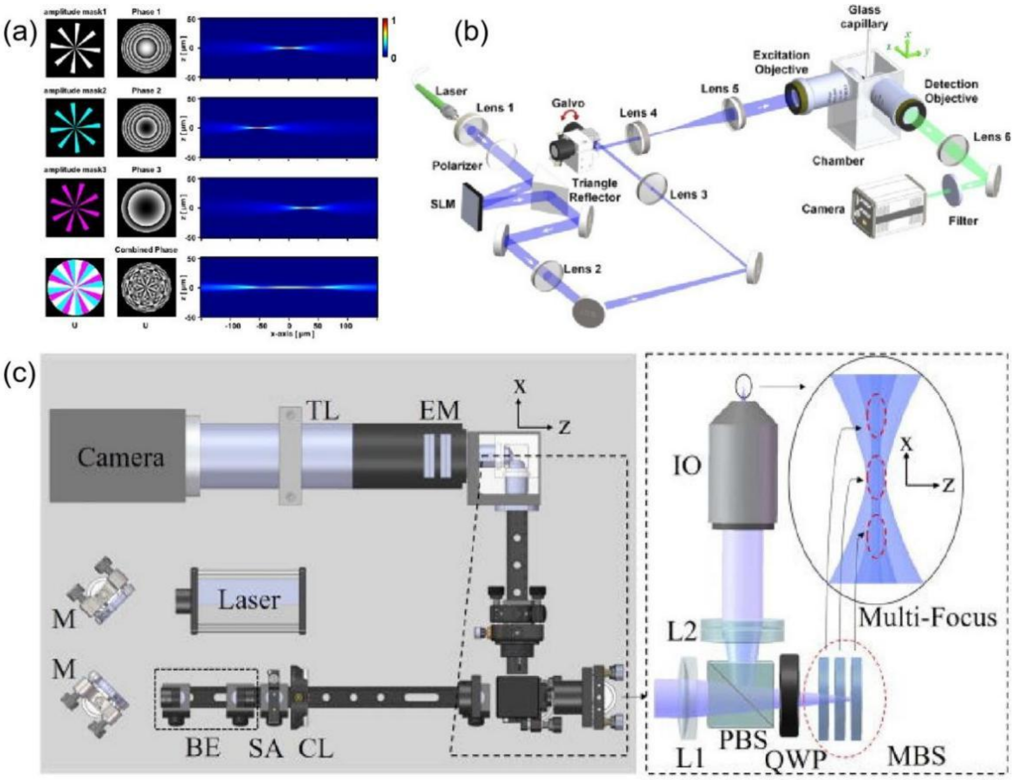

Figure 1-23. Methods for generating multi-focus light sheets. *(a) Liu et al.. modulated the incident light using different regions of an SLM to generate multiple axial focal points in a continuous manner[71]. (b) Liu et al.. used a holographic algorithm to modulate an array of Gaussian spots with an SLM and then achieved large-field light-sheet illumination through galvo lens scanning[72]. (c) Li et al.. used reflections from multiple layers of media to simultaneously generate multiple focal points at different distances from the objective lens, thereby extending the usable range of the light sheet[73].*

B. Axial Scanning Strategy

Axial scanning is a powerful method for expanding the FOV in light-sheet microscopy while maintaining high resolution. By dynamically shifting the position of the light sheet along the axial (z-axis) direction, it allows sequential illumination of different sample layers, enabling comprehensive 3D imaging. This technique can be achieved through motorized sample stage movement, tunable lenses, or dynamic optical systems like AODs. Axial scanning preserves the light sheet's focus at each layer, ensuring high resolution and reducing photodamage by illuminating only the regions of interest. It is particularly suited for imaging large biological samples, such as embryos and organ models, making it an essential tool for advanced volumetric imaging.

In 2022, Kevin et al. introduced Axially Swept Light-Sheet Microscopy (ASLM), a technique designed to achieve isotropic resolution across spatial scales[74]. By dynamically sweeping the excitation light sheet along the optical axis during camera exposure, they eliminated the axial elongation common in conventional light-sheet microscopy. This innovation enabled uniform 3D imaging with high resolution while reducing phototoxicity and photobleaching. The method was demonstrated on live embryos, organoids, and neuronal structures, showcasing its ability to image large volumes with subcellular precision. ASLM represents a significant advancement in volumetric imaging, combining extended fields of view with isotropic resolution, thus addressing key limitations of traditional light-sheet techniques.

1.4.2.2 Improvement in Lateral Resolution

Enhancing lateral resolution in light-sheet microscopy is critical for achieving finer imaging of biological structures. Several strategies have been developed to address the challenges of lateral resolution, leveraging advanced illumination, localization techniques, and computational approaches.

A. Structured Illumination Modulation

Structured illumination microscopy (SIM) techniques have been adapted to light-sheet microscopy to surpass the diffraction limit. By projecting periodic patterns of light onto the sample, structured illumination modulates the fluorescence signal, enabling the extraction of higher spatial frequency information. This strategy doubles the effective resolution laterally and has been successfully applied in lattice light-sheet microscopy[74]. Lattice patterns formed by the interference of multiple Bessel beams or Gaussian beams enhance contrast and suppress background noise while maintaining a thin, uniform light sheet. This approach is particularly useful for live-cell imaging, where phototoxicity must be minimized and fine subcellular details need to be resolved. In addition to lattice light sheets, there are other modulation patterns, such as Bessel droplets[75]. This illumination method can effectively suppress the side lobes of Bessel beams and generate a dashed-line structured light pattern. Combining scanning and phase shifting, it enables super-resolution imaging within the plane of the light sheet.

Another method for generating structured light sheets involves the combination of structured illumination microscopy (SIM) and light-sheet microscopy with orthogonal beam alignment, as demonstrated by Kenta et al[76]. In this approach, SIM provides structured excitation at the fluorophore’s excitation wavelength, while a 405 nm light-sheet beam serves as an activation source. These two beams overlap in a defined plane, creating selective excitation regions. Alexa dyes are employed to ensure that fluorescence is only triggered within the intersecting area of the SIM and light-sheet beams. This dual-wavelength technique allows precise spatial control of fluorescence excitation, reducing background noise and photodamage, while enabling high-resolution imaging in three dimensions, especially for live-cell applications.

B. Single-molecule Localization Strategy

Single-molecule localization techniques, such as PALM (Photoactivated Localization Microscopy) and STORM (Stochastic Optical Reconstruction Microscopy), have been integrated with light-sheet microscopy to achieve nanoscale resolution. By sparsely activating fluorescent molecules and fitting their point spread functions (PSFs) to determine precise locations, these methods break the diffraction limit. When combined with light-sheet illumination, single-molecule localization enables imaging of dynamic molecular interactions and super-resolution mapping of organelle structures. This approach is ideal for capturing intricate cellular details with minimal photobleaching and phototoxicity.

Felix et al. combined dSTORM with lattice light-sheet microscopy to achieve high-resolution imaging of receptor distribution and mobility[77]. Their results demonstrated that the distribution and mobility of receptors remain largely unaffected by contact with the coverslip, indicating that the basal plasma membrane's physical interaction with the substrate does not significantly alter receptor behavior. However, the study also revealed that the measured localization densities at the basal plasma membrane are generally lower, which the authors attribute to limited accessibility for antibodies in this region. This limitation likely arises from steric hindrance or physical barriers that restrict antibody binding, emphasizing the challenges of achieving uniform labeling in confined cellular environments. The integration of dSTORM and lattice light-sheet microscopy in this work highlights the potential for detailed super-resolution imaging of membrane dynamics, while also pointing to critical factors, such as antibody penetration, that must be considered in such studies.

1.4.3 Illumination Angle Modulation and Scattering Imaging

Scattering imaging is a label-free imaging technique that enables the visualization of structures within highly scattering or inhomogeneous media. Unlike fluorescence-based methods, which rely on specific molecular markers, scattering imaging leverages intrinsic light-matter interactions to reveal structural and refractive index variations in biological tissues and other complex materials. However, due to multiple scattering and diffraction effects, conventional imaging methods often suffer from reduced resolution and contrast.

Illumination angle modulation plays a critical role in overcoming these limitations by controlling how light interacts with the medium. The angle of incident light affects both scattering and diffraction, altering the spatial frequency components that contribute to image formation. At low illumination angles, light primarily interacts with low-frequency components, limiting the achievable resolution. In contrast, high-angle illumination introduces additional high-frequency information, which can enhance edge detection and improve overall image sharpness.

1.4.3.1 Principle of Scattering Microscopy Imaging

When light propagates through biological tissues, nanomaterials, or heterogeneous media, it undergoes scattering due to spatial variations in the refractive index. These variations arise from intracellular structures such as organelles, membranes, and protein complexes, which have different optical properties compared to the surrounding cytoplasm.

Scattering in biological cells can serve both as a challenge and an opportunity in imaging. On one hand, it can blur images and reduce resolution by introducing multiple scattering events, leading to a loss of structural information. On the other hand, analyzing scattered light provides critical insights into cellular morphology, enabling high-contrast imaging of unstained and live cells.

Scattering-based microscopy methods extract structural information by measuring angle-dependent scattering, phase shifts, and intensity variations of the scattered light. Techniques such as quantitative phase imaging (QPI), optical coherence tomography (OCT), and dark-field microscopy leverage these effects to reconstruct the sample's internal architecture with high resolution and enhanced contrast. Additionally, computational methods, such as inverse scattering reconstruction and machine-learning-assisted phase retrieval, further improve image clarity by compensating for multiple scattering effects.

By harnessing the optical scattering properties of biological structures, modern imaging techniques can visualize subcellular features, detect early disease markers, and provide label-free diagnostics, making scattering-based microscopy a powerful tool in biomedical research and clinical applications.

Scattering types can be classified based on the size of the scattering particles into Rayleigh scattering and Mie scattering. When the particle size is much smaller than the wavelength of light (e.g., protein molecules, ribosomes, and small organelles), Rayleigh scattering dominates. When the particle size is comparable to or slightly larger than the wavelength of light (200 nm ~ 2 μm), Mie scattering occurs. The structures inside the cell fall within the transition region, where both theories are applicable. According to the Rayleigh scattering formula, the scattering intensity can be expressed as:

$$I = I_0 \cdot \frac{8\pi^4\alpha^2}{\lambda^4 R^2} \cdot (1 + \cos^2\theta) \tag{1-46}$$

Where:

I is the scattered intensity,

I_0 is the incident light intensity,

α is the polarizability of the particle,

λ is the wavelength of the incident light,

R is the distance from the scattering particle to the detector,

θ is the scattering angle.

This equation shows that Rayleigh scattering intensity is inversely proportional to the fourth power of the wavelength ($I \propto \lambda^4$), meaning shorter wavelengths (blue light) scatter more strongly than longer wavelengths (red light).

1.4.3.2 Frequency Shift Due to Oblique Illumination

Previously, I discussed the diffraction limit and the point spread function (PSF), which define the fundamental resolution constraints of an optical system. In structured illumination microscopy (SIM), I utilize high-frequency light field encoding to shift certain high-frequency components into the system’s optical transfer function (OTF). This frequency-shifting approach extends the system's detectable spatial frequencies, ultimately reconstructing a super-resolution image.

Here, I explore an alternative method with high-angle oblique illumination, which also enhances resolution by introducing a lateral frequency shift in Fourier space. The frequency shift induced by oblique illumination is given by the equation:

$$K_{\mathrm{illumination}} = \frac{2n\pi\sin\alpha}{\lambda} \tag{1-47}$$

Where:

$K_{\mathrm{illumination}}$ is the spatial frequency shift induced by oblique illumination,

n is the refractive index of the medium,

α is the illumination angle relative to the optical axis,

λ is the wavelength of the illumination light.

By tilting the illumination beam at a large angle, the high-frequency components of the sample are mapped into the system's passband, making them detectable. This method effectively extends the spatial bandwidth, allowing retrieval of finer details beyond the diffraction limit. In the following sections, I analyze the impact of different illumination angles and how multi-angle oblique illumination further enhances resolution in microscopy.

1.4.3.3 Rotating Coherent Scattering (ROCS) Microscopy

ROCS microscopy is an advanced label-free super-resolution imaging technique that enhances contrast and spatial resolution by exploiting high-speed, oblique, and rotating coherent illumination. Unlike traditional fluorescence microscopy, ROCS utilizes scattered light from the sample, enabling high-speed, high-contrast imaging of cellular structures and dynamic processes without photobleaching or phototoxicity.

ROCS microscopy achieves super-resolution imaging by utilizing rotating total internal reflection fluorescence (TIRF) illumination. At high numerical apertures (NA), different illumination angles produce phase-shifted scattered wavefronts. When these wavefronts are coherently combined, they result in spatial frequency filtering, where certain structures become enhanced or suppressed due to interference effects.

ROCS leverages this phenomenon by sequentially acquiring images under different illumination angles and computationally summing the coherent scattering contributions from multiple angles. This process effectively extends the spatial frequency bandwidth, allowing the reconstruction of a super-resolved image beyond the diffraction limit. By integrating these scattered wavefronts, ROCS enhances contrast and reveals high-frequency structural details, making it highly effective for live-cell imaging, membrane dynamics studies, and high-speed nanostructure visualization.

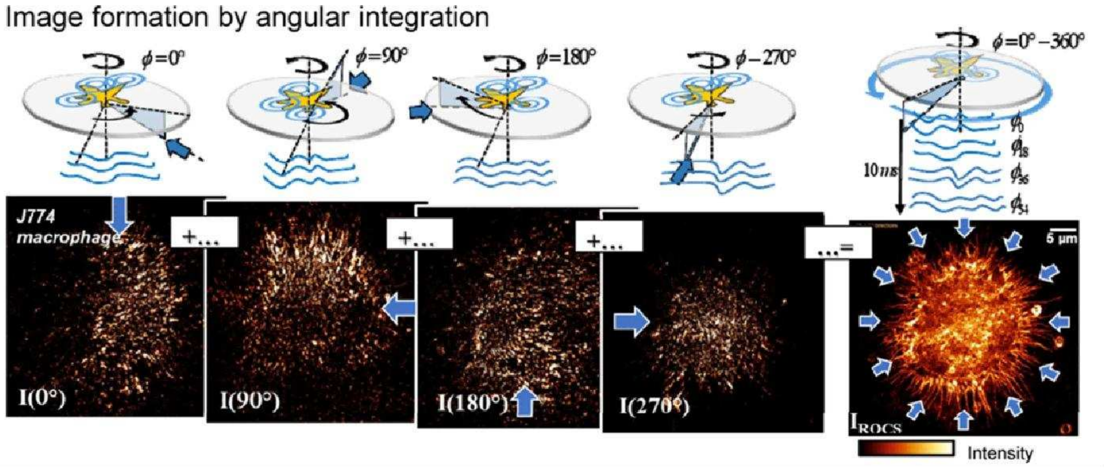

Figure 1-24. Principle of ROCS Super-resolution Imaging [78].

In ROCS, the detected intensity at each point results from the superposition of multiple scattered waves from different illumination directions. Mathematically, the total scattered field at a given point E_{total} is given by:

$$E_{\text{total}}(x,y) = \sum_i E_i\,(x,y)e^{i\phi_i} \tag{1-48}$$

Where:

$E_{\text{i}}(x,y)$ is the scattered field under illumination angle,

ϕ_i is the phase shift introduced by each different illumination angle.

For certain spatial frequencies, destructive interference occurs when the phase shifts align in such a way that:

$$\sum_i \quad e^{i\phi_i} \approx 0 \tag{1-49}$$

This leads to partial or complete cancellation of specific structural details, effectively acting as a high-pass filter that removes low-frequency background noise while emphasizing fine details.

ROCS microscopy leverages interference-induced destructive superposition to suppress unwanted background and low-frequency components, naturally enhancing contrast and high-resolution details. By combining coherent scattering, multi-angle illumination, and phase superposition, ROCS achieves super-resolution without complex computational post-processing, making it a powerful tool for label-free, high-speed imaging in biological and material science applications.

1.4.4 Light Field Modulation via Multimode Fiber

Light propagation in complex media is significantly more intricate than in free space, posing both fundamental challenges and exciting research opportunities. From solving the propagation of optical fields through scattering media to achieving imaging through multimode fibers as thin as a human hair, these ideas are not only fascinating but also highly impactful. A multimode fiber (MMF) behaves as a complex scattering medium due to modal dispersion[79]. While speckle formation appears random, light propagation in a static medium is deterministic, allowing precise control through wavefront shaping and transfer matrix calibration[80]. Since 2010, multimode fiber (MMF) imaging based on transfer matrix (TM) measurement has undergone rapid advancements[81], leading to the development of a range of techniques with practical value and significant application potential.

These methods include digital phase conjugation, transfer matrix algorithms, compressed sensing, and deep learning, fully demonstrating the capabilities of MMF imaging. Among them, the TM approach has attracted particular attention due to its ability to comprehensively characterize fiber transmission while offering a straightforward measurement process. However, in real-world applications, factors such as fiber length variations and environmental fluctuations can affect the stability of the transfer matrix, necessitating frequent recalibrations. To address this, researchers have proposed various stabilization and compensation strategies, enhancing the robustness of MMF-based imaging systems[82-84].

With the advancement of computational optics and machine learning, deep-learning-based techniques have also been introduced into the MMF imaging field[85-88]. By training neural networks, researchers have successfully reconstructed original images from complex speckle patterns, significantly improving image quality and processing speed. These breakthroughs have expanded the potential applications of multimode fibers in biomedical imaging, optical communication, and beyond, paving the way for next-generation high-resolution, compact imaging systems. Next chapter introduces several active and passive methods for light field modulation and imaging through multimode fibers.

1.4.4.1 transfer matrix Method

A. Transmission Modes Supported by Optical Fibers

Multimode fibers (MMFs) can typically support thousands of modes within their core. For a step-index multimode fiber, the number of supported modes can be expressed as[89]:

$$N = \frac{1}{2}\left(\frac{\pi d NA}{\lambda}\right) \tag{1-37}$$

Where d is the core diameter, NA is the numerical aperture, and λ is the wavelength of the incident light. The modes supported by the fiber can be obtained by solving the electromagnetic wave equation in cylindrical coordinates[90].

In cylindrical coordinates (r, ϕ, z), the wave equation for the electric field E or magnetic field

H in a fiber is:

$$\nabla^2 E + k^2 n^2 E = 0 \tag{1-38}$$

Where:

∇ is Laplacian operator

k is the wave number in free space,

n is the refractive index

The radial component follows the characteristic equation:

$$\frac{uJ_{l-1}(u)}{J_l(u)} + \frac{\sqrt{V^2-u^2}K_{l-1}(\sqrt{V^2-u^2})}{K_l(\sqrt{V^2-u^2})} = 0 \tag{1-39}$$

Where:

$J_l(x)$ is the Bessel function of the first kind.

$K_l(\sqrt{V^2 - u^2})$ is the modified Bessel function of the second kind.

u is the normalized radial parameter.

V is the fiber's normalized frequency (V-number):

$$V = \frac{2\pi a}{\lambda}\sqrt{n_{core}^2 - n_{clad}^2} \tag{1-40}$$

Which determines the number of modes supported in the fiber.

For the core region $r < a$:

$$F_R(r) = J_l\left(u\frac{r}{a}\right)/J_l(u) \tag{1-41}$$

For the cladding region $r > a$:

$$F_R(r) = K_l\left(u\frac{r}{a}\right)/K_l(u) \tag{1-42}$$

The phase component is:

$$\psi_{lm}(r, \phi) = F_R(r)e^{il\phi} \tag{1-43}$$

Where:

ϕ is the azimuthal coordinate.

The above equations describe a theoretically orthogonal basis set for the optical field propagating within a multimode fiber. The optical field at any given propagation plane can be expressed as a combination of these basis modes.

A theoretical approach is to directly compute the output optical field of the fiber through numerical simulations. However, factors such as fiber deformation, structural imperfections, and measurement inaccuracies introduce deviations between the actual transmitted field and the theoretically predicted distribution.

B. Transfer Matrix Measurement

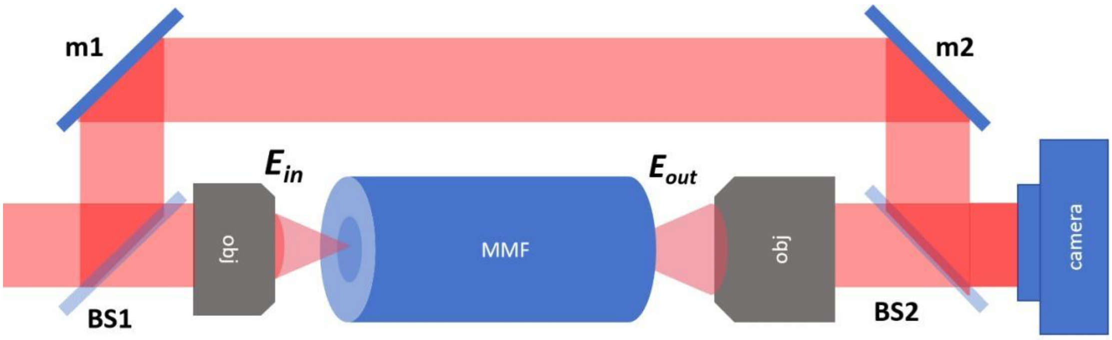

Figure 1-25. Measurement of Complex Wave Propagation Through a Single Multimode Fiber.

For spatial-domain transmission matrices, the input and output optical fields must be discretized into a set of mutually orthogonal modes. The output optical field corresponding to a given mode m can be expressed as a linear combination of different input modes n:

$$E_m^{\text{out}} = \sum_n k_{mn} E_n^{\text{in}} \tag{1-44}$$

Where E^{out} represents the output optical field, E^{in} is the input optical field, and k_{mn} is the complex coefficient linking the n^{th} input mode to the m^{th} output mode. First, the input plane (such as an SLM plane or the fiber input facet) and the output plane (such as a camera plane or the fiber output facet) are discretized. An interference system is established by introducing a reference beam, as shown in Figure 1-25. By controlling the SLM and using phase-shifting interferometry, the transfer matrix is computed from the recorded speckle patterns at the output.

The pre-calibrated transfer matrix allows precise control of the MMF output field. A series of focused spots are formed at the fiber output, scanning across the object. The reflected light from the object is collected back into the same multimode fiber and detected by a photodetector, measuring intensity information. Alternatively, the inverse transfer matrix can be used to reconstruct the input optical field directly from the speckle patterns at the near-end output of the fiber.

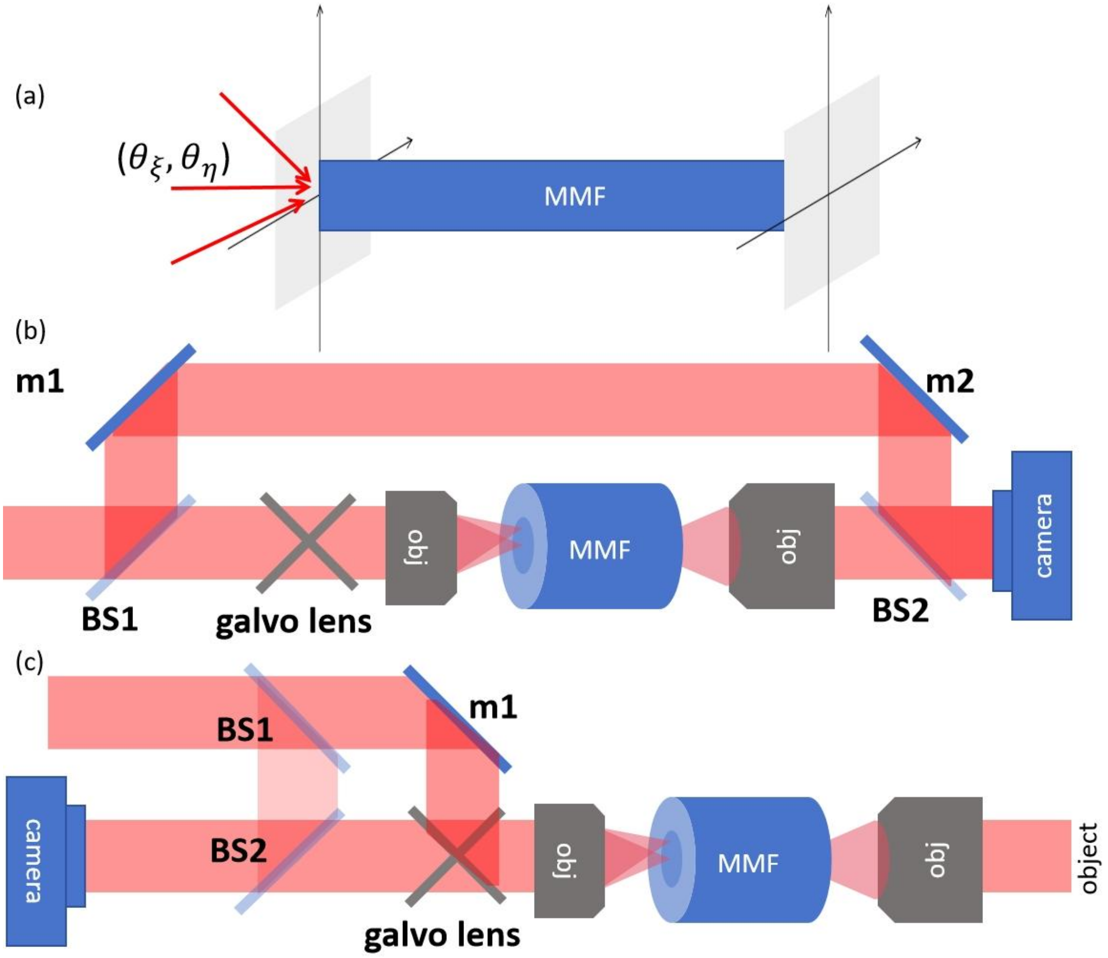

Figure 1-26. Measurement of fiber transfer matrix in the frequency domain. (a) Laser incident angle scanning. (b) Schematic diagram of the transfer matrix measurement system using galvanometer scanning. (c) Schematic illustration of fiber-scanning imaging.obj: Objective lens; BS: Beam splitter; m: Mirror. MMF: multimode fiber

In addition to the spatial-domain transfer matrix, the frequency-domain transfer matrix describes the response of the MMF to different spatial frequencies of the input light field. The basic principle of frequency-domain transfer matrix measurement is illustrated in Figure 1-26. By varying the incident plane wave angle $(\theta_\xi, \theta_\eta)$at the fiber input, the corresponding output optical field can be expressed as:

$$E(x, y, \theta_\xi, \theta_\eta) \tag{1-45}$$

The Camera-in-the-Loop[91] (CIL) Iteration Method is a feedback-based wavefront shaping technique that optimizes phase modulation on a SLM using real-time intensity measurements from a camera. By iteratively adjusting the phase of individual SLM segments, the method maximizes intensity at a target location without requiring prior knowledge of the TM. Each segment's phase is scanned, and the optimal value is retained to enhance constructive interference. This approach is widely used in focusing through MMF, imaging through scattering media, optical trapping, and laser beam shaping. The key advantages of CIL include adaptability to dynamic environments, improved focusing efficiency, and applicability to complex optical systems.

1.4.4.2 Phase Conjugation Method

The Phase Conjugation Method is an advanced approach for controlling optical fields at the distal end of multimode fibers (MMF). It enables the precise reconstruction of a desired optical field by first generating the target field at the output, measuring its back-propagated wavefront at the input, and then applying phase conjugation to reverse the propagation distortions. The system is as shown in Figure 1-27.This method effectively cancels out modal scrambling within the fiber, making it highly effective for structured light delivery in complex optical environments.

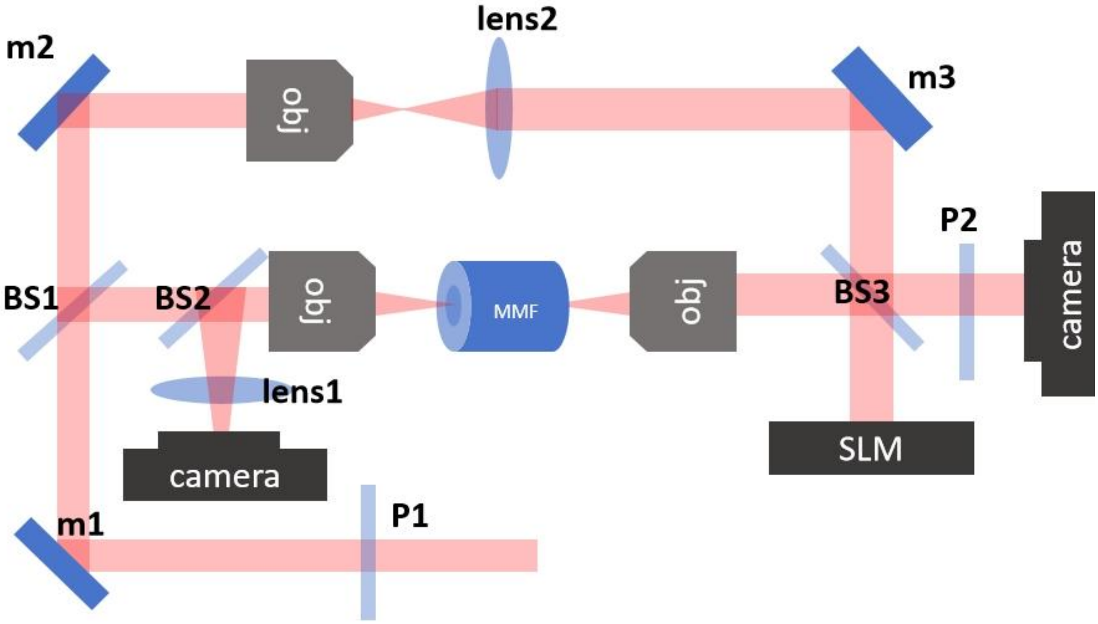

Figure 1-27. Schematic diagram of the fiber imaging system based on phase conjugation. ***obj: Objective lens; BS: Beam splitter; m: Mirror. MMF: multimode fiber; P: polarizer; SLM: spatial light modulator.***

The process involves four key steps: first, a structured optical field (such as a focused spot or pattern) is generated at the distal tip of the fiber. This field naturally propagates backward through the MMF, undergoing mode mixing and resulting in a complex wavefront at the proximal end. The distorted wavefront is then measured using an interferometric or holographic technique, providing the input optical field required for correction. A phase-conjugate version of this measured field is then computed and displayed on a SLM to modulate the incident beam. Finally, the modulated beam is re-injected into the fiber, where it retraces the modal distortions and reconstructs the exact desired field at the distal tip.

This technique has significant advantages, including its ability to restore complex light fields at the fiber output, compensate for modal scrambling without requiring full TM inversion, and operate at high speeds for real-time correction. It is widely used in fiber-based holographic imaging, endoscopic microscopy, optical communication, and laser beam delivery. By overcoming the limitations of conventional MMF-based light control, the Phase Conjugation Method has become a key enabling technology for structured light delivery through multimode fibers.

1.4.4.3 Camera-in-Loop Phase Optimization

Beyond phase conjugation methods, researchers have developed phase optimization techniques to achieve more precise and adaptive wavefront control in multimode fiber (MMF) imaging. These methods iteratively refine the input phase to optimize the transmitted optical field, enabling high-resolution imaging through the fiber. The system setup is the same as Figure 1-25.

The approach involves using SLM or DMD to modulate the input wavefront, with a camera capturing the output speckle pattern for feedback. A computational optimization algorithm then iteratively adjusts the phase pattern on the SLM based on the detected output, gradually refining the wavefront until the desired optical field is reconstructed at the fiber's distal end.

This technique allows for real-time phase correction, adapting dynamically to environmental variations such as mechanical perturbations and temperature changes that can affect fiber transmission. Compared to phase conjugation, phase optimization provides greater flexibility and does not require prior knowledge of the transfer matrix. It significantly enhances imaging resolution, contrast, and stability, making MMF-based imaging suitable for applications such as deep-tissue imaging, optical trapping, and structured light generation.

1.4.4.4 Speckle Structured Illumination

Compressed imaging using structured illumination has recently emerged as an innovative approach for multimode fiber (MMF) imaging. Instead of actively correcting modal scrambling, this method leverages the random speckle patterns generated at the MMF output as a form of structured illumination. During calibration, a series of low-correlation speckle patterns are recorded by controlling the wavefront of the input light. In the imaging phase, these pre-recorded speckle patterns illuminate the object, and a single-pixel detector collects the reflected intensity. The image reconstruction process is based on compressed sensing algorithms, which allow high-resolution imaging with significantly fewer measurements.

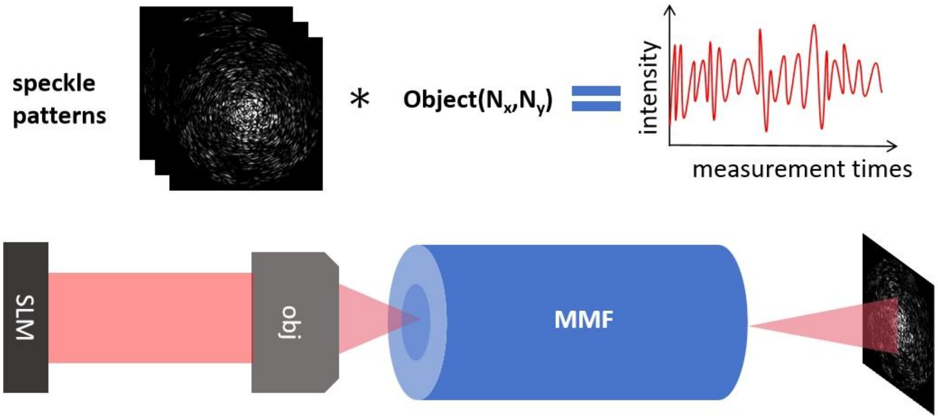

Figure 1-28. Schematic diagram of multimode fiber imaging principle based on speckle illumination.

Compared to traditional MMF imaging techniques, compressed imaging eliminates the need for transfer matrix measurement or iterative wavefront correction, simplifying both the calibration process and optical setup. Additionally, compressed sensing enables high-quality reconstruction with a reduced number of sampling measurements, significantly improving imaging speed and efficiency.

The first application of speckle-illumination-based MMF imaging was demonstrated in 2013 by Mahalati et al. at Stanford University[92], showing that the number of resolvable image features could be significantly increased by leveraging speckle illumination. In 2018, Amitonova et al. from Vrije University Amsterdam[93] introduced a fluorescence-based MMF compressed imaging system, achieving diffraction-limited resolution with 20 × fewer measurements than conventional scanning-based MMF imaging. In 2019, Caravaca-Aguirre et al. at Grenoble Alpes University[94] extended this technique to photoacoustic imaging, combining MMFs with fiber-optic hydrophones for multimodal imaging of biological samples.

Further advancements have focused on improving the generation of low-correlation structured illumination patterns. In 2020, Fukui et al. from Tokyo University[95] demonstrated an MMF imaging system using chip-integrated optical phased arrays (OPA), allowing compact, high-speed speckle pattern generation. In 2022, Zhu et al. from Nanjing University developed a long working distance and large FOV all-fiber imaging system based on single-pixel imaging[96]. Similarly, Dong et al. from Zhejiang University[97] proposed a sparsity-enhanced MMF 3D compressed imaging method, using structured wavefronts to achieve volumetric imaging of biological tissues at an axial depth range of 0–200 μm.

With its ability to reduce sampling requirements and achieve super-resolution imaging, compressed imaging based on structured illumination has become a promising technique for fiber-based biomedical imaging, hyperspectral imaging, and low-light optical sensing. Recent developments in wavefront shaping, deep learning, and integrated photonics continue to enhance the speed and resolution of MMF-based compressed imaging, making it a valuable approach for high-efficiency fiber imaging systems.

1.4.4.5 Machine Learning-Assisted Multimode Fiber Imaging

With the increasing complexity of multimode fiber (MMF) imaging, machine learning techniques have emerged as a powerful tool to address challenges such as modal scrambling, transmission instability, and complex wavefront reconstruction. Instead of explicitly measuring the transfer matrix or applying iterative corrections, deep learning models learn the mapping between the fiber's speckle output and the original input optical field, enabling rapid and accurate image reconstruction.

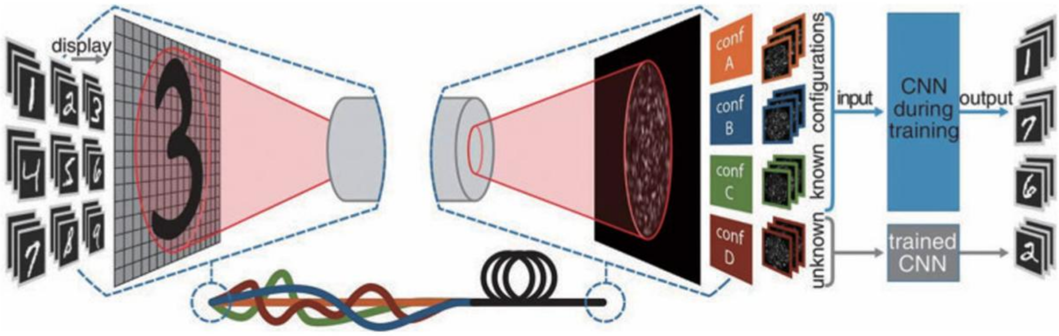

Figure 1-29. Image transmission through a dynamically perturbed multimode fiber by deep learning[98].

In the training step, a large dataset of known input-output pairs is collected to train convolutional neural networks (CNNs) or other deep-learning architectures. Once trained, the model can directly predict the input field from a new speckle pattern, bypassing the need for explicit phase retrieval or transfer matrix inversion. This approach significantly enhances imaging speed, robustness, and adaptability, especially in dynamic environments where the fiber may undergo bending or external perturbations.

Early applications of machine learning in MMF imaging include 2018 work by Rahmani et al.[85], who used a deep convolutional neural network (CNN) to reconstruct input images from multimode fiber speckle patterns. In 2021, Li et al.[99] proposed a method using deep learning-assisted transfer matrix calibration, allowing real-time MMF image recovery. In 2021, Deng et al. developed an end-to-end deep learning framework that directly learns the inverse mapping of light propagation through an MMF, significantly improving real-time imaging performance[100].

Further improvements have been made by integrating deep learning with compressed imaging, enabling high-speed single-shot reconstruction of complex optical fields. In 2022 Bagley et al. Reconstruct image through disturbed multimode fiber by training single-layer network with multiple fiber states[98]. The use of physics-informed neural networks (PINNs) and generative adversarial networks (GANs) has further expanded the potential of machine learning for MMF-based imaging, allowing for robust imaging in low-light and dynamic environments[87, 101].

Compared to traditional MMF imaging techniques, machine learning-based approaches offer higher resilience to noise, greater generalization across varying conditions, and real-time processing capabilities. These advantages make it particularly valuable for applications in biomedical imaging, fiber-based endoscopy, and high-speed optical sensing. As computational models and training datasets continue to improve, deep-learning-enhanced MMF imaging is poised to become a key enabler of compact, high-resolution, and intelligent optical imaging systems.

1.4.4.6 Temporal Decoding Fiber Imaging

In addition to spatial-domain wavefront shaping and machine learning techniques, researchers have explored time-domain information extraction as an alternative approach to imaging through multimode fibers (MMFs). This method leverages the fact that different spatial modes in an MMF have distinct group velocities, causing temporal dispersion when a broadband or pulsed light source propagates through the fiber. By analyzing the temporal characteristics of the transmitted light, it becomes possible to reconstruct the original image without the need for complex phase retrieval or transfer matrix calibration.

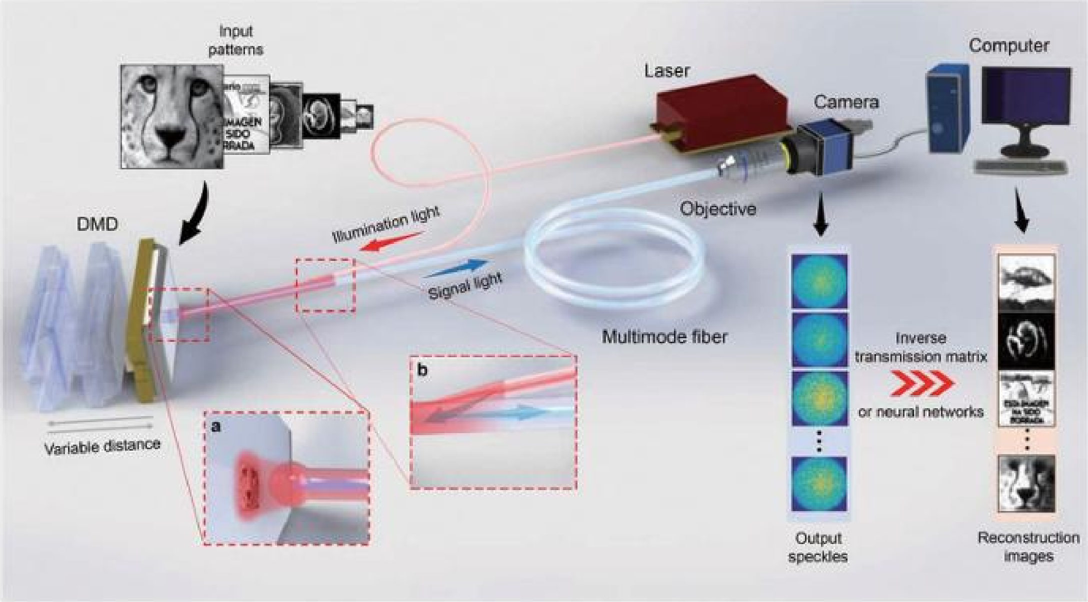

Figure 1-30. High-speed all-fiber micro-imaging with large depth of field[102].

In 2022, Liu et al.[102] from Tsinghua University proposed a high-speed, all-fiber imaging model based on this principle. The imaging system and reconstruction framework are shown in ***Figure 1-30***. The researchers utilized modal dispersion in a 1 km-long MMF to convert 2D spatial information into a 1D temporal pulse stream. By collecting the input images and their corresponding time-domain signals, a dataset was constructed for training a neural network. Once trained, the neural network was capable of reconstructing high-quality images from time-domain waveforms while exhibiting a certain degree of transfer learning ability.

1.5 Discussion

Microscopic imaging is advancing rapidly, and the requirements for light field control are becoming increasingly complex. Designing corresponding illumination light fields based on appropriate application scenarios is an important research direction in microscopic imaging. Below, we summarize the opportunities for the development of microscopic imaging showcased by the technologies introduced in sections 1.2 and 1.3, as well as the challenges faced by microscopic imaging technology described in section 1.4.

1.5.1 Orthogonal Light Sheet Illumination

From Figure 1-13, it is evident that light sheet illumination is a versatile method applicable across a wide range of scales and is utilized in multiscale volumetric imaging. Light-sheet illumination has undergone long-term development, leading to the creation of various modulation modes tailored to different scale and resolution requirements. However, this orthogonal illumination mode still presents significant opportunities for further advancements. First, its inherent tomographic properties make it well-suited for fast volumetric imaging. Second, its illumination direction is perpendicular to the detection pathway, reducing laser noise. Finally, its horizontal illumination angle maximizes the scattering angle, allowing the acquisition of the highest-frequency information in scattering imaging.

I have observed that light sheet illumination can be applied to in vivo imaging. However, a major challenge arises due to the complex composition of tissues, which causes significant light absorption and scattering, resulting in a very low signal-to-noise ratio. However, this challenge also presents an opportunity to introduce light sheet imaging in small animals by improving the signal-to-noise ratio.

In the second chapter, I introduced NIR-II dyes and imaging techniques, along with time-gating and deep learning strategies, to enhance the signal-to-noise ratio, enabling volumetric imaging of mouse vasculature using light sheet microscopy. In Chapter 3, I also used the light-sheet illumination mode, but for scattering imaging, which was one of the earliest applications of orthogonal illumination. In Chapter 4, I employed a different light-sheet modulation approach by utilizing multimode fibers for light field control in light-sheet imaging.

1.5.2 Label-free Microscopy

Label-free microscopic imaging will become a key development direction for next-generation microscopic imaging technologies. Compared to fluorescent imaging, label-free imaging exhibits lower phototoxicity, requires no labeling, and has shorter exposure times, making it suitable for long-term imaging of living cells. Therefore, label-free imaging can, to some extent, compensate for the limitations of fluorescence imaging. However, label-free imaging also has drawbacks, such as lower spatial resolution and difficulties in correlating the imaging results with actual structures.

In section 1.4.3, we introduced a scattering-based label-free imaging method called ROCS, which is a reconstruction-free super-resolution imaging technique. Its imaging speed can reach at least 100 Hz, and theoretically, it can offer a much larger field of view and higher imaging speed than fluorescence-based super-resolution imaging techniques. However, this technique is currently limited by its reliance on TIRF illumination for 2D imaging.

In Chapter 3, I attempted to break through the dimensional barrier from 2D to 3D by using light field control to generate rotational or multi-angle light sheet illumination. Once successful, this could lead to an ultrafast, label-free, super-resolution volumetric imaging method. In the future, by integrating fluorescence imaging and computational imaging, dynamic three-dimensional super-resolution imaging and tracking could be achieved.

1.5.3 Fiber Encoded Light Field Modulation

The transmission of light fields in complex media or confined spaces has long been one of the challenges in microscopic imaging. The development of spatial light modulation devices has opened up possibilities for modulating light fields under such complex conditions. In section 1.4.4, I introduced a method for transmitting and modulating light fields via optical fibers, offering a solution for remote light field control. Researchers can achieve in-situ imaging in narrow spaces, such as endoscopic imaging, through the use of optical fibers. Current optical fiber imaging methods are still immature, and measuring the transfer matrix is quite complicated. Although the optical fiber transmission segment is structurally simple, the optical system used for measuring the transfer matrix is highly complex. In Chapter 4, I attempted a new method to measure the transfer matrix using a simplified system, and I also streamlined the computational methods to eliminate extensive calculations. Furthermore, I explored the implementation of light sheet illumination through optical fibers to facilitate the miniaturization and integration of light sheet systems. This approach is also very useful for optical holography and diffractive imaging.

1.6 Reference

1. Chen, X., et al., *Superresolution structured illumination microscopy reconstruction algorithms: a review.* Light: Science & Applications, 2023. **12**(1): p. 172.
2. Power, R.M. and J. Huisken, *A guide to light-sheet fluorescence microscopy for multiscale imaging.* Nature methods, 2017. **14**(4): p. 360-373.
3. Dholakia, K. and T. Čižmár, *Shaping the future of manipulation.* Nature photonics, 2011. **5**(6): p. 335-342.
4. Thorn, K., *A quick guide to light microscopy in cell biology.* Molecular biology of the cell, 2016. **27**(2): p. 219-222.
5. Pan, A., C. Zuo, and B. Yao, *High-resolution and large field-of-view Fourier ptychographic microscopy and its applications in biomedicine.* Reports on Progress in Physics, 2020. **83**(9): p. 096101.
6. Fischer, R.S., et al., *Microscopy in 3D: a biologist's toolbox.* Trends in cell biology, 2011. **21**(12): p. 682-691.
7. Yang, T. and F. Gu, *Overview of modulation techniques for spatially structured-light 3D imaging.* Optics & Laser Technology, 2024. **169**: p. 110037.
8. Heintzmann, R. and G. Ficz, *Breaking the resolution limit in light microscopy.* Briefings in Functional Genomics, 2006. **5**(4): p. 289-301.
9. Suhling, K., P.M. French, and D. Phillips, *Time-resolved fluorescence microscopy.* Photochemical & Photobiological Sciences, 2005. **4**(1): p. 13-22.
10. Torrado, B., et al., *Fluorescence lifetime imaging microscopy.* Nature Reviews Methods Primers, 2024. **4**(1): p. 80.
11. Bond, C., et al., *Technological advances in super-resolution microscopy to study cellular processes.* Molecular Cell, 2022. **82**(2): p. 315-332.
12. Zhang, Q., et al. *Far-field super-resolution microscopy using evanescent illumination: a review*. in *Photonics*. 2024. MDPI.
13. Cano, P., *Integrated Structured Light Architectures: A Review of Modulation Techniques.* 2023.

14. Forbes, A., M. De Oliveira, and M.R. Dennis, *Structured light.* Nature Photonics, 2021. **15**(4): p. 253-262.
15. Zhanghao, K., et al., *Super-resolution fluorescence polarization microscopy.* Journal of Innovative Optical Health Sciences, 2018. **11**(01): p. 1730002.
16. Micó, V., et al., *Resolution enhancement in quantitative phase microscopy.* Advances in Optics and Photonics, 2019. **11**(1): p. 135-214.
17. Yao, A.M. and M.J. Padgett, *Orbital angular momentum: origins, behavior and applications.* Advances in optics and photonics, 2011. **3**(2): p. 161-204.
18. Oldenbourg, R., *Polarized light microscopy: principles and practice.* Cold Spring Harbor Protocols, 2013. **2013**(11): p. pdb. top078600.
19. van Munster, E.B. and T.W. Gadella, *Fluorescence lifetime imaging microscopy (FLIM).* Microscopy Techniques: -/-, 2005: p. 143-175.
20. Fleming, G., *Chemical applications of ultrafast spectroscopy.* 1986.
21. Zhu, Y. and J.-X. Cheng, *Transient absorption microscopy: Technological innovations and applications in materials science and life science.* The Journal of Chemical Physics, 2020. **152**(2).
22. Weiner, A.M., *Femtosecond pulse shaping using spatial light modulators.* Review of scientific instruments, 2000. **71**(5): p. 1929-1960.
23. Kondakci, H.E. and A.F. Abouraddy, *Diffraction-free space–time light sheets.* Nature Photonics, 2017. **11**(11): p. 733-740.
24. Cao, Q., P. Zheng, and Q. Zhan, *Vectorial sculpturing of spatiotemporal wavepackets.* APL Photonics, 2022. **7**(9).
25. Bergen, J.R. and E.H. Adelson, *The plenoptic function and the elements of early vision.* Computational models of visual processing, 1991. **1**(8): p. 3.
26. Grella, R., *Fresnel propagation and diffraction and paraxial wave equation.* Journal of Optics, 1982. **13**(6): p. 367.
27. Matsushima, K., *Shifted angular spectrum method for off-axis numerical propagation.* Optics Express, 2010. **18**(17): p. 18453-18463.
28. Maurer, C., et al., *What spatial light modulators can do for optical microscopy.* Laser & Photonics Reviews, 2011. **5**(1): p. 81-101.
29. Rosales-Guzmán, C. and A. Forbes. *How to shape light with spatial light modulators*. 2017. Society of Photo-Optical Instrumentation Engineers (SPIE).
30. Zhao, T. and Y. Chi, *Modified Gerchberg–Saxton (GS) algorithm and its application.* Entropy, 2020. **22**(12): p. 1354.
31. Nape, I., et al., *Revealing the invariance of vectorial structured light in perturbing media.* arXiv preprint arXiv:2108.13890, 2021.
32. Chen, Z., et al., *Complete shaping of optical vector beams.* Optics express, 2015. **23**(14): p. 17701-17710.
33. Jiao, S., et al., *Complex-amplitude holographic projection with a digital micromirror device (DMD) and error diffusion algorithm.* IEEE Journal of Selected Topics in Quantum Electronics, 2020. **26**(5): p. 1-8.
34. Mitsa, T. and K.J. Parker, *Digital halftoning technique using a blue-noise mask.* Journal of the Optical Society of America A, 1992. **9**(11): p. 1920-1929.

35. Zhang, Z., et al., *Fast Fourier single-pixel imaging via binary illumination.* Scientific reports, 2017. **7**(1): p. 12029.
36. Conkey, D.B., A.M. Caravaca-Aguirre, and R. Piestun, *High-speed scattering medium characterization with application to focusing light through turbid media.* Optics express, 2012. **20**(2): p. 1733-1740.
37. Wang, G., et al., *Ultrafast optical imaging using multimode fiber based compressed sensing and photonic time stretch.* arXiv preprint arXiv:1803.03061, 2018.
38. Roudas, I. *Modeling of modal dispersion in multimode and multicore optical fibers*. in *2017 26th Wireless and Optical Communication Conference (WOCC)*. 2017. IEEE.
39. Tegin, U., et al. *Scalable nonlinear optical computing with multimode fibers*. in *AI and Optical Data Sciences III*. 2022. SPIE.
40. Daetwyler, S. and R.P. Fiolka, *Light-sheets and smart microscopy, an exciting future is dawning.* Communications biology, 2023. **6**(1): p. 502.
41. Zawadzki, R.J., et al., *Adaptive-optics optical coherence tomography for high-resolution and high-speed 3D retinal in vivo imaging.* Optics express, 2005. **13**(21): p. 8532-8546.
42. Rodríguez, C., et al., *An adaptive optics module for deep tissue multiphoton imaging in vivo.* Nature methods, 2021. **18**(10): p. 1259-1264.
43. Ren, Y.-X., et al., *Non-diffracting light wave: fundamentals and biomedical applications.* Frontiers in Physics, 2021. **9**: p. 698343.
44. Wang, F., et al., *In vivo NIR-II fluorescence imaging for biology and medicine.* Nature Photonics, 2024. **18**(6): p. 535-547.
45. Cao, J., et al., *Recent progress in NIR-II contrast agent for biological imaging.* Frontiers in bioengineering and biotechnology, 2020. **7**: p. 487.
46. Zhu, S., et al., *3D NIR-II molecular imaging distinguishes targeted organs with high-performance NIR-II bioconjugates.* Advanced Materials, 2018. **30**(13): p. 1705799.
47. Lee, K.W., et al., *Anti-quenching NIR-II J-aggregates of benzo [c] thiophene fluorophore for highly efficient bioimaging and phototheranostics.* Advanced Materials, 2023. **35**(20): p. 2211632.
48. Kong, S., et al., *Clinical applications of nanoprobes of high-resolution in vivo imaging.* Iscience, 2025. **28**(1).
49. Fei, K., et al., *Present application and perspectives of organoid imaging technology.* Bioengineering, 2022. **9**(3): p. 121.
50. Wang, Z., et al., *LiveLattice: Real-time visualisation of tilted light-sheet microscopy data using a memory-efficient transformation algorithm.* Journal of Microscopy, 2025. **297**(2): p. 123-134.
51. Spahn, C., et al., *Whole-cell, 3D, and multicolor STED imaging with exchangeable fluorophores.* Nano letters, 2018. **19**(1): p. 500-505.
52. Cao, R., et al., *Open-3DSIM: an open-source three-dimensional structured illumination microscopy reconstruction platform.* Nature Methods, 2023. **20**(8): p. 1183-1186.
53. Huang, B., et al., *Whole-cell 3D STORM reveals interactions between cellular structures with nanometer-scale resolution.* Nature methods, 2008. **5**(12): p. 1047-1052.
54. Abbe, E., *Beiträge zur Theorie des Mikroskops und der mikroskopischen Wahrnehmung.* Archiv für mikroskopische Anatomie, 1873. **9**(1): p. 413-468.

55. Rayleigh, N., *XXXI. Investigations in optics, with special reference to the spectroscope.* The London, Edinburgh, and Dublin Philosophical Magazine and Journal of Science, 1879. **8**(49): p. 261-274.
56. Sheppard, C., *Axial resolution of confocal fluorescence microscopy.* Journal of Microscopy, 1989. **154**(3): p. 237-241.
57. Heintzmann, R. and C.G. Cremer. *Laterally modulated excitation microscopy: improvement of resolution by using a diffraction grating*. in *Optical biopsies and microscopic techniques III*. 1999. SPIE.
58. Gustafsson, M.G., *Surpassing the lateral resolution limit by a factor of two using structured illumination microscopy.* Journal of microscopy, 2000. **198**(2): p. 82-87.
59. Tang, J., J. Ren, and K.Y. Han, *Fluorescence imaging with tailored light.* Nanophotonics, 2019. **8**(12): p. 2111-2128.
60. Stelzer, E.H., et al., *Light sheet fluorescence microscopy.* Nature Reviews Methods Primers, 2021. **1**(1): p. 73.
61. Ryan, J., et al., *Introduction to modern methods in light microscopy.* Light Microscopy: Methods and Protocols, 2017: p. 1-15.
62. Masters, B.R., *Richard Zsigmondy and Henry Siedentopf's Ultramicroscope*, in *Superresolution Optical Microscopy: The Quest for Enhanced Resolution and Contrast*. 2020, Springer International Publishing: Cham. p. 165-172.
63. Evanko, D., A. Heinrichs, and C. Rosenthal, *Milestones in light microscopy.* Nature Cell Biol, 2009. **11**: p. S5-S20.
64. Fernández-Suárez, M. and A.Y. Ting, *Fluorescent probes for super-resolution imaging in living cells.* Nature reviews Molecular cell biology, 2008. **9**(12): p. 929-943.
65. Voie, A.H., D. Burns, and F. Spelman, *Orthogonal-plane fluorescence optical sectioning: Three-dimensional imaging of macroscopic biological specimens.* Journal of microscopy, 1993. **170**(3): p. 229-236.
66. Huisken, J., et al., *Optical sectioning deep inside live embryos by selective plane illumination microscopy.* Science, 2004. **305**(5686): p. 1007-1009.
67. Dickson, L.D., *Characteristics of a propagating Gaussian beam.* Applied Optics, 1970. **9**(8): p. 1854-1861.
68. Chen, B.-C., et al., *Lattice light-sheet microscopy: imaging molecules to embryos at high spatiotemporal resolution.* Science, 2014. **346**(6208): p. 1257998.
69. Planchon, T.A., et al., *Rapid three-dimensional isotropic imaging of living cells using Bessel beam plane illumination.* Nature methods, 2011. **8**(5): p. 417-423.
70. Vettenburg, T., et al., *Light-sheet microscopy using an Airy beam.* Nature methods, 2014. **11**(5): p. 541-544.
71. Liu, P., et al., *Systematic and quantitative comparison of axially overlapped multi-focus and Gaussian light sheets.* Optics and Lasers in Engineering, 2024. **181**: p. 108355.
72. Liu, C., et al., *Extended field of view of light-sheet fluorescence microscopy by scanning multiple focus-shifted Gaussian beam arrays.* Optics Express, 2021. **29**(4): p. 6158-6168.
73. Li, H., et al., *Axially overlapped multi-focus light sheet with enlarged field of view.* Applied Physics Letters, 2021. **118**(22).
74. Dean, K.M., et al., *Isotropic imaging across spatial scales with axially swept light-sheet microscopy.* Nature protocols, 2022. **17**(9): p. 2025-2053.

75. Chen, W., et al., *Bessel-droplet foci enable high-resolution and high-contrast volumetric imaging of synapses and circulation in the brain in vivo.* bioRxiv, 2022: p. 2022.03. 05.483143.

76. Temma, K., et al., *Selective-plane-activation structured illumination microscopy.* Nature Methods, 2024. **21**(5): p. 889-896.

77. Wäldchen, F., et al., *Whole-Cell imaging of plasma membrane receptors by 3D lattice light-sheet d STORM.* Nature communications, 2020. **11**(1): p. 887.

78. Jünger, F., et al., *100 Hz ROCS microscopy correlated with fluorescence reveals cellular dynamics on different spatiotemporal scales.* Nature Communications, 2022. **13**(1): p. 1758.

79. Zhu, R. and F. Xu, *Multimode fiber imaging based on temporalspatial information extraction.* Laser & Optoelectronics Progress, 2023. **60**(11): p. 1106011.

80. Goodman, J.W., *Speckle phenomena in optics: theory and applications*. 2007: Roberts and Company Publishers.

81. Popoff, S.M., et al., *Measuring the Transmission Matrix in Optics: An Approach to the Study and Control<? format?> of Light Propagation in Disordered Media.* Physical review letters, 2010. **104**(10): p. 100601.

82. Farahi, S., et al., *Dynamic bending compensation while focusing through a multimode fiber.* Optics express, 2013. **21**(19): p. 22504-22514.

83. Gu, R.Y., R.N. Mahalati, and J.M. Kahn, *Design of flexible multi-mode fiber endoscope.* Optics express, 2015. **23**(21): p. 26905-26918.

84. Gordon, G.S., et al., *Characterizing optical fiber transmission matrices using metasurface reflector stacks for lensless imaging without distal access.* Physical review X, 2019. **9**(4): p. 041050.

85. Rahmani, B., et al., *Multimode optical fiber transmission with a deep learning network.* Light: science & applications, 2018. **7**(1): p. 69.

86. Borhani, N., et al., *Learning to see through multimode fibers.* Optica, 2018. **5**(8): p. 960-966.

87. Yu, Z., et al., *High-speed multimode fiber imaging system based on conditional generative adversarial network.* Chinese Optics Letters, 2021. **19**(8): p. 081101.

88. Song, B., et al., *Deep learning image transmission through a multimode fiber based on a small training dataset.* Optics express, 2022. **30**(4): p. 5657-5672.

89. Redding, B., S.M. Popoff, and H. Cao, *All-fiber spectrometer based on speckle pattern reconstruction.* Optics express, 2013. **21**(5): p. 6584-6600.

90. Plöschner, M., et al., *Multimode fibre: Light-sheet microscopy at the tip of a needle.* Scientific reports, 2015. **5**(1): p. 18050.

91. Choi, S., et al. *High-quality holographic displays using double SLMs and camera-in-the-loop optimization*. in *Optical Architectures for Displays and Sensing in Augmented, Virtual, and Mixed Reality (AR, VR, MR) II*. 2021. SPIE.

92. Mahalati, R.N., R.Y. Gu, and J.M. Kahn, *Resolution limits for imaging through multi-mode fiber.* Optics express, 2013. **21**(2): p. 1656-1668.

93. Amitonova, L.V. and J.F. De Boer, *Compressive imaging through a multimode fiber.* Optics letters, 2018. **43**(21): p. 5427-5430.

94. Caravaca-Aguirre, A.M., et al., *Hybrid photoacoustic-fluorescence microendoscopy through a multimode fiber using speckle illumination.* Apl Photonics, 2019. **4**(9).

95. Fukui, T., et al. *Single-pixel imaging through multimode fiber using silicon optical phased array chip*. in *Optical Fiber Communication Conference*. 2020. Optica Publishing Group.

96. Zhu, R.-z., et al., *All-fiber reflective single-pixel imaging with long working distance.* Optics & Laser Technology, 2023. **158**: p. 108909.

97. Dong, Z., et al., *A modulated sparse random matrix for high-resolution and high-speed 3D compressive imaging through a multimode fiber.* Science bulletin, 2022. **67**(12): p. 1224-1228.

98. Bagley, N., et al., *Transfer learning and generalization of a neural-network-based multimode fiber position and imaging sensor under thermal perturbations.* Optical Fiber Technology, 2022. **70**: p. 102855.

99. Li, S., et al., *Compressively sampling the optical transmission matrix of a multimode fibre.* Light: science & applications, 2021. **10**(1): p. 88.

100. Deng, L., et al., *Characterization of an imaging multimode optical fiber using a digital micro-mirror device based single-beam system.* Optics express, 2018. **26**(14): p. 18436-18447.

101. Gao, H., et al., *Seeing through multimode fibers with physics-assisted deep learning.* Optics & Laser Technology, 2023. **167**: p. 109761.

102. Liu, Z., et al., *All-fiber high-speed image detection enabled by deep learning.* Nature communications, 2022. **13**(1): p. 1433.

2 Light-Sheet modulation for In Vivo Imaging of Small Animals

2.1 Background

The field of small-animal imaging has seen remarkable progress, particularly in volumetric imaging for live animals. Advances in second near-infrared (NIR-II) fluorescence imaging have significantly expanded the capability to visualize structures deep within tissues, overcoming traditional challenges such as scattering and absorption[1]. As the fluorescence emission wavelength increases, the degree of fluorescence scattering by the tissue decreases. The wavelength of the NIR-II fluorescence window ranges from 1000 to 1700 nm. Due to its low scattering properties, researchers have developed various agents[2-4] and systems. Recent advancements in volumetric imaging systems can be evaluated based on four key parameters: resolution, imaging speed, penetration depth, and field of view. In 2010, Welsher K et al. demonstrated that selecting wavelengths between 1 and 1.4 μm could optimize penetration depth[5]. In 2012, Hong et al. introduced single-walled carbon nanotubes for NIR-II fluorescence imaging, achieving a spatial resolution of approximately 30 μm, a rapid acquisition time of under 200 ms, and tissue penetration reaching 3 mm[6]. In 2014, their research advanced to through-skull fluorescence imaging in mice without craniotomy[7]. They demonstrated an imaging depth exceeding 2 mm, a resolution finer than 10 μm, a 25 mm×20 mm field of view, and a frame rate of 5.3 frames per second. In 2019, Wenbin et al. developed a confocal microscopy system utilizing NIR-II aggregation-induced emission (AIE) dots[8]. They successfully imaged 3D cerebrovascular structures in living mice at a depth of 800 μm, with a spatial resolution of 8.78 μm at 700 μm depth. Around the same time, Liu Y et al. used carbon quantum dots for NIR-II two-photon bioimaging and achieved a maximum penetration depth of 500 μm[9]. In 2021, Wang et al. reported the use of structured-illumination light-sheet microscopy. This method enabled imaging at a penetration depth of 750 μm with a spatial resolution of 1.9 μm in all three dimensions, measured as 1.9 μm×1.9 μm×1.9 μm[10]. A schematic summary in Figure 2-1 quantifies the trade-offs among the four key imaging specifications, which include field of view, imaging speed, depth resolution, and lateral resolution. The analysis highlights the compromises inherent in different illumination strategies, such as wide-field imaging, spot scanning, and light-sheet scanning.

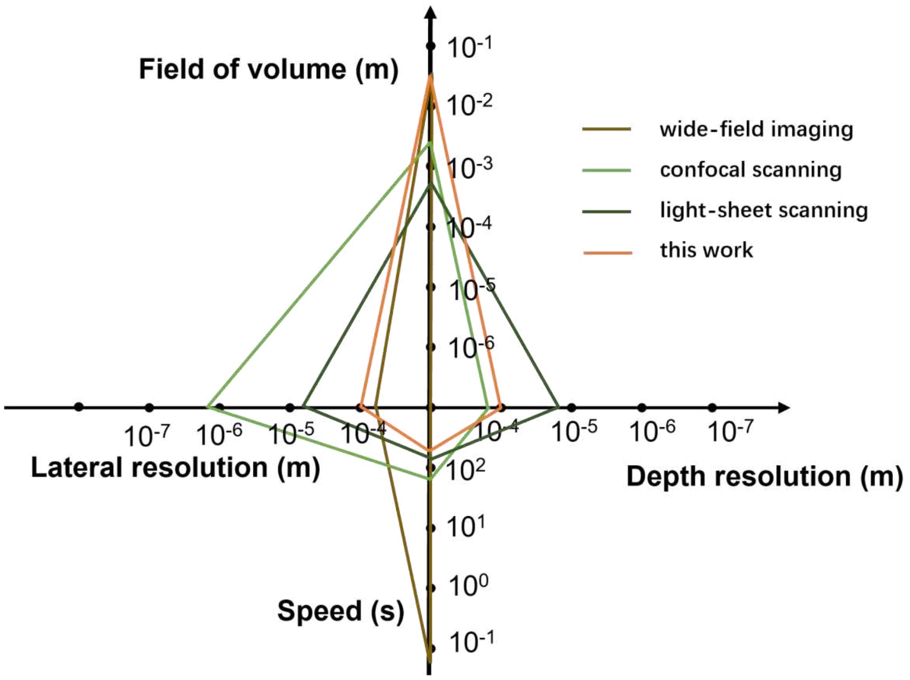

Figure 2-1. Trade-offs among lateral resolution, depth resolution, speed, and volume of view by using the three light illumination strategies, wide-field [11], spot scanning [12], and light-sheet scanning [13], in NIR-II fluorescent volumetric imaging (log scale).

Despite the remarkable advancements in small-animal imaging, several limitations and challenges remain in the field. One significant bottleneck is the trade-off between spatial resolution, imaging depth, and field of view. Techniques like near-infrared fluorescence imaging, while achieving substantial penetration depth, often suffer from reduced spatial resolution and contrast in deeper tissues due to light scattering and absorption. Similarly, existing systems face difficulties in imaging large, complex regions such as whole organs or entire vascular networks without compromising temporal resolution, which is critical for capturing dynamic processes. Another challenge lies in phototoxicity and photobleaching, especially for long-term in vivo imaging, which limits the duration and reliability of observations. Moreover, the development of efficient contrast agents with deep-tissue specificity and minimal toxicity remains an ongoing hurdle. These constraints highlight the need for innovative approaches that can balance resolution, depth, and field of view. Employing large-scale light-sheet microscopy to observe whole mice offers a promising solution by enabling rapid, minimally invasive, and high-resolution imaging across large volumes. This technique provides a unique opportunity to overcome current limitations and unlock new possibilities in studying small-animal models.

2.1.1 Light-sheet Modulation for in Vivo volumetric imaging

Light-sheet microscopy has been widely adopted across various fields, offering mature theories and techniques that provide valuable insights for new applications. In developmental biology, light-sheet microscopy enables long-term imaging of dynamic processes like embryogenesis and organ formation with minimal phototoxicity[14], capturing intricate details over extended periods. In neuroscience, advancements such as lattice light-sheet microscopy allow rapid mapping of neural circuits in whole brains with near-isotropic resolution. Similarly, in cellular biology, light-sheet techniques have revolutionized live-cell imaging, revealing subcellular dynamics and interactions in real-time[15]. These achievements are rooted in innovative approaches like structured illumination, non-diffracting beams, and computational image processing, all of which address challenges such as depth penetration, resolution trade-offs, and background fluorescence. These established methods and ideas provide a robust foundation for adapting light-sheet microscopy to new domains.

Building on the foundational successes of light-sheet microscopy in other fields, this technique offers a promising pathway to overcome existing limitations in small-animal imaging. By leveraging mature technologies like lattice light-sheet illumination, adaptive optics, and advanced computational reconstruction, it becomes possible to address the challenges of imaging resolution, depth, and field of view in large biological specimens such as live mice. Integrating these strategies into a large-scale light-sheet imaging system tailored for small animals would enable real-time, minimally invasive visualization of entire organ systems and vascular networks. This adaptation could bridge the gap between traditional small-animal imaging and the need for high-resolution, dynamic observations in vivo. Through the innovative application of light-sheet microscopy, researchers can unlock new opportunities to study physiological processes, disease progression, and therapeutic interventions in ways previously unattainable in small-animal models.

Herein, this work presents a novel approach to in vivo 3D imaging of small animals by integrating a large-field light-sheet design, dual-region fluorescence probes, and time-gated detection. The study introduces an innovative light-sheet architecture optimized for large fields of view while maintaining high resolution and minimal phototoxicity, enabling detailed observation of deep tissues. Dual-region probes were developed to achieve distinct fluorescence signals for simultaneous imaging of skin and vascular structures, while time-gated detection effectively reduced background noise, improving imaging contrast. This work also combines deep-learning algorithms to extract vascular structures from fluorescence data, providing an automated and precise method for analyzing complex networks. Scientifically, the study revealed the relative depth relationships between skin and blood vessels in small animals, advancing our understanding of in vivo tissue interactions. From an engineering perspective, it represents a breakthrough in achieving dynamic, high-resolution imaging of deep tissues, offering a robust platform for preclinical research and translational applications.

2.1.2 Time-gated Modulation for in Vivo volumetric imaging

Time-modulated optical field detection has become a powerful tool in fluorescence microscopy and deep-tissue imaging, providing significant advantages in suppressing background noise and enhancing signal contrast. By implementing time-gated detection, fluorescence signals can be selectively captured within a defined temporal window, ensuring that only emission occurring after laser excitation is recorded while eliminating unwanted scattered laser light and autofluorescence[16, 17]. This method improves the SNR and allows for deeper tissue penetration, making it especially valuable in biomedical imaging and functional fluorescence studies. High-speed optical choppers and electronic gating techniques further refine the synchronization between excitation and detection, ensuring precise optical modulation and higher temporal resolution.

When applied to small-animal volumetric imaging, time-gated detection provides several key benefits. In whole-organism imaging, light scattering presents a major challenge, reducing contrast and resolution. In 2019, Gu et al. developed a new contrast agent based on Yb^{3+}-doped nanoparticles. These nanoparticles exhibit a near-unity quantum yield and a sufficiently long lifetime in the NIR range, making them suitable for time-gated imaging. This approach enabled a high signal-to-noise ratio greater than 9 under an excitation power density of 1.1 mW/cm^2[18]. In 2020, B. Nimmegeers et al. synthesized NIR-emitting nanoparticles specifically designed for time-gated imaging. This method effectively eliminated autofluorescence from biological tissues[19]. To implement time gating in the visible range, researchers can use a modulated camera or a switchable single-element detector. However, in the NIR-II range, a time-gated camera must be custom-built, which significantly increases costs. As an alternative, a chopper can be used to modulate the light path, providing a more cost-effective and practical solution[20-22].

By utilizing precisely controlled time windows, this technique ensures that deep-tissue fluorescence signals are captured while rejecting short-lived background noise. Additionally, in multi-region imaging, such as differentiating tissue structures within small animals, time-gated detection enables better depth discrimination, enhancing the visualization of features like vasculature, tumors, and metabolic processes. The ability to completely filter out scattered excitation light further improves contrast, making it an ideal approach for high-resolution, label-free imaging in living organisms.

2.2 Principle and System

2.2.1 Large-Field Light-Sheet Time-gated Imaging

To achieve large-field 3D imaging of small animals, the study employs an optimized light-sheet design capable of covering expansive sample regions while maintaining fine resolution. The light sheet, generated through a precisely tuned optical system, balances thickness and uniformity to minimize phototoxicity and scattering effects. Additionally, the dual-region fluorescence probes are tailored to simultaneously emit distinct signals from two regions, both skin and vasculature, allowing for differential imaging. This dual-region approach ensures precise delineation of tissue boundaries and relative depths within the imaging field, enabling comprehensive visualization of skin and blood vessels in a single scan. The light-sheet architecture is further enhanced to adapt to the optical properties of small animal tissues, ensuring consistent signal intensity and high contrast across various depths.

To generate a light sheet, we position the focal spot at a specific distance from the back focal plane of the objective lens, forming an optical system with a low numerical aperture (NA). The focal spot is adjusted using a 10× objective lens with an NA of 0.3 (Nexscope PlanF-Apo). To shape the Gaussian beam into a light sheet, we employ a Powell lens array (PMMA-Powell lens array-30). Compared to a cylindrical lens, the Powell lens array provides more uniform illumination across the sheet. The full width at half maximum (FWHM) of the light sheet can be determined using the following equation:

$$2\omega_0 = 2\frac{n\lambda}{\pi NA} \tag{2-1}$$

Where λ is the wavelength, n is the refractive index. Using the Gaussian beam model, we get the diameter and length of the beam waist, the Gaussian beam functions are shown as:

$$\begin{gathered} E = E_0\frac{\omega_0}{\omega(z)}\exp\left(-\frac{r^2}{\omega^2(z)}\right), \\ \omega(z) = \sqrt{2}\omega_0, \\ z_0 = \frac{\omega^2\pi\eta}{\lambda}, \end{gathered} \tag{2-2}$$

Here, E is the amplitude of the light beam, E_0 is the amplitude at the focal plane, z is the distance from the focal plane, r is the distance from the optical axis, $\omega(z)$ is the spot radius, ω_0 represents the minimum radius of the beam at z_0, known as the beam waist, is the spot radius at the focal plane. z_0 is the Rayleigh length, η is the refractive index of the medium, λ is the wavelength. The Rayleigh range is the range when the spot area becomes twice the minimum value, and the Rayleigh length of a Gaussian beam is the length from the waist to the spot of the Rayleigh range.

The surface of the mice is not a flat plane, requiring a sufficient Rayleigh length for effective light-sheet scanning. To ensure adequate illumination, we set the Rayleigh length to 8 mm, which resulted in a simulated focal spot radius of approximately 100 μm in diameter. In our experiment, we achieved a focal spot diameter of 100.5 μm when the Rayleigh length was around 8 mm, as illustrated in Figure 2-2. For deeper illumination, extending the Rayleigh length to 26 mm allows adjustment of the light-sheet thickness to 183.1 μm by modifying the distance between the lens system and the objective. The comparison between wide-field imaging and light-sheet imaging (maximum projection) is presented in Figure 2-2(c, d). The results demonstrate that light-sheet imaging produces a lower background intensity. Compared to wide-field illumination, light-sheet imaging provides a higher contrast ratio due to reduced scattering. In light-sheet mode, scattering primarily occurs within the illuminated sheet area. In contrast, wide-field illumination generates extensive scattered light from the surrounding regions, leading to a higher background intensity.

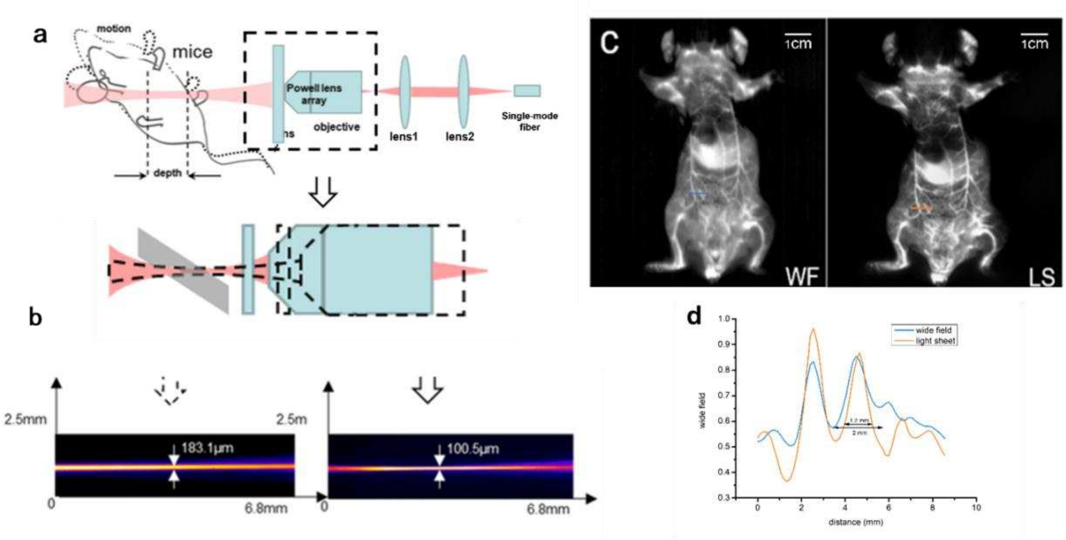

Figure 2-2. Adjustable large-FoV light sheet illumination system for high-contrast whole mice imaging. *a) light sheet illumination system with adjustable thickness from 183.1 to 100.5 μm and Rayleigh length from 8 to 26 mm, formed by a 30 mm focus lens (Thorlab-1700-B), a 16 mm focus 0.79 NA aspherical lens (Thorlab-ACL254U-B), and a 10× 0.3 NA objective lens. b) the illumination of light sheet through the whole mice. c) Comparison of a wide-field imaging result and a top view of light-sheet scanning result at a distance of 100 μm from the mice, d) line profile analysis of c).*

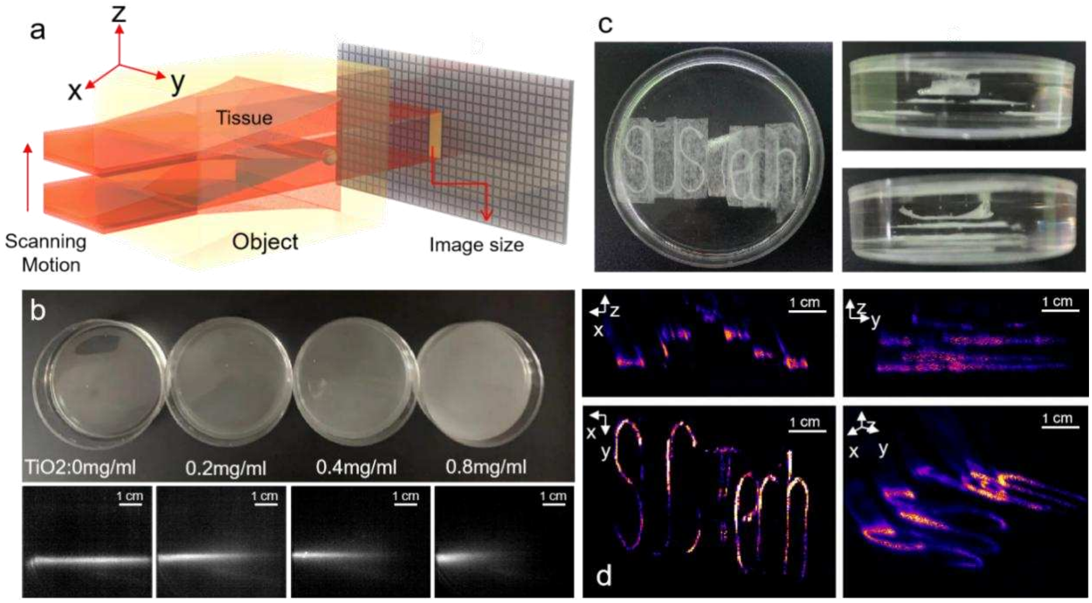

Figure 2-3. Phantom experiment to evaluate the scattering effect under the large-FoV light-sheet illumination. *a) Schematic illustration of light-sheet scanning across the phantom matrix. b) Scattering simulation using silicone phantom containing lanthanide doped NIR-II fluorescent nanoparticles and TiO2 nanoparticles. c) Letter patterns stained by lanthanide-doped NIR-II fluorescent nanoparticles and embedded in silicone phantom d) Reconstruction of the letter patterns by light-sheet scanning. The diameter of the container is 5.5 cm. The step of light-sheet scanning between each layer is 1 mm.*

2.2.2 Time-Modulated Optical Field Detection for Background Suppression

In this study, I developed and integrated time-gated optical field modulation to enhance fluorescence imaging in small animals. A high-speed optical chopper was employed to precisely synchronize the excitation and detection phases, ensuring that only post-excitation fluorescence was recorded. Additionally, advanced timing electronics allowed for accurate temporal gating, improving both depth resolution and contrast in live tissue imaging. This approach significantly enhanced deep-tissue imaging quality, enabling clear differentiation of tissue structures such as skin and vasculature. Figure 2-3 and Figure 2-4 demonstrate the effectiveness of our method, showing substantial improvements in imaging depth and contrast, validating the potential of time-gated technology for high-resolution, in vivo fluorescence imaging.

Our experimental setup utilizes a time-gated fluorescence imaging system combined with a light-sheet generator to enhance deep-tissue imaging contrast. The system consists of a high-speed optical chopper synchronized with a pulsed laser signal to precisely control the detection window. As shown in the schematic on the left, the chopper modulates the excitation light, allowing only fluorescence signals within a specific time window to be captured by the camera. A pinhole further refines the collected signals by blocking unwanted scattered light. The system operates with precise synchronization between the chopper, laser excitation, and camera acquisition, ensuring optimal background suppression while maintaining signal integrity.

The comparison results, displayed on the right, illustrate the enhanced imaging contrast achieved through time-gated detection. Each row presents fluorescence images taken under continuous-wave (CW) illumination (left column) vs. time-gated (TG) imaging (right column) at different power levels. The time-gated approach significantly reduces laser scattering background, leading to improved visibility of tissue structures at various depths. Notably, under the same average laser power, time-gated imaging demonstrates higher contrast and improved depth-dependent differentiation, effectively filtering out scattered excitation light while preserving fluorescence signals.

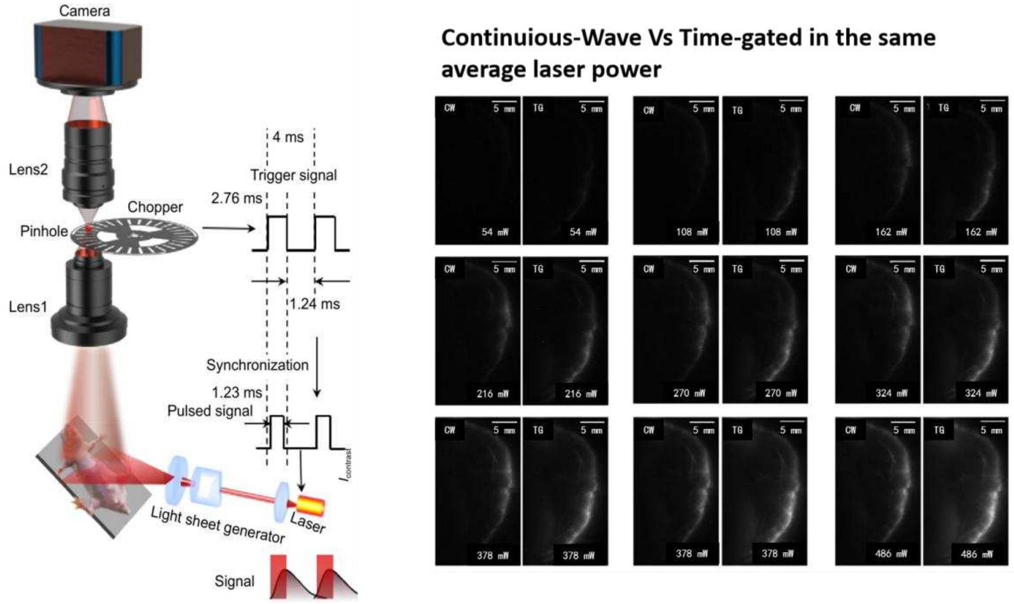

Figure 2-4. Time-gated light-sheet imaging system[23]. *a) Time-gated imaging system to improve the SNR. b) Comparison results of time-gated imaging and continuous wave filter-based imaging. The plotted pictures represent the profiles of the white dotted lines.*

By leveraging precise optical gating, our system achieves superior fluorescence signal detection while suppressing background interference. This technique is particularly beneficial for deep-tissue imaging, small-animal volumetric imaging, and fluorescence lifetime measurements. The enhanced SNR allows for clearer visualization of biological structures, making it a valuable tool for high-resolution in vivo imaging.

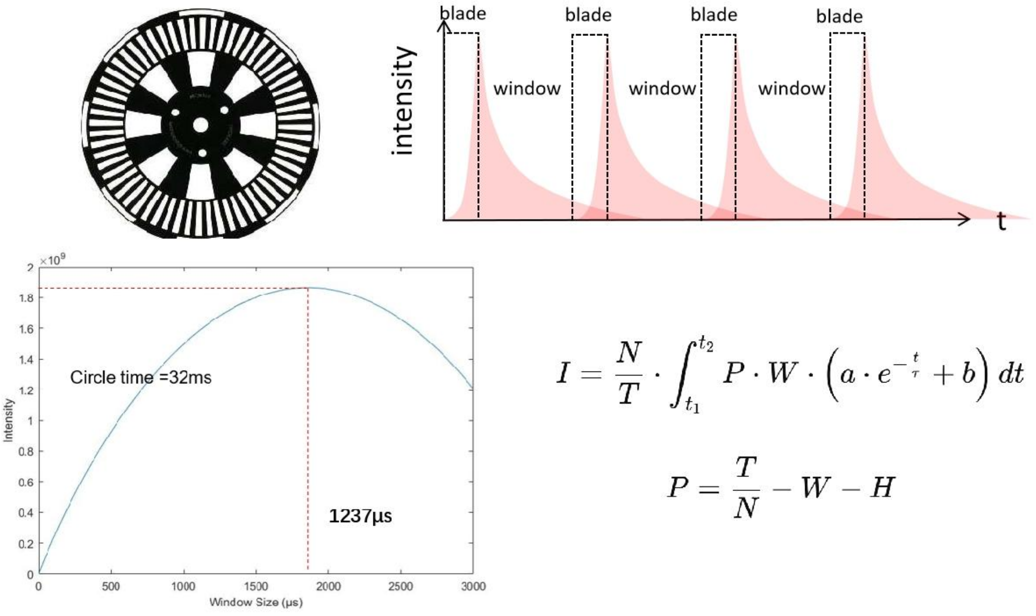

$$I = \frac{N}{T} \cdot \int_{t_1}^{t_2} P \cdot W \cdot \left(a \cdot e^{-\frac{t}{\tau}} + b\right) dt$$

$$P = \frac{T}{N} - W - H$$

Figure 2-5. Variation of luminous flux with chopper parameters. *a) The luminous flux changes with the window width, at a cycle time of 32 ms. b) Variation of maximum luminous flux at increasing cycle time.*

To optimize fluorescence signal collection, I performed theoretical calculations of the integrated fluorescence intensity over time, considering the decay characteristics of the emitted light. By modeling the fluorescence decay and integrating the intensity over each open window of a rotating chopper blade, I determined that the optimal duty cycle is 1:2 (open:closed). This ensures maximum signal collection while minimizing background noise.

To achieve this optimal duty cycle, I designed a chopper blade with alternating open and closed sections, ensuring that the fluorescence excitation and emission are sampled efficiently. The mathematical formulation of the integrated intensity I considers the fluorescence decay function and the chopper window timing, leading to the optimal selection of window size (1237 µs) and cycle time (32 ms). The equations provided describe the integration of intensity over the time windows, as well as the effective pulse duration P, which accounts for the chopper's rotation period, number of blades, and window-to-blade ratio.

This optimized chopper design is crucial for applications requiring time-gated detection, such as fluorescence lifetime imaging (FLIM) and time-resolved spectroscopy, where precise control over excitation and collection timing enhances contrast and measurement accuracy.

2.2.3 Deep Learning for Vascular Extraction and Depth Analysis

In above study, I successfully eliminated background laser scattering using large-scale light-sheet imaging and time-gated detection. However, some residual background fluorescence remains due to scattered laser excitation, affecting image clarity. To achieve a more precise 3D reconstruction of the vascular structure in mice, advanced image processing algorithms are necessary. Unlike simple noise, this background interference cannot be effectively removed using conventional denoising techniques. A conventional method to enhance the vessel structure is to calculate the partial derivative of the image by Hessian matrix[24]. However, when the vessels are presented against a complex background, the resolving power of Hessian matrix based method is limited. Therefore, I developed a vascular recognition algorithm[23], as outlined in the ***Figure 2-6***, to selectively enhance vessel structures while suppressing background signals.

The schematic diagram of the vascular enhancement algorithm is shown in the Figure 2-6. I use a sliding window to scan each pixel of the image point by point to determine whether it belongs to the vascular contour. First, the sliding window is adjusted by subtracting the background. A sloped background is one of the key factors affecting the vascular enhancement algorithm. Since the selected sliding window is relatively small, the background can be approximated as a flat slope. The background image is estimated by selecting the minimum values from the four corner regions and performing interpolation. After background subtraction, the vascular contour is identified by analyzing four directional edges, allowing for further image segmentation and enhancement.

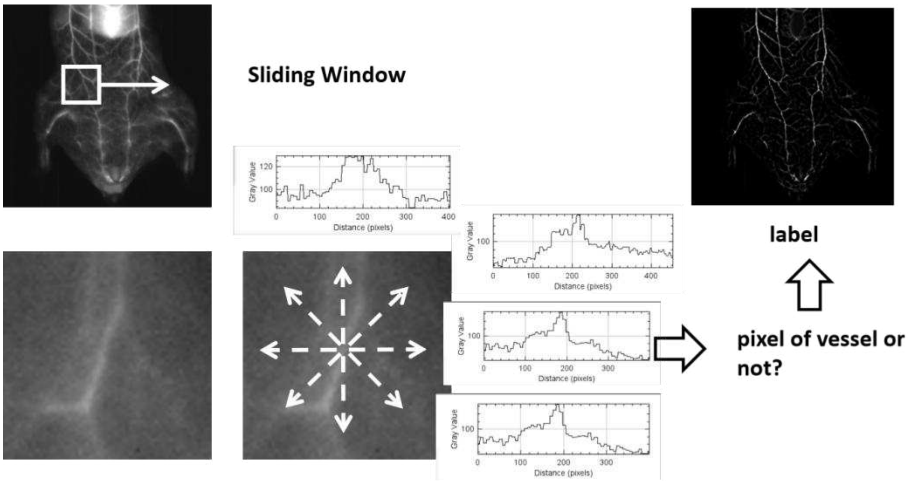

Figure 2-6. Algorithm Principle for Enhancing Mouse Vascular Images.

Given the complexity and computational demands of our algorithm, I further integrated deep-learning networks to accelerate the processing. Specifically, I employed convolutional neural networks (CNNs) trained for vascular segmentation and reconstruction. This system automates vascular feature extraction from fluorescence images, accurately differentiating blood vessels from surrounding tissues. Moreover, it enables quantitative analysis of vessel depths and spatial relationships. The deep-learning framework significantly improves processing speed, reducing manual intervention and making it a highly efficient tool for large-scale in vivo imaging studies. Figure 2-7 and Figure 2-8 illustrates the effectiveness of our approach, showcasing detailed 3D reconstructions of vascular networks, highlighting their relative positioning within tissues.

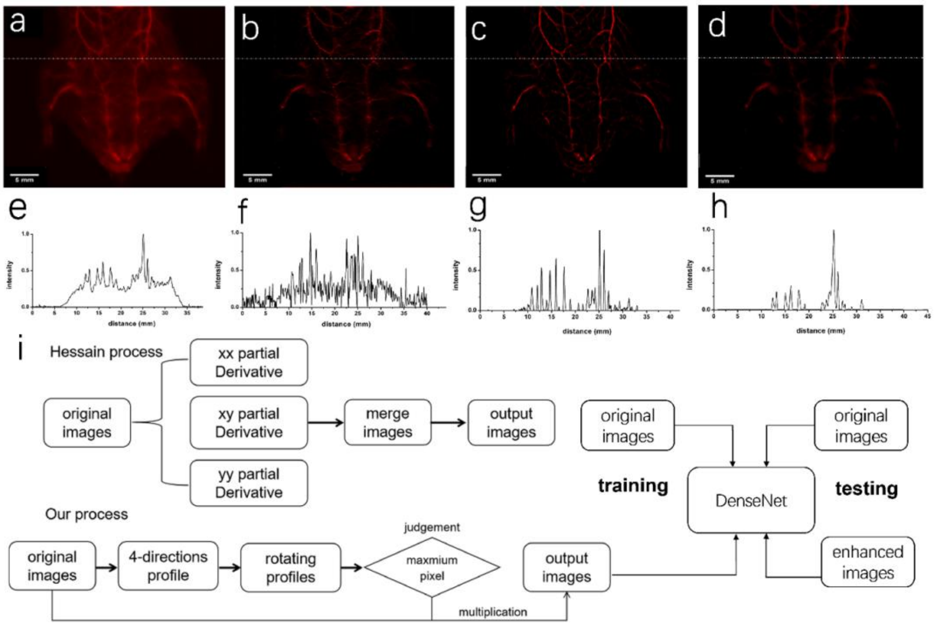

Figure 2-7. Comparison schematics and results of vessel enhancement processes by using Hessian matrix v.s. DenseNet deep learning algorithm based on protuberance detection[23]. *a) Raw image. b) Hessian matrix enhancement. c) DenseNet enhancement result. d) Image with contrast enhancement. e),*

f),g),h) are the profiles of white dotted lines in a), b), c), d). i) Training process of Hessian algorithm and our algorithm.

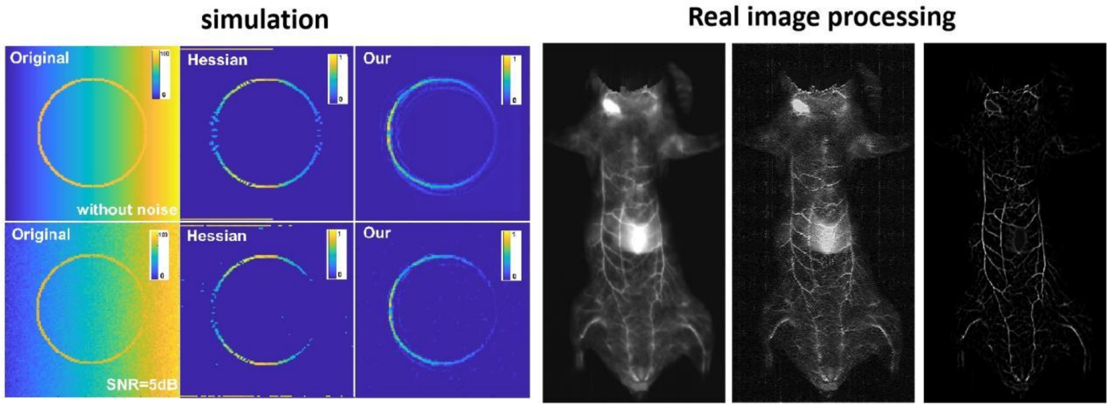

Figure 2-8. Comparison of my results with the image enhancement effect of the Hessian algorithm in simulated structural images and real image processing.

The results demonstrate the robustness of our method in both simulation and real imaging scenarios. In simulations, I introduced background slopes and noise to test algorithm performance under challenging conditions. While traditional algorithms struggle with interference, our approach successfully extracts and reconstructs vascular structures with high fidelity. Similarly, in real imaging, our algorithm outperforms conventional Hessian-based methods, providing clearer and more accurate vessel segmentation. The ability to handle low SNR and complex tissue environments underscores the effectiveness of our approach in biological imaging applications.

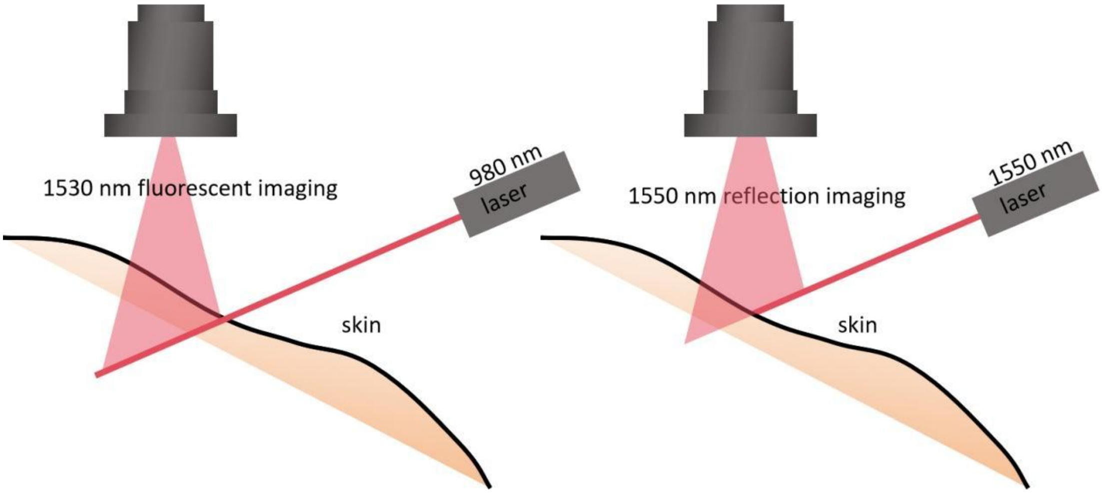

Figure 2-9. A schematic diagram of light-sheet illumination capturing the vascular and skin surface contours of a mouse.

To determine the relative depth of the epidermis and blood vessels, I employ a dual-modality imaging approach combining fluorescence imaging at 1530 nm and reflection imaging at 1550 nm. In the fluorescence imaging setup (left panel), a 980 nm laser excites deeper tissue structures, such as blood vessels, which emit fluorescence at 1530 nm. Since hemoglobin and other vascular components preferentially absorb and emit in this spectral range, this method enables high-contrast visualization of subcutaneous vasculature. On the other hand, the reflection imaging setup (right panel) utilizes a 1550 nm laser for surface tissue illumination, where backscattered light is detected to reconstruct the epidermal contour, providing an accurate reference for the skin surface.

By combining these two imaging modalities, I can quantify the depth difference between the skin surface and underlying blood vessels. The fluorescence signal primarily originates from deeper layers, representing vascular structures, while the reflection signal maps the superficial skin profile. By analyzing the spatial correlation between these two signals, I obtain a precise depth distribution of subcutaneous vasculature relative to the epidermis. This non-invasive technique is highly valuable for applications such as vascular imaging, dermatological diagnostics, and blood perfusion analysis, providing critical insights into tissue-depth interactions in biomedical research and clinical settings.

2.3 Result

The experimental results presented in this study robustly validate the accuracy and effectiveness of the proposed methods and theoretical framework. The large-field light-sheet design demonstrated its capability to achieve high-resolution imaging across an expansive field of view, as shown by the clear visualization of skin and vasculature structures with minimal phototoxicity. The dual-region fluorescence probes enabled precise differentiation between skin and vascular tissues, with their distinct emission profiles confirming the probe's reliability for simultaneous multi-region imaging.

The time-gated detection system further proved its efficacy by significantly enhancing SNR, particularly in deeper tissue layers where autofluorescence and scattering typically degrade image quality. Comparative results revealed a marked improvement in fluorescence contrast, with clear boundaries between tissue structures, validating the system's ability to isolate long-lived fluorescence signals effectively.

The integration of deep-learning algorithms for vascular structure extraction yielded highly accurate 3D reconstructions of blood vessels, corroborating the system’s ability to process complex imaging data efficiently. These reconstructions, which quantified the relative depths of skin and vasculature, matched theoretical predictions, providing further evidence for the robustness of the methodology. Together, these experimental findings underscore the system's potential to transform in vivo imaging, offering a reliable, scalable solution for high-resolution and high-contrast imaging in small-animal models.

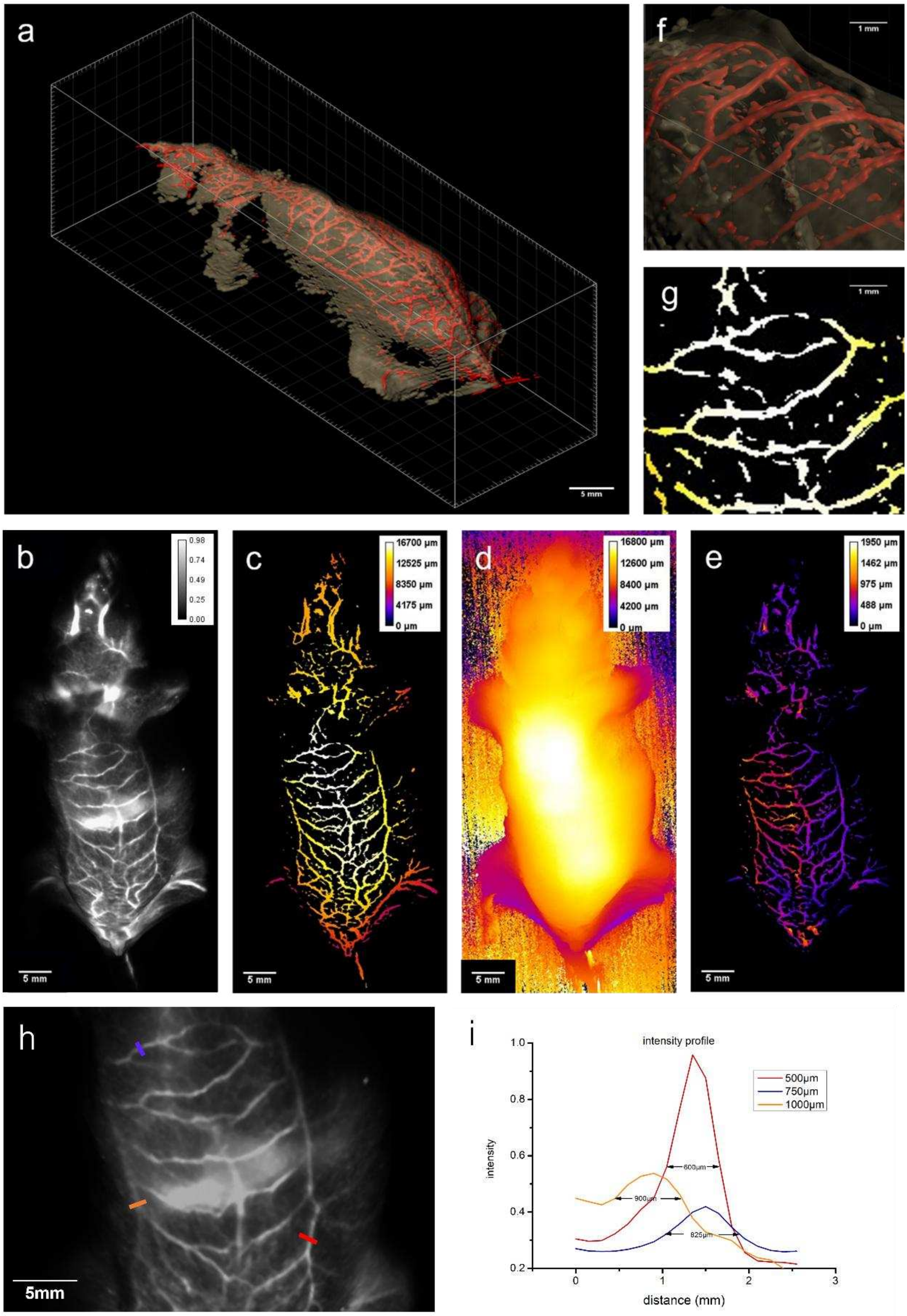

Figure 2-10. The depth information of the high contrast images of the whole mice skin and blood vessel revealed by the time-gated light-sheet NIR-II volumetric imaging system enhanced by deep learning algorithm. *a) The 3D reconstruction image of mice skin and vessel networks. b) Luminescent intensity map. c) The height map of the mice's blood vessels. d) The height map of the mice's skin. e)*

Vessels with colors that represent their depth under the skin. f), g) local details of the same position in a) and c). h,i) intensity profiles of vessels in different depths. h) A magnified part of b). Intensity profiles of lines in h) with depths of 500 μm, 750 μm, and 1000 μm.

The experimental results presented in this study, as illustrated in ***Figure 2-10***, validate the accuracy and effectiveness of the proposed methods and theoretical framework. By employing the large-field light-sheet design and dual-region probes, the system achieved clear differentiation between skin and vascular structures, demonstrating its ability to provide high-contrast, in vivo imaging with minimal phototoxicity. The time-gated detection further enhanced signal clarity by effectively suppressing background autofluorescence, as evidenced by the significantly improved SNR and depth-resolved imaging.

The missing vessels are likely due to brightness limitations. Thin vessels may produce weaker signals that fall below the sensitivity of our camera. Additionally, some vessels may be located in deeper tissue layers and are therefore not visible. Our algorithm performs image enhancement based solely on the acquired images, so it cannot generate vessels that are not captured in the original data.

The relative depth measurements of the skin and blood vessels, derived from the fluorescence signals, were consistent with known anatomical structures in small animals, confirming the precision of the dual-mode design and the optical setup. Additionally, the deep-learning-based vascular segmentation algorithm accurately reconstructed the 3D vascular network, as verified by comparisons with ground truth data and manual annotations. The extracted vascular depths matched the expected spatial relationships, reinforcing the reliability of the system in analyzing complex tissue interactions.

Collectively, the experimental results demonstrate the robustness and practicality of the proposed methods. The system's ability to achieve high-resolution imaging across large volumes, accurately map tissue depths, and extract fine vascular details confirms the theoretical foundation and engineering design, paving the way for advanced applications in small-animal imaging and translational research.

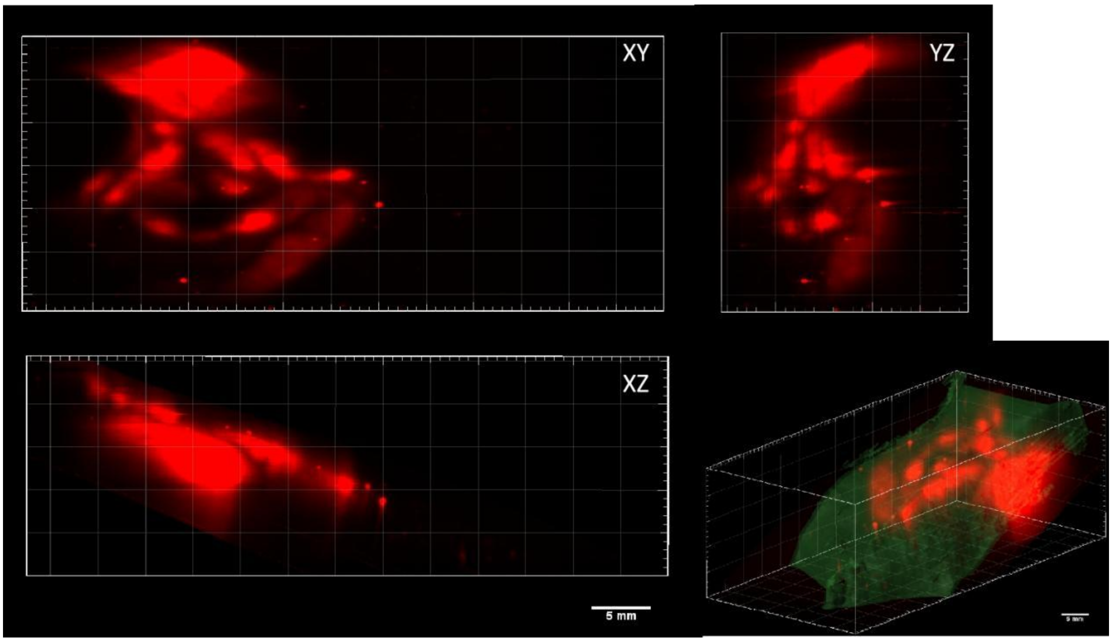

Figure 2-11. Light-sheet scanning imaging of the mouse stomach and intestines.

One limitation in visualizing deep vascular structures is that fluorescence signals are partially absorbed by surrounding tissues, reducing the detectable depth. Since imaging relies on emitted fluorescence, brighter targets with stronger fluorescence signals are more easily observed compared to weaker vascular emissions. To explore deeper anatomical structures, I leveraged this property by performing oral administration in mice, allowing fluorescent contrast agents to reach the gastrointestinal tract. As shown in Figure 2-11, I successfully visualized deeper intestinal and stomach structures, which exhibit stronger fluorescence intensity, demonstrating the potential of this method for deep-tissue imaging beyond vascular structures.

2.4 Conclusion

This study presents a novel approach for large-scale, high-resolution 3D imaging of small animals, offering transformative potential in preclinical research and translational applications. The system's innovative combination of a large-field light-sheet design, dual-region fluorescence probes, time-gated detection, and deep-learning-based vascular analysis enables detailed visualization of complex tissue structures with minimal phototoxicity. Such capabilities make it a valuable tool for studying dynamic physiological processes, vascular development, disease progression, and the effects of therapeutic interventions in vivo.

Advantages: The proposed system achieves an excellent balance between field of view, spatial resolution, and imaging depth, addressing key challenges in small-animal imaging. The dual-region probes provide clear differentiation between skin and vascular structures, while the time-gated detection minimizes background noise, enhancing SNR even at greater depths. The integration of deep learning further streamlines data analysis, enabling precise 3D reconstructions and quantitative insights with minimal manual intervention.

Limitations: However, certain limitations persist. The system relies on advanced optical components and precise calibration, which may increase its complexity and cost. Additionally, while the dual-region probes effectively differentiate skin and vasculature, their specificity may need further refinement for broader tissue types. Lastly, the reliance on deep-learning algorithms requires high-quality training data and computational resources, which could pose a barrier for widespread adoption.

This work not only advances the field of small-animal imaging but also sets the stage for future innovations. The system's unique ability to provide accurate in vivo imaging of skin and vascular structures has significant implications for studying diseases such as cancer, cardiovascular conditions, and inflammatory disorders. Moving forward, further optimization of probe design and imaging protocols could expand its applicability to additional tissue types and biological processes.

The presented system represents a breakthrough in overcoming the inherent trade-offs in resolution, depth, and field of view in small-animal imaging. By bridging these gaps, it provides researchers with an unprecedented ability to study dynamic biological processes in vivo with high precision and detail. This approach lays the groundwork for future advancements in optical imaging systems and paves the way for novel diagnostic and therapeutic strategies. Through continued refinement and adoption, this system has the potential to transform our understanding of complex biological phenomena and accelerate the translation of preclinical findings into clinical solutions.

2.5 Reference

1. Ntziachristos, V., C. Bremer, and R. Weissleder, *Fluorescence imaging with near-infrared light: new technological advances that enable in vivo molecular imaging.* European radiology, 2003. **13**(1): p. 195-208.
2. Li, B., et al., *Organic NIR-II molecule with long blood half-life for in vivo dynamic vascular imaging.* Nature communications, 2020. **11**(1): p. 3102.
3. Zhu, X., et al., *High-fidelity NIR-II multiplexed lifetime bioimaging with bright double interfaced lanthanide nanoparticles.* Angewandte Chemie, 2021. **133**(44): p. 23737-23743.
4. Du, H., H. Wan, and H. Dai, *Recent advances in development of NIR-II fluorescent agents.* Near Infrared-Emitting Nanoparticles for Biomedical Applications, 2020: p. 83-101.
5. Welsher, K., S.P. Sherlock, and H. Dai, *Deep-tissue anatomical imaging of mice using carbon nanotube fluorophores in the second near-infrared window.* Proceedings of the National Academy of Sciences, 2011. **108**(22): p. 8943-8948.
6. Hong, G., et al., *Multifunctional in vivo vascular imaging using near-infrared II fluorescence.* Nature medicine, 2012. **18**(12): p. 1841-1846.
7. Hong, G., et al., *Through-skull fluorescence imaging of the brain in a new near-infrared window.* Nature photonics, 2014. **8**(9): p. 723-730.
8. Yu, W., et al., *NIR-II fluorescence in vivo confocal microscopy with aggregation-induced emission dots.* Science Bulletin, 2019. **64**(6): p. 410-416.

9. Liu, Y., et al., *Rational synthesis of highly efficient ultra-narrow red-emitting carbon quantum dots for NIR-II two-photon bioimaging.* Nanoscale, 2020. **12**(3): p. 1589-1601.
10. Wang, F., et al., *In vivo NIR-II structured-illumination light-sheet microscopy.* Proceedings of the National Academy of Sciences, 2021. **118**(6): p. e2023888118.
11. Lu, L., et al., *NIR-II bioluminescence for in vivo high contrast imaging and in situ ATP-mediated metastases tracing.* Nature communications, 2020. **11**(1): p. 4192.
12. Liao, J., et al., *Depth-resolved NIR-II fluorescence mesoscope.* Biomedical Optics Express, 2020. **11**(5): p. 2366-2372.
13. Wang, F., et al., *Light-sheet microscopy in the near-infrared II window.* Nature methods, 2019. **16**(6): p. 545-552.
14. Pampaloni, F., et al. *Light sheet-based fluorescence microscopy (LSFM) reduces phototoxic effects and provides new means for the modern life sciences*. in *European Conference on Biomedical Optics*. 2011. Optica Publishing Group.
15. Girkin, J.M. and M.T. Carvalho, *The light-sheet microscopy revolution.* Journal of Optics, 2018. **20**(5): p. 053002.
16. Jin, D. and J.A. Piper, *Time-gated luminescence microscopy allowing direct visual inspection of lanthanide-stained microorganisms in background-free condition.* Analytical chemistry, 2011. **83**(6): p. 2294-2300.
17. Zheng, X., et al., *High-contrast visualization of upconversion luminescence in mice using time-gating approach.* Analytical chemistry, 2016. **88**(7): p. 3449-3454.
18. Gu, Y., et al., *High-sensitivity imaging of time-domain near-infrared light transducer.* Nature Photonics, 2019. **13**(8): p. 525-531.
19. Nimmegeers, B., et al., *Synthesis and characterization of GdVO4: Nd near-infrared phosphors for optical time-gated in vivo imaging.* Materials, 2020. **13**(16): p. 3564.
20. Marriott, G., et al., *Time resolved imaging microscopy. Phosphorescence and delayed fluorescence imaging.* Biophysical journal, 1991. **60**(6): p. 1374-1387.
21. Cheng, S., et al., *Time-gated ratiometric detection with the same working wavelength to minimize the interferences from photon attenuation for accurate in vivo detection.* ACS Central Science, 2019. **5**(2): p. 299-307.
22. Dong, Z., et al., *A modulated sparse random matrix for high-resolution and high-speed 3D compressive imaging through a multimode fiber.* Science bulletin, 2022. **67**(12): p. 1224-1228.
23. Wu, S., et al., *Deep learning enhanced NIR-II volumetric imaging of whole mice vasculature.* Opto-Electronic Advances, 2023.
24. Yin, X., et al., *Accurate image analysis of the retina using hessian matrix and binarisation of thresholded entropy with application of texture mapping.* PloS one, 2014. **9**(4): p. e95943.

3 Rotational Light-Sheet modulation for Scattering Imaging

3.1 Introduction

Label-free imaging is becoming an increasingly important tool in modern microscopy, serving as a valuable complement to fluorescence imaging. Unlike fluorescence-based methods, it does not require labels or stains, allowing samples to be observed in their native state while minimizing phototoxicity. Label-free imaging mainly includes several categories: phase-delay-based imaging techniques such as Optical Diffraction Tomography (ODT)[1, 2] and quantitative phase imaging; scattering-based techniques such as Rotational Scattering Imaging (ROCS)[3-7]; nonlinear optical methods such as Raman spectroscopy imaging and second harmonic generation (SHG)[8] imaging; as well as photoacoustic imaging and autofluorescence imaging.

Among the various label-free techniques, ROCS stands out for its rapid acquisition speed, high contrast, and super resolution which achieved without computational reconstruction. By selectively enhancing scattered light through rotational illumination or sample modulation, ROCS effectively isolates dynamic or modulated signals from background noise. This makes it particularly well-suited for real-time, super-resolution imaging of small scattering samples, such as living cells and tissues. With its ultra-fast, label-free, and reconstruction-free approach, ROCS represents a significant advancement in scattering-based imaging. This method is well-suited for real-time observation of dynamic processes in subcellular structures.

Despite the significant advantages of Rotational Scattering Imaging (ROCS), its reliance on Total Internal Reflection Fluorescence (TIRF)[9] illumination comes with inherent limitations. TIRF restricts the excitation region to an evanescent field within a few hundred nanometers of the sample surface, effectively making ROCS a two-dimensional technique. As a result, structures or events occurring in deeper layers of a cell or tissue remain inaccessible, limiting its applicability in comprehensive biological studies.

Additionally, the strong reflection of the laser at steep incidence angles can overpower the desired scattering signals, necessitating the use of an adjustable aperture or iris in the detection path. While this aperture helps block excessive reflection by reducing the numerical aperture (NA), it also narrows the field of view and can limit resolution. Thus, while TIRF-based illumination greatly enhances contrast for near-surface structures, its inherent 2D nature and the technical challenges posed by laser reflections restrict ROCS's potential for broader volumetric imaging.

Light-sheet microscopy is a well-established technique for modulating light fields, offering high tomographic capabilities through its orthogonal illumination geometry. By delivering light at a 90-degree angle relative to the detection axis, it effectively suppresses direct laser reflections, reducing background interference and maintaining a high signal-to-noise ratio (SNR). While primarily associated with fluorescence imaging, this orthogonal illumination approach is also highly effective for scattering-based imaging, as it confines both the illumination and detection planes, preventing unwanted reflections from contaminating the desired signals.

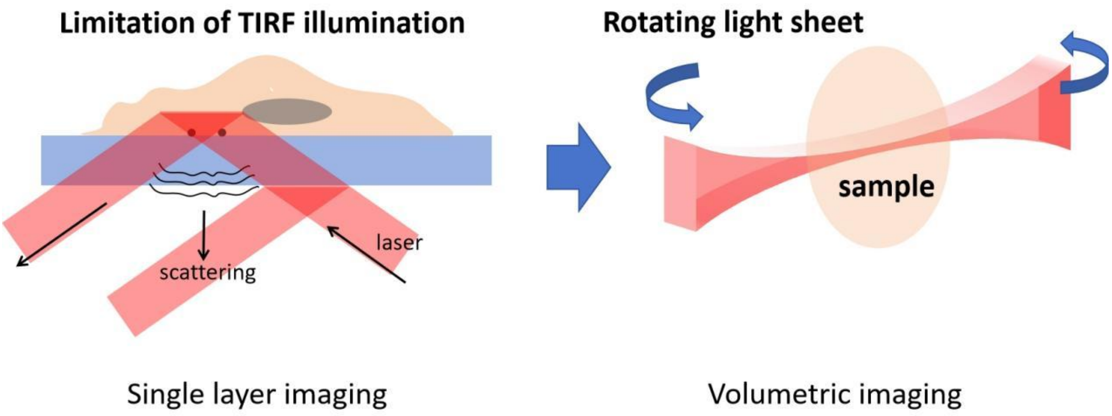

Figure 3-1.Concept to replace TIRF illumination in ROCS using light-sheet modulation

Building on these advances, my goal is to replace the rotating TIRF illumination in ROCS with a rotating light sheet, thereby extending label-free scattering imaging into three dimensions. The light-sheet orthogonal illumination method was originally developed to observe the super-resolution scattering images of nanoparticles[10]. After the development of fluorescence labeling techniques, light-sheet illumination was primarily utilized for fluorescence imaging. However, in recent years, a new approach called scattering light-sheet microscopy (sLSM) has also been studied. In 2020, Christopher et al. used sLSM for cellular-level imaging of tissues[11]. In 2022, Xiangda et al. applied sLSM to investigate long-term interactions between cells and the extracellular matrix[12]. That same year, Jingwei compared the performance of sLSM under different wavelengths[13]. In 2023, Nava et al. explored the potential of sLSM for subcellular-level imaging[14].

By rotating an orthogonally oriented light sheet rather than a spinning TIRF beam, I eliminate most reflections that would otherwise obscure weak scattered signals, preserving the high-contrast advantage of ROCS while gaining true volumetric access to the sample. Such a ‘rotational light-sheet’ strategy would allow dynamic scattering information to be captured across multiple planes with minimal background interference, granting a more complete picture of cellular or tissue-scale structures. Moreover, integrating ROCS principles, especially its rapid imaging capabilities and sub-diffraction contrast, into a tomographic light-sheet framework opens the door to fast, label-free 3D visualization of living systems, overcoming the inherent 2D limitations of TIRF-based setups.

3.2 System and Result

The concept of rotational light-sheet illumination is simple, but its optical system design poses great challenges. The challenges mainly lie in two aspects. First, unlike rotational TIRF illumination, aligning the light sheet in free space is difficult. Second, the thickness of the light sheet must not be too large; otherwise, scattered light from different layers will interfere with each other. This requires a high

NA illumination. However, using a high NA means a shorter illumination distance, leading to spatial constraints. Considering these limitations, we implemented two different designs as follows.

3.2.1 Multi-angle light-sheet illumination

My first design involved using six lasers to generate six light sheets that illuminate the center from different directions. The original ROCS imaging method is implemented by spinning TIRF illumination. The spinning TIRF illumination is generated by galvo-lens and single laser. Therefore, although the illumination source at each moment originates from the same laser, it can be considered as different light sources that are mutually incoherent. The intensity integration of the ROCS imaging method over one full rotation can be expressed as[3]:

$$P_{ROCS}(x,y) = \int_0^{2\pi} |E_{cam}(x,y,\phi)|^2 d\phi \tag{3-1}$$

Here, $E_{cam}(x,y,\phi)$ represents the electric field distribution on the imaging plane. ϕ is the illumination angle. However, at a single moment, the illumination light is coherent. Under a single illumination direction, the intensity distribution on the image plane can be expressed as[4]:

$$\begin{aligned} P_{\phi_0}(x,y,\varepsilon) &= \int |E_{cam}(x,y,\phi_0,\varepsilon)|^2 d\varepsilon \\ &= \int \left|E_i[(e^{-ik_i(\phi_0,\varepsilon)r}) \cdot f(x,y)] * PSF_A(x,y)\right|^2 d\varepsilon \end{aligned} \tag{3-2}$$

Here $f(x,y)$ describes the object, $PSF_A(x,y)$ the electric field point spread function and

$E_i e^{-ik_i(\phi_0,\varepsilon)r}$ is the electric field with wave vector k_i.

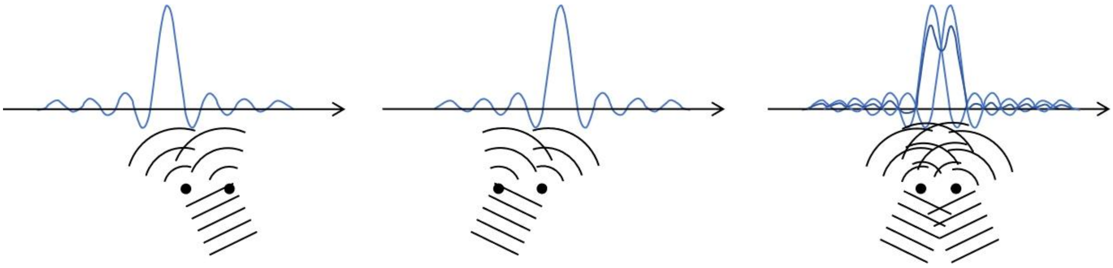

Figure 3-2. The principle of ROCS in resolving two closely spaced scattering sources.

When plane waves illuminate the particles from different angles, the scattered waves interfere, creating distinct interference patterns. These patterns contain structural information about the particles. By integrating the interference patterns from multiple illumination angles, the system enhances spatial resolution and effectively distinguishes closely spaced scattering sources. The principle is as shown in Figure 3-2.

Based on this principle, the illumination beams from different directions do not need to interfere with each other. Therefore, I can achieve the ROCS imaging effect by using multiple light sources to illuminate from different directions. As a result, I designed the system as shown in the Figure

3-3.

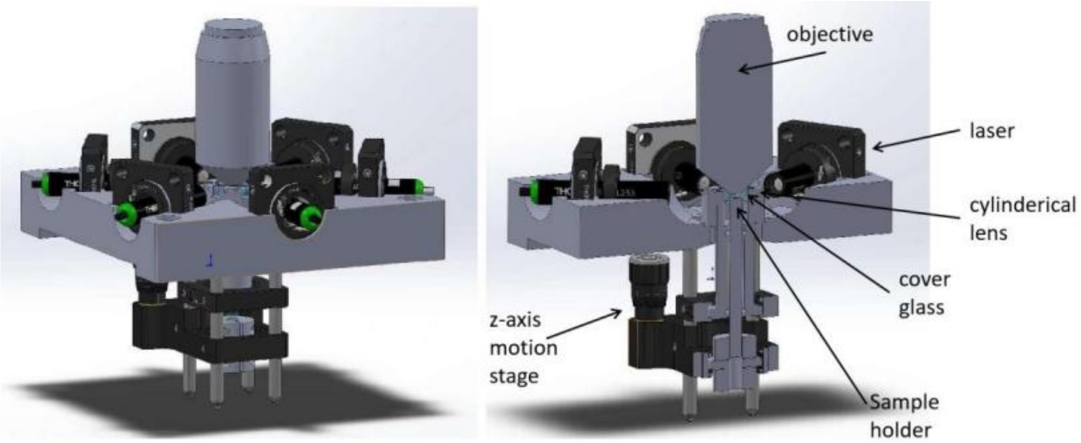

Figure 3-3. Multi-angle Light-sheet illumination design.

The entire system consists of an illumination system, a sample chamber, and an imaging system. The illumination sources are placed in six directions, each spaced 60 degrees apart. At each angle, the illumination beam is shaped into a light sheet using a combination of a collimated laser and a cylindrical lens.

The design of the sample chamber is shown in Figure 3-4. To ensure that the six light sheets enter perpendicularly without refraction, I covered the corresponding illumination windows with coverslips. The sample is placed on a vertically adjustable sample stage. To minimize diffraction and ensure effective light-sheet illumination, I embedded the sample in 2% agarose (with a refractive index of 1.335). By moving the sample stage along the z-axis, I can capture scattering images at different depths, enabling volumetric imaging.

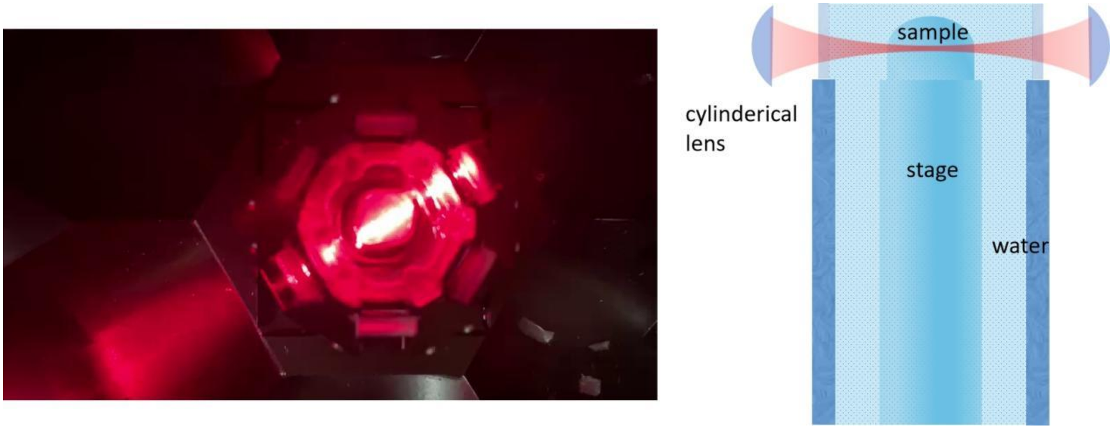

Figure 3-4. Chamber design. The sample chamber is a hexagonal water tank with six sides, each side fitted with a coverslip window to ensure the light sheet enters without distortion. A cylindrical lens is fixed outside the coverslip, and the light sheet is focused at the center of the sample chamber within the water. The sample stage consists of a glass rod vertically inserted into the chamber through a waterproof sealing ring, with its lower end mounted on a z-axis translation stage for sample scanning. Bright-field illumination is provided through the glass rod to facilitate bright-field

observation.

3.2.2 Result of Multi-angle Light Sheet Illumination

3.2.2.1 TiO_2 samples

The first testing sample is TiO_2 crystal particle clusters with size around 20 μm. By sequentially collecting images while scanning along the z-axis, I reconstructed a 3D scattering profile that clearly delineated individual particle clusters. The strong scattered signal from TiO2 validated the feasibility of our surrounding illumination strategy, demonstrating that even with only six beams (rather than the ideal twelve or more), the setup could provide high-contrast volumetric scattering data.

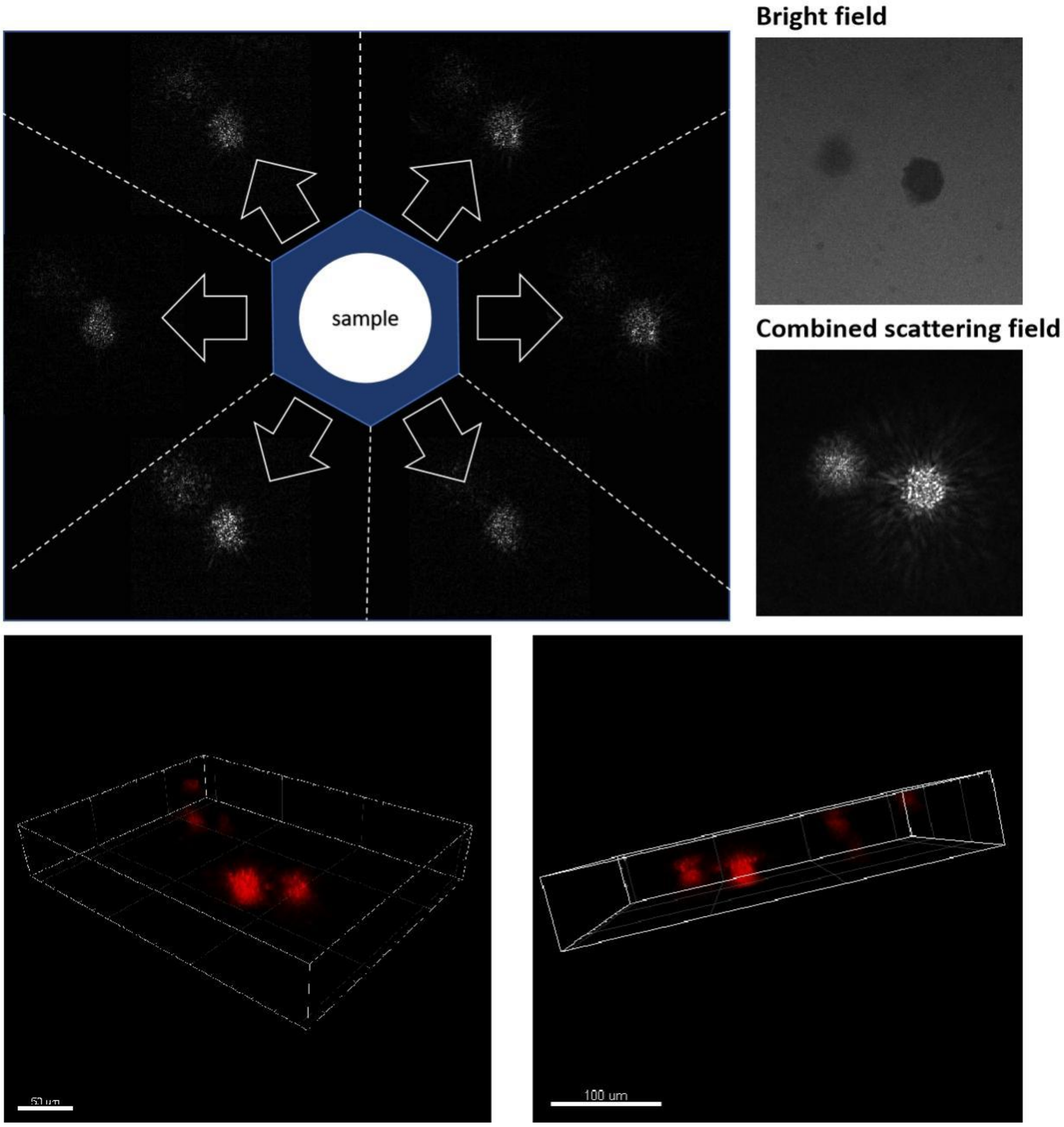

Figure 3-5. 3D Scattering Imaging of TiO_2 Particle Clusters.

When observing suspended TiO_2 powder, we noted exceptionally bright optical intensity with a high signal-to-noise ratio. To avoid overexposure, we had to reduce the laser power down to approximately

1 μW using an OD4 neutral-density filter. This high intensity results from the significant refractive index mismatch between TiO_2 (around 2.5) and water (1.33). Additionally, although we could not reconstruct the internal structure of the sample from scattering speckles, we observed regular diffraction speckle patterns as shown in the figure, which might be related to the crystalline structure of the particles.

3.2.2.2 HeLa Cells

After testing with a highly scattering sample, TiO_2, the system's tomographic capability was confirmed. Next, I conducted experiments with HeLa cells. The HeLa cells were fixed in agarose after nitration and then secured on the sample stage for scanning. The resulting 3D volumetric scattering imaging is shown in Figure 3-6.

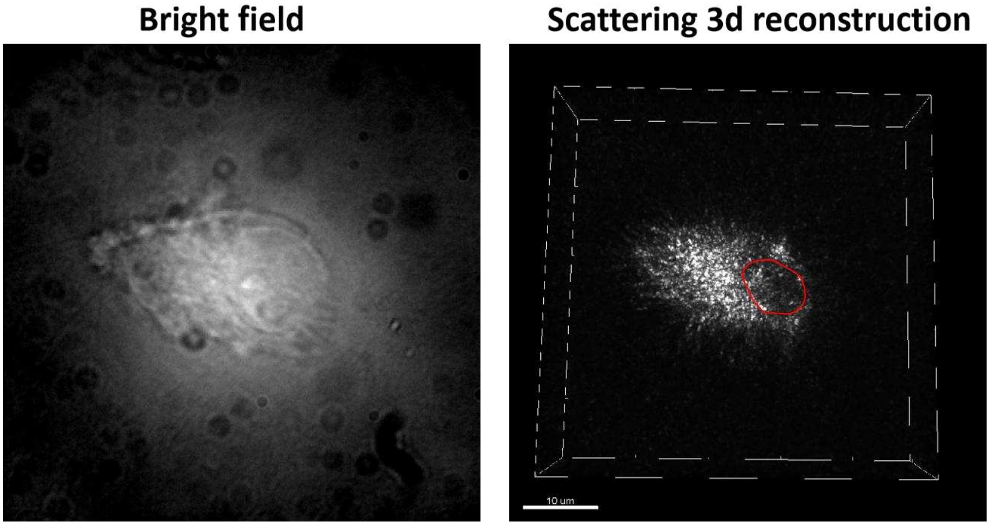

Figure 3-6. The results include both bright-field (2D) imaging and scattering-field (3D) imaging of HeLa cells. *The 2D bright-field image provides structural details of the cells in a single plane, while the 3D scattering-field image reveals volumetric scattering properties, offering deeper insights into the internal composition and refractive index variations within the cells.The red-marked region indicates the location of the cell nucleus.*

Through observing HeLa cells, we found that speckle patterns can reveal structural information from within the cell. As shown in the figure, we can clearly identify the nuclear region. Moreover, the system can be designed to perform 3D scanning, yielding three-dimensional scattering results. However, achieving ROCS-level organelle resolution using this system is challenging due to two main limitations. First, because of spatial constraints, we employed illumination from only six directions, whereas theoretically, illumination from twelve directions is required to achieve sufficient resolution. Second, the thickness of the light sheet is not much thin, causing interference between scattered light from adjacent focal planes. Additionally, the imprecise overlap of light sheets generated by multiple laser beams is also one of the factors affecting the imaging quality.

3.2.2.3 Yeast Cells

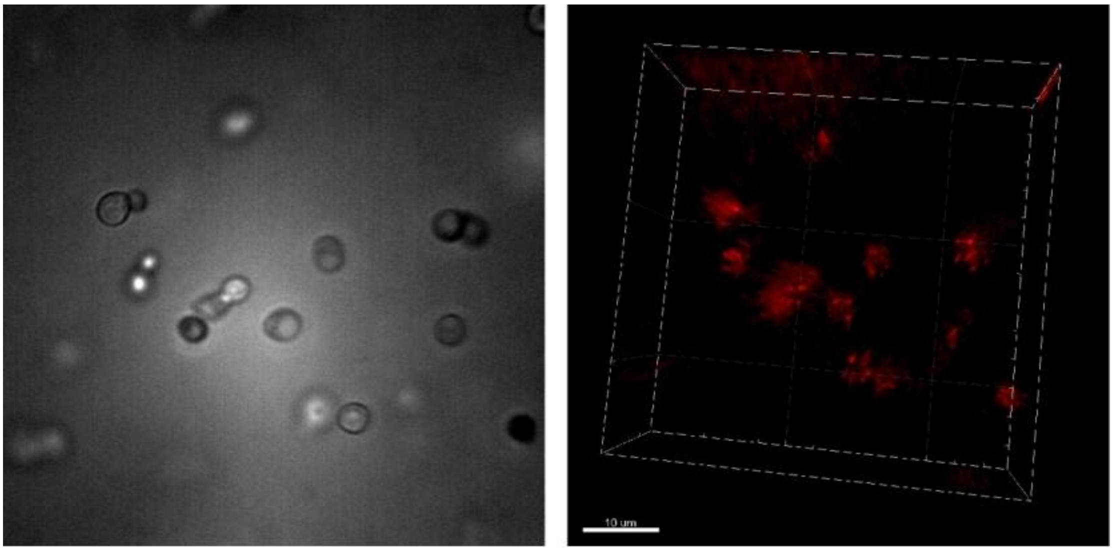

Figure 3-7.Imaging results of yeast cells. *Left: Bright-field image, Right: 3D scattering field result.*

3.2.2.4 Discussion

By scanning the sample, I identified the limitations of this design:

The numerical aperture (NA) of the cylindrical lens is approximately 0.197, and the calculated focal spot size (light-sheet thickness) is approximately 3.02 µm. This results in insufficient axial (z-axis) resolution and interference between scattering sources at different depths within the light-sheet thickness. These factors introduce challenges in reconstructing the final image, as interference signals from different layers degrade the imaging quality and resolution.

The second limitation is the restricted number of illumination angles due to spatial constraints. In theory, reconstructing ROCS images requires at least 12 illumination angles, but we were only able to incorporate 6 light sources. Additionally, aligning the light sheets precisely was already challenging, making further expansion difficult. This means that the current design relies heavily on precision engineering and control to function effectively. The impact of having an insufficient number of light sources is that fine structural details cannot be fully captured. For example, in yeast cell imaging, I observed six scattering spots on the outer layer of the cell caused by the six light sheets, resembling "highlights" reflected from a convex mirror. This phenomenon is even more pronounced in yeast cells due to their smaller size, further confirming the insufficiency of illumination angles. In contrast, if the illumination angles were sufficient, we would be able to clearly visualize the peripheral contours of the yeast cell, providing a more complete structural representation. Therefore, my second design adopts a single laser beam with a galvo lens scanning approach to cover all illumination angles.

3.2.3 Rotational light-sheet illumination

Our second design adopts a ‘reflective cup’ structure as shown in ***Figure 3-9***. By incorporating scanning mirrors (e.g., a galvo system), a single beam can be swept around the sample, forming a rotating light sheet. This arrangement is generally more straightforward to align but does require mechanical beam rotation. Moreover, fabricating the reflective cup, initially envisioned with multiple cylindrical surfaces, poses significant manufacturing difficulties. To mitigate this, I currently employ a rotating parabolic reflector in place of a fully custom, multi-cylindrical assembly. While this solution is easier to implement than its fully bespoke alternative, it still demands precise optical machining and alignment to ensure a stable, continuous rotation of the light sheet for 3D ROCS imaging.

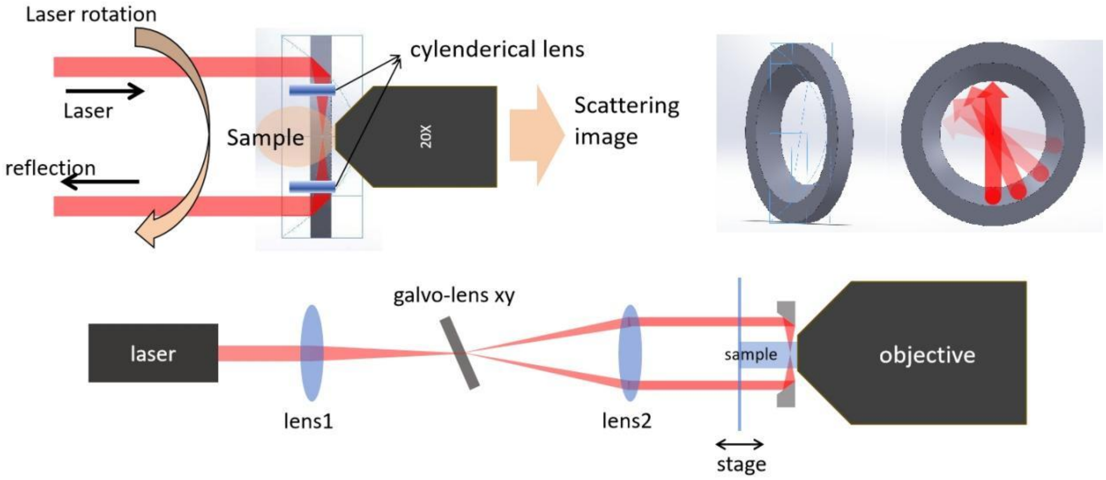

Figure 3-8. Rotational Light-sheet illumination Using Reflective-Cup.

However, using an XY dual-axis galvolens for light-sheet scanning introduces a challenge: there is a fixed distance between the two mirrors. This issue has minimal impact during point scanning with a galvanometer since field curvature correction can be applied using a scan lens to ensure that the beam remains well-focused on the imaging plane. By properly designing the scan optics, the field curvature introduced by the mirror separation can be compensated, maintaining beam alignment across the field of view.

When generating rotational light sheets, the galvanometer must produce a parallel annular scanning beam. The fixed separation between the X and Y scanning mirrors introduces a small angular deviation between the two orthogonal scanning directions, leading to misalignment in the light-sheet formation.

To correct this, I implemented two separate cylindrical lens-based 4f systems for the X and Y axes, as shown in the Figure 3-10. This design allows for the decoupling of the focal planes of the X and Y axes, ensuring that the scanned beam paths remain parallel, which is critical for maintaining a properly aligned rotational light-sheet illumination.

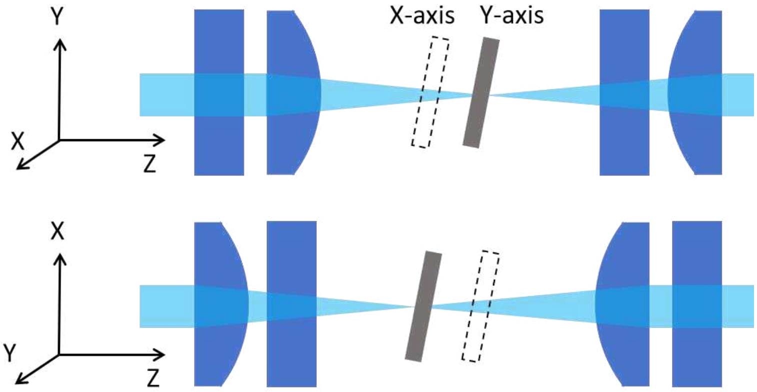

Figure 3-9. A 4f system composed of two sets of cylindrical lenses is used to correct the scanning angle mismatch caused by the distance between the X and Y galvo mirrors. The two sets of cylindrical lenses are placed orthogonally, with the X and Y galvo mirrors located at the Fourier (frequency) planes of their respective 4f systems. C: cylindrical lens.

This approach effectively compensates for the XY galvo mirror separation, allowing the system to generate a uniform and correctly oriented annular scanning light beam for rotational light-sheet imaging.

3.2.4 Result of Rotating Reflection light-sheet illumination

3.2.4.1 Pancreatic Islet Cell.

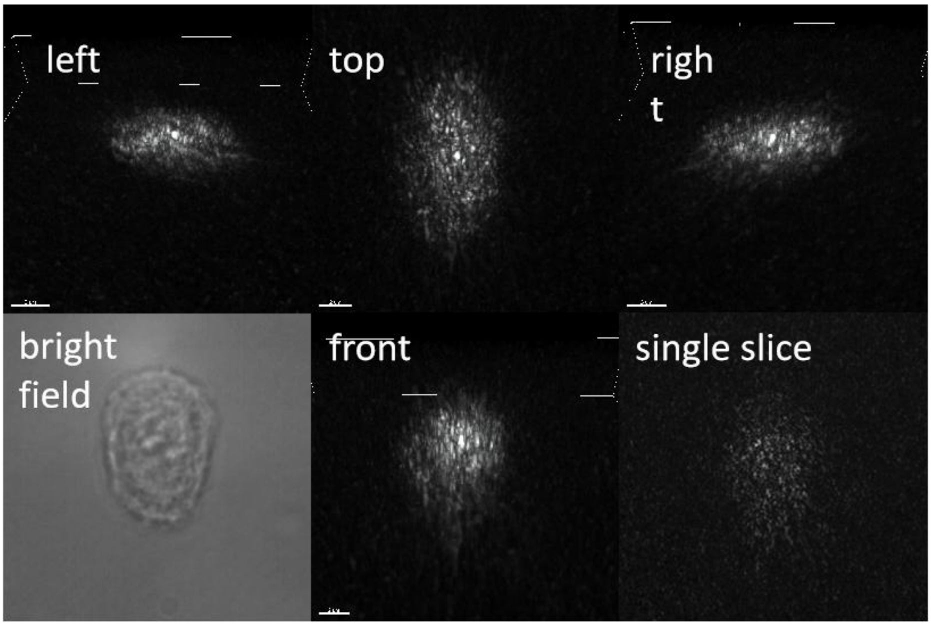

Figure 3-10. Volumetric Scattering Images of a Pancreatic Islet Cell.

Using our second design, a reflective cup with parabolic mirror arrangement coupled with a galvolens, I obtained volumetric scattering images of pancreatic islet cells. By rotating the light sheet around the specimen, I captured scattering data across multiple angles, then compiled these individual views into a 3D reconstruction. The resulting dataset reveals the distribution of scattering features within the islet cells, offering insight into their internal morphology without the use of fluorescent dyes. This improved design, which replaces multiple discrete beams with a single rotating sheet, simplifies optical alignment compared to the multibeam setup while still achieving high-contrast, volumetric ROCS imaging of delicate biological structures.

3.2.4.2 AC16 cell

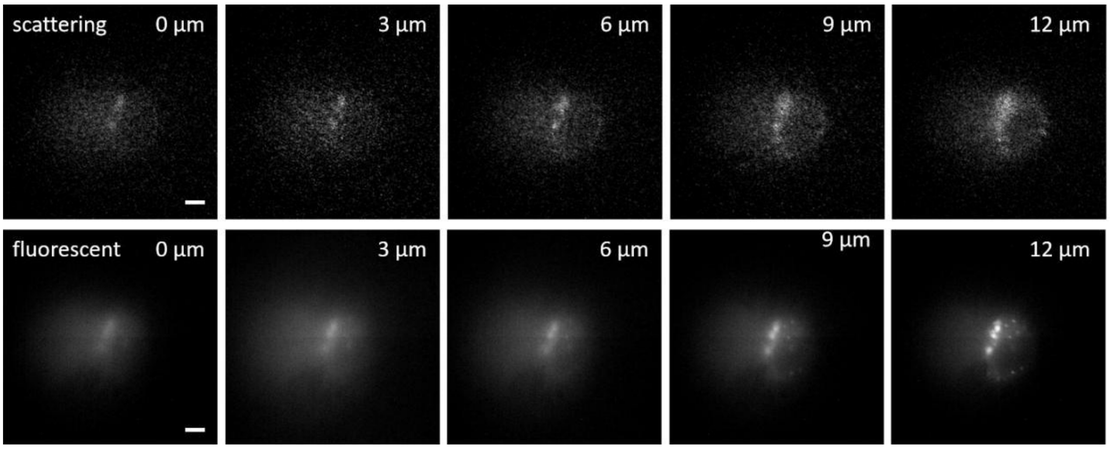

Figure 3-11. Rotational light sheet scanning result of an AC16 cell slice from 0 to 12 μm. Top: scattering, bottom: fluorescent.

As shown in ***Figure 3-10***, we performed scanned imaging of AC16 cells. In this system, a 488 nm laser was used as the light source. When a 500 nm long-pass filter was placed in the detection path, the system functioned as a light-sheet scanning setup. The top row of the figure shows selected scattering-based light-sheet scan slices, while the bottom row presents the corresponding fluorescence images obtained from light-sheet imaging.

3.2.4.3 Yeast cells

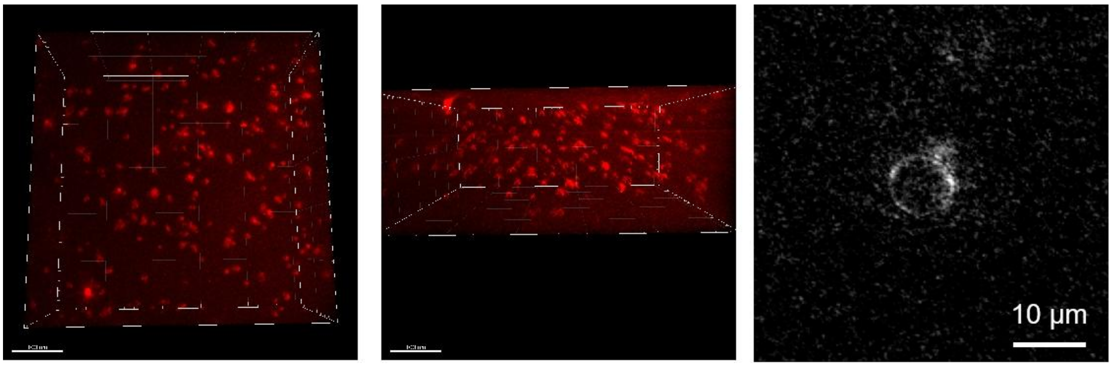

Figure 3-12. Imaging results of yeast cells: Left: top view; Meddle: front view Right: single yeast cell with scattering imaging.

I embedded the yeast cells in 2% agarose for immobilization. As shown in ***Figure 3-12***, I used this system to scan approximately 100 μm in depth across a 300 μm field of view. The image shows the reconstructed 3D scattering field from the scan. Consistent with our intended improvement goals, the new design no longer shows the six highlight spots when observing yeast cells. Instead, the outline of the yeast cells are observed. This indicates that the bright spots on the previous yeast contour were caused by incomplete angles.

3.2.4.4 Spherical organoids

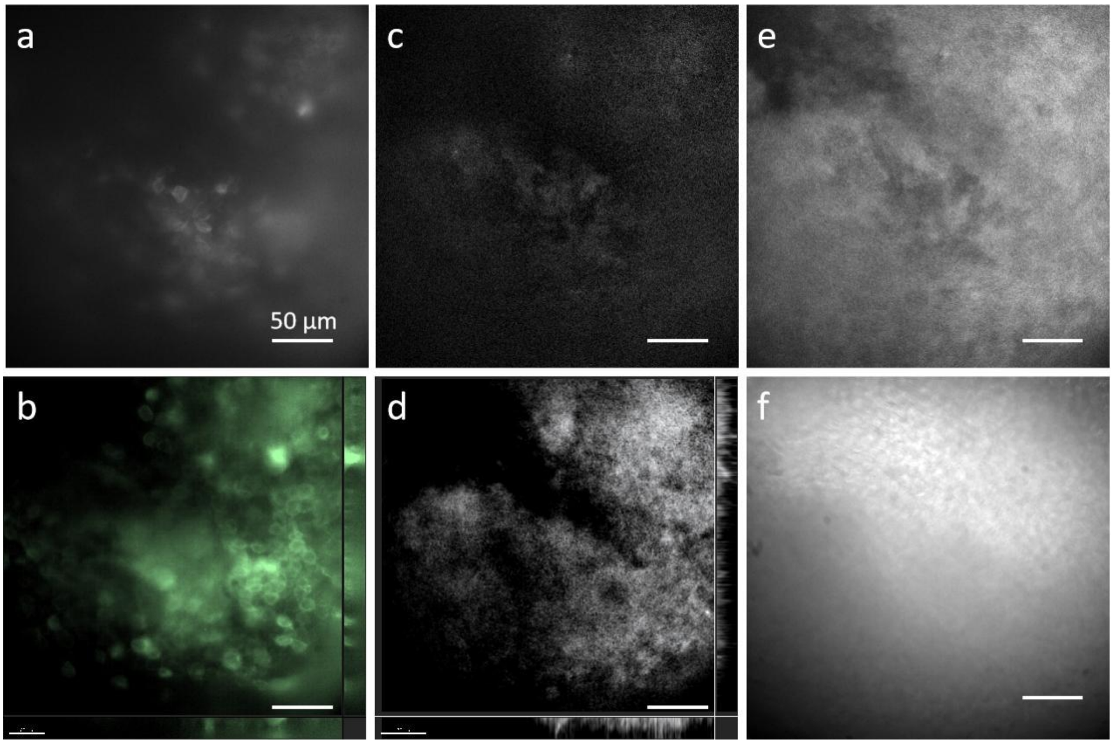

Figure 3-13. Rotational light-sheet scanning results of spherical organoids. (a) Fluorescence single-layer image at slice 0 μm (b) 3D fluorescence scanning result (c) Scattering image at slice 0 μm (d) 3D scattering field scanning result (e) Standard deviation along the z-axis of the 3D scattering field (f) Bright-field image.

3.2.5 Discussion

In the new design, we primarily addressed the issue of insufficient angles. This allows the sample under rotating light sheet illumination to display more structural information rather than a random scattering pattern. However, my original design generated the rotating light sheet by combining multiple parabolic cylindrical mirrors with parallel beam scanning. Due to the high precision requirements and complexity of fabrication, I opted to generate the light sheet using a parabolic mirror with a cylindrical lens instead. The drawback is that the annular cylindrical lens array produced intense reflected light, resulting in a pronounced scattering background, and the reconstruction results do not exhibit as high a signal-to-noise ratio as the previous design. I still plan to implement rotating light sheet illumination using parabolic cylindrical mirrors, as shown in the ***Figure 3-14***.

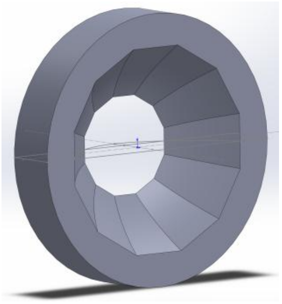

Figure 3-14. In the parabolic cylindrical mirror design, parallel incident light will be focused at the center into a light sheet.

Another point I'd like to discuss is that when imaging organoids, due to their large size and complex structure, the light sheet becomes scattered during deep scanning, making it difficult to maintain structured illumination. One potential solution is to use a NIR-II light source as the illumination laser to increase imaging depth.

3.3 Conclusion and Thoughts

3.3.1 Advantages and Perspective

Label Free Morphological Contrast

The scattering-based images reveal fine structural features within both inorganic samples (TiO_2) and biological specimens (HeLa and pancreatic islet cells) that are not readily apparent in standard bright-field views. This highlights the potential of scattering contrast to elucidate subcellular details without exogenous labels, thus preserving native physiological conditions. Moreover, since the intensity of scattered light is three to four orders of magnitude higher than that of fluorescence, much lower illumination power is required, making it less likely to cause damage to the cells.

High-speed Volumetric Perspective

ROCS itself is an inherently fast, label-free imaging method capable of reaching at least 100 Hz. In addition to enhancing the imaging from 2d to 3d, our use of multi-beam illumination enables even faster imaging speeds. This is because multiple lasers can illuminate simultaneously, eliminating the need for rotational scanning time. For future improvements, I would opt for more precisely fabricated optical structures and use smaller optical components, such as optical fibers, to achieve more illumination angles.

Modular integration.

Both of my design approaches feature detachable, modular configurations that can be integrated into standard upright or inverted microscopy systems. This flexibility allows for easy adaptation to various experimental setups and imaging needs without requiring significant modifications to existing platforms. Moreover, the modular nature enables rapid switching between different imaging modes, such as fluorescence, scattering, or bright-field, by simply reconfiguring specific components. This not only enhances system versatility but also facilitates future upgrades, such as incorporating additional illumination angles, higher-precision optics, or automated scanning modules to further improve imaging speed and resolution.

3.3.2 Challenge and solutions

3.3.2.1 Design of Rotational light sheet illumination

The design of a rotational light sheet is a challenge because several requirements have to be met at the same time:

firstly, the light sheet has to be thin enough to prevent the scattered light from the upper and lower layers from interfering and affecting the image reconstruction, which requires a sufficient numerical aperture for the focusing of the light sheet, secondly, the illumination of each angle needs to be overlapped, otherwise it will result in the loss of the scattered field of a part of the angle affecting the reconstruction, which requires a sufficiently high machining accuracy, and finally, the space has to be taken into account , because the working distance of the high NA objective lens is short.

Multi-laser, multi-angle illumination remains a viable solution. One approach is to achieve an integrated array configuration using micro-devices such as optical fibers and metasurfaces, thereby enabling sufficient multi-angle light sheet illumination within a limited space. For the single-beam scanning scheme, designed DOE devices and grating devices can replace parabolic cylindrical mirrors to meet spatial requirements and reduce fabrication complexity.

3.4 Reference

1. Sung, Y., et al., *Optical diffraction tomography for high resolution live cell imaging.* Optics express, 2009. **17**(1): p. 266-277.
2. Kim, K., et al., *Optical diffraction tomography techniques for the study of cell pathophysiology.* Journal of Biomedical Photonics & Engineering, 2016. **2**(2).
3. Jünger, F., et al., *100 Hz ROCS microscopy correlated with fluorescence reveals cellular dynamics on different spatiotemporal scales.* Nature Communications, 2022. **13**(1): p. 1758.
4. Ruh, D., et al., *Superior contrast and resolution by image formation in rotating coherent scattering (ROCS) microscopy.* Optica, 2018. **5**(11): p. 1371-1381.
5. Jünger, F., P.v. Olshausen, and A. Rohrbach, *Fast, label-free super-resolution live-cell imaging using rotating coherent scattering (ROCS) microscopy.* Scientific reports, 2016. **6**(1): p. 30393.
6. Saguy, A., et al., *Deep-ROCS: from speckle patterns to superior-resolved images by deep learning in rotating coherent scattering microscopy.* Optics Express, 2021. **29**(15): p. 23877-23887.
7. Koch, M.D. and A. Rohrbach, *Label-free imaging and bending analysis of microtubules by ROCS microscopy and optical trapping.* Biophysical journal, 2018. **114**(1): p. 168-177.

8. Kleinman, D.A., *Theory of second harmonic generation of light.* Physical Review, 1962. **128**(4): p. 1761.
9. Fish, K.N., *Total internal reflection fluorescence (TIRF) microscopy.* Current protocols in cytometry, 2009. **50**(1): p. 12.18. 1-12.18. 13.
10. Masters, B.R., *Richard Zsigmondy and Henry Siedentopf's Ultramicroscope*, in *Superresolution Optical Microscopy: The Quest for Enhanced Resolution and Contrast*. 2020, Springer International Publishing: Cham. p. 165-172.
11. Nguyen, C.D., et al., *Scattering-based light-sheet microscopy for rapid cellular imaging of fresh tissue.* Lasers in surgery and medicine, 2021. **53**(6): p. 872-879.
12. Zhou, X., et al., *Light-sheet scattering microscopy to visualize long-term interactions between cells and extracellular matrix.* Frontiers in immunology, 2022. **13**: p. 828634.
13. Zhao, J., et al., *Investigation of different wavelengths for scattering-based light sheet microscopy.* Biomedical Optics Express, 2022. **13**(7): p. 3882-3892.
14. Subedi, N.R., et al., *Scattered-light-sheet microscopy with sub-cellular resolving power.* Journal of Biophotonics, 2023. **16**(9): p. e202300068.

4 Fiber Encoded Orthogonal Light Sheet Illumination

4.1 Introduction

In recent years, the miniaturization and integration of optical systems have become key directions of development[1-3]. So far, free-space light field modulation techniques, exemplified by light-sheet microscopy, have reached a high level of maturity. They provide high-resolution, low-damage imaging solutions while demonstrating strong adaptability to complex experimental environments and diverse application needs. With the rapid development of fields such as mobile equipment, AR/VR, optical quantum computing, medical imaging, and biological research, the miniaturization of optical systems has become a necessary requirement. In the field of microscopic imaging, many studies have integrated complex optical systems into modular chips[4-8].

Despite the remarkable progress made in free-space light field modulation, effectively deploying these techniques in highly constrained or miniature systems remains challenging. For instance, endoscopic imaging typically must fit within narrow fiber channels or rigid mechanical supports, leaving insufficient room for complex optical components. Similarly, light-sheet microscopy often demands orthogonally arranged objectives or complex illumination modules, making it difficult to integrate into compact setups like microfluidic devices or organs-on-a-chip. Additionally, tailoring illumination arrays to specialized configurations, such as large-scale parallel scanning or custom-designed focal patterns, which can be prohibitively complex when space is limited. These constraints not only limit the flexibility and customization of advanced imaging techniques but also highlight the need for novel approaches that can achieve high-performance light field modulation while meeting strict size and geometry requirements.

A promising approach to overcoming these spatial and design constraints lies in the use of multimode fibers (MMFs) for light field control. Unlike conventional fiber bundles, which rely on distinct cores acting as pixels, a single MMF supports numerous propagation modes that can be individually addressed and manipulated. Over the past decade, advances in wavefront shaping, adaptive optics, and computational methods have paved the way for precise control of light through MMFs, enabling high-resolution imaging, targeted illumination, and minimally invasive diagnostics. By measuring and compensating for the complex transmission characteristics of an MMF (often referred to as its ‘transfer matrix’), researchers can generate customized beam profiles at the fiber output that ranging from single focal spots to structured illumination patterns. Such breakthroughs have already proven valuable in endoscopic imaging, fiber-based optical trapping, and other scenarios where space is severely limited. As these methods continue to mature, the potential to integrate MMFs into miniaturized microscopy systems holds great promise for bridging the gap between advanced light field modulation and the ever-increasing demand for compact, versatile imaging solutions.

Early demonstrations of single MMF imaging primarily relied on the measurement of a so-called

‘Transfer Matrix’ (TM), which relates the input field to the output field of the fiber. Pioneering work by Vellekoop and Mosk introduced the concept of wavefront shaping through scattering media, laying the groundwork for controlling light fields in disordered or multimodal waveguides. Popoff and colleagues further refined TM-based approaches, establishing a robust framework for precise optical field manipulation. Building on these principles, researchers such as Qing. Y et al.[9] devised the STABLE system for reliable transmission correction in MMFs, achieving consistent beam shaping even under slight fiber deformations. Meanwhile, Zhang. Q et al.[10] explored deep-learning-enhanced methods, printing neural network-trained phase masks for real-time image reconstruction at the fiber output. Other groups have advanced techniques like AOD-based temporal scanning (Martin et al.) to generate structured light fields and enable advanced imaging modes.

Collectively, these breakthroughs illustrate the rapidly evolving capabilities of MMF-based light field manipulation. By accurately measuring and compensating for modal mixing, MMFs can deliver tailored illumination patterns with its size that as thin as human hair. This ultra-compact form factor holds immense promise for miniature microscopy and integrated imaging systems, offering a powerful solution to the spatial constraints that hamper traditional free-space methods.

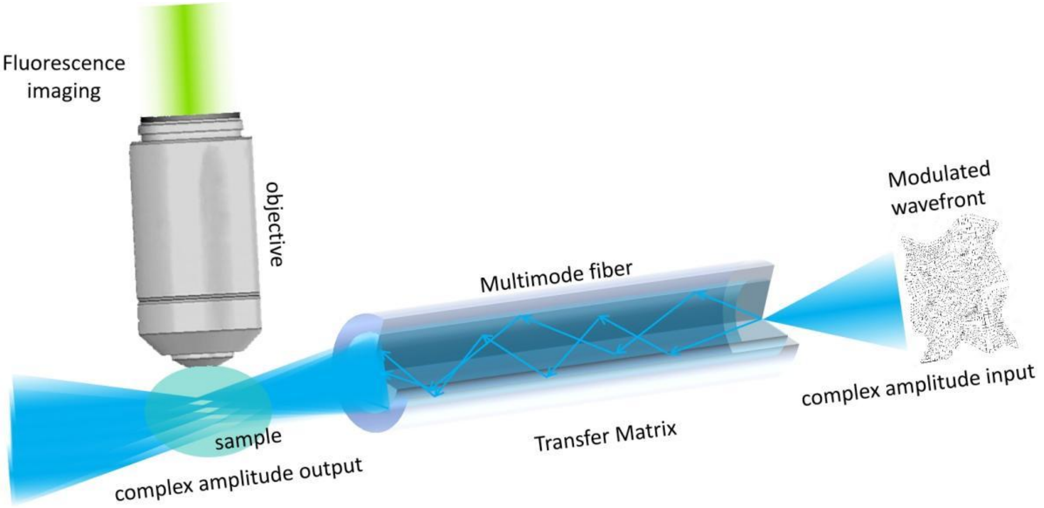

Figure 4-1. Schematic Diagram of Structured Light Sheet Illumination Using a Single Multimode Fiber.

Our approach seeks to integrate multimode fiber (MMF) light field modulation with light-sheet microscopy, leveraging the compact footprint of a single fiber to deliver highly adaptable illumination. By measuring and compensating for the fiber’s transfer matrix, I can shape the output beam into various light-sheet configurations, such as Gaussian, Bessel, or multiplexed arrays, while preserving the system’s miniature form factor. This small-scale solution not only addresses the space limitations inherent in conventional light-sheet setups but also enables fast scanning and array-based illumination for more efficient imaging across a wide field of view.

Moreover, the inherent flexibility of MMFs allows us to envision fully integrated, chip-scale modules capable of replacing or augmenting traditional illumination objectives. Such modules could be directly attached to standard microscopes, sidestepping the need for bulky, orthogonally arranged optics. Their versatility extends to microfluidic platforms and other confined environments, paving the way for large-scale parallel measurements and simplified alignment procedures. In the future, these fiber-based micro light field modulators could form building blocks for highly customized, plug-and-play imaging systems which bringing the benefits of advanced wavefront shaping and light-sheet microscopy to broader applications in biology, materials science, and beyond.

Existing efforts to combine multimode fibers (MMFs) with advanced beam shaping have largely focused on measuring and compensating for the fiber's complex transmission characteristics. For example, Ploschner et al[11]. demonstrated an AOD-based approach for generating Bessel beams array through temporal scanning, while other teams employed iterative algorithms or off-axis holography for wavefront shaping. However, these methods often rely on additional hardware components and can be limited by lengthy calibration times or insufficient spatial resolution.

Our work introduces several key innovations. First, I simplify the TM measurement by orthogonalizing input scanning patterns, thereby accelerating data acquisition and improving the stability of TM calibration. This allows for direct matrix operations with minimal computational overhead, eliminating the need for extra devices such as acoustic-optic deflectors (AODs). Second, I expand the TM's capacity by measuring and storing a larger set of orthogonal modes, thereby enabling higher-resolution beam modulation reducing modes crosstalk. Finally, by incorporating only the spatial light modulator (SLM) for both calibration and wavefront shaping, I achieve light field control in the multimode fiber with a more simple optical setup. Collectively, these optimizations yield faster calibration, higher fidelity beam shaping, and a more compact system architecture, critical steps toward practical, integrated light-sheet microscopy in confined or miniaturized settings.

4.1.1 Structured Light-sheet Illumination on Fiber Tip

The spatial limitations of light-sheet microscopy primarily arise from the requirement for two orthogonally arranged objectives, one for illumination and the other for detection, which demands a large working space and precise alignment. This setup can pose challenges when imaging large or complex samples, as the orthogonal geometry restricts access to the sample and may require specially designed chambers or mounting systems. Additionally, the bulky configuration can make integration into confined experimental setups, such as microfluidic devices or organ-on-chip systems, difficult. To address these challenges, several innovative solutions have been developed. Single-objective light-sheet microscopy (SOLS) eliminates the need for orthogonal objectives by using reflective surfaces, microprisms, or dynamic beam shaping techniques to introduce the light sheet along the detection path. These advancements not only overcome spatial constraints but also enhance the adaptability of light-sheet microscopy for diverse biological applications.

However, single-objective light sheet illumination restricts the numerical aperture of the illumination path. This work proposes the use of multi-mode optical fibers for generating structured light sheets in light-sheet microscopy. Multi-mode fibers allow for remote light-field modulation and can deliver high-quality structured light to confined spaces, such as microfluidic chambers or regions inaccessible to conventional objectives. This approach offers several advantages, including space savings, system integration, and flexibility. Multi-mode fibers can be used to form arrays of light sheets, enabling wide-field, high-resolution imaging in compact setups. The integration of such fiber-based light sheets into current microscopy systems could address existing bottlenecks, particularly in small-animal and microfluidic imaging, by providing efficient, scalable, and versatile solutions. This innovation holds the potential to significantly advance the capabilities of light-sheet microscopy, making it more accessible and adaptable for a wide range of applications.

A previous study has demonstrated the feasibility of generating a light sheet using a multimode fiber. Martin et al. achieved this by employing AOD-based temporal scanning to form both light sheets and structured optical fields at the fiber output[11]. Building upon their theoretical foundation, I developed an approach that directly modulates structured light at the fiber output without requiring AOD. Additionally, I simplified the acquisition and computation of the transfer matrix (TM), significantly accelerating the previously complex calibration process. By directly measuring the TM without requiring matrix inversion, I achieve higher-resolution optical field control at the fiber output without increasing computational time.

4.2 Methodology

4.2.1 Fiber encoded Light-field modulation Using SLM

To achieve flexible beam shaping through a single MMF, I use a spatial light modulator (SLM) to encode complex wavefronts at the fiber input. By carefully calibrating how light propagates through the fiber, I can generate user-defined output fields, ranging from a single tightly focused spot to structured beam arrays, without needing large, orthogonally arranged optics or additional scanning devices such as AODs. Below, I outline the core elements of our method, focusing on zero-order light management, selection of the diffraction order, and the off-axis holographic measurement of complex amplitude.

4.2.1.1 Placement of the SLM and Zero-Order Light Elimination

Since the SLM is placed in the Fourier plane relative to the fiber input facet, each point on the SLM corresponds to a distinct spatial frequency component at the fiber. A key challenge in phase-only SLM systems is the presence of zero-order light, unwanted reflections and unmodulated residual light, which degrade beam quality and reduce the accuracy of wavefront shaping. To mitigate these effects:

Blazed Grating Superposition

A 45° blazed grating is added to the target phase pattern on the SLM, shifting the primary diffracted beam away from the zero-order in the Fourier plane. By selecting an appropriate grating period, I redirect the modulated light into a ‘clean’ region, minimizing interference from zero-order and pixelated diffraction artifacts as shown in ***Figure 4-2***.

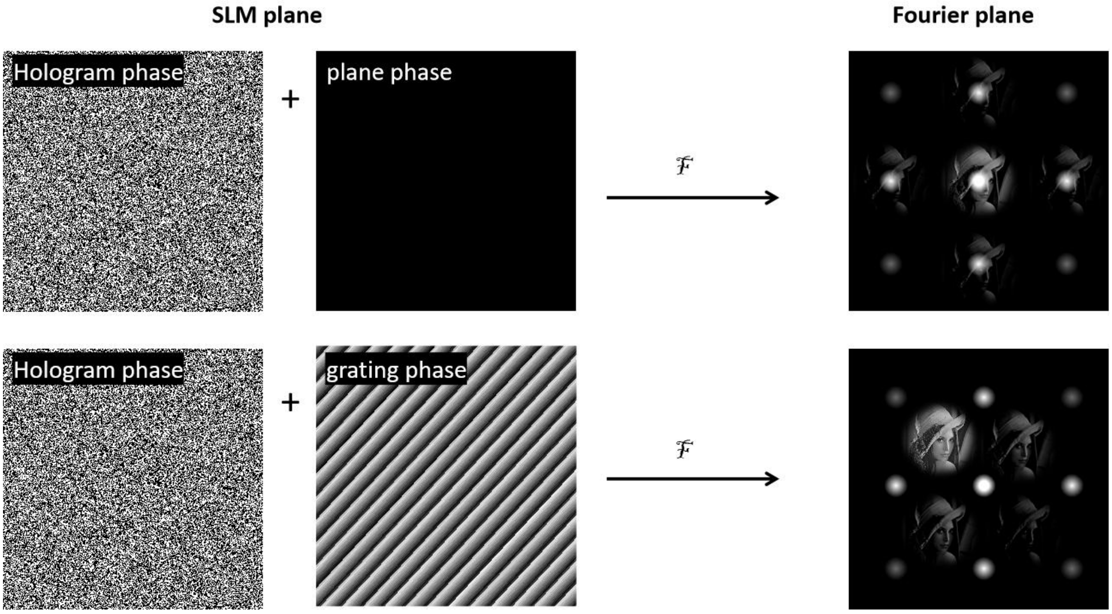

Figure 4-2. Schematic diagram of the method for avoiding intrinsic diffraction from the SLM by using a grating-based phase shift.

This is also important for the subsequent transfer matrix measurement, because I use the primary light as a reference beam incident on the objective and align its focus to the center of the optical fiber. The subsequent scanning measurement process is based on this reference, whether it is P-polarized or S-polarized light. The procedure is very simple; there is no need to actually compute the phase after superimposing the grating. Since the fiber end is equivalent to the Fourier plane of the SLM, performing an inverse Fourier transform on the complex amplitude in the light plane yields the phase on the SLM. Now, to avoid the diffraction spots from the SLM, we simply shift the target complex amplitude by 45 degrees before performing the inverse Fourier transform.

4.2.1.2 Focusing Energy into the First-Order Diffraction

Our approach adopts a single diffraction order strategy, meaning I direct most of the optical energy into the first-order of the applied grating. By fine-tuning the grating parameters on the SLM:

A. Maximized Energy Efficiency

Concentrating optical power into a single diffraction order improves the SNR at the fiber output, benefiting high-resolution applications such as light-sheet microscopy.

In our approach to diffraction order selection, I adopt a single-order strategy, where only the first-order diffracted light from the SLM is used. By adjusting the diffraction angle of the grating, I can concentrate most of the optical energy into the first-order diffraction position, maximizing the efficiency of light modulation.

The intensity of the first-order diffraction can be expressed by the following formula:

$$I_1 = \left(\frac{\sin(\pi d \sin\theta/\lambda)}{\pi d \sin\theta/\lambda}\right)^2 \tag{3-1}$$

B. Adjustable Intensity Control

The diffraction efficiency can be modulated to control illumination intensity during beam scanning and shaping. This is useful for balancing illumination brightness with sample phototoxicity or other experimental constraints.

4.2.1.3 Off-Axis Holographic Measurement of Complex Amplitude

A. Single-Shot Complex Field Acquisition

In optical field modulation through fibers, most methods require capturing the complex amplitude distribution at the fiber output. Typically, cameras and imaging systems can only capture the intensity information of the optical field, which corresponds to the amplitude distribution. However, in optical field computations, I require the complex amplitude, which includes both amplitude and phase information. Traditional optical field phase measurement requires the three-step phase-shifting method. The method relies on recording four interference intensity images while introducing a controlled phase shift between the reference beam and the object beam. The interference intensity at each step is given by:

$$I_k(x,y) = I_o(x,y) + I_r(x,y) + 2\sqrt{I_o(x,y)I_r(x,y)}\cos(\phi(x,y) + \Delta\phi_k) \tag{3-2}$$

Where:

$I_k(x,y)$ is the recorded intensity at step k.

$I_o(x,y)$and $I_r(x,y)$ are the intensities of the object beam and the reference beam, respectively.

$\phi(x,y)$ is the unknown phase to be measured.

$\Delta\phi_k$ is the phase shift introduced at step k.

The four-step phase shifts are typically:

$\Delta\phi_1$=0°, $\Delta\phi_2$=90°, $\Delta\phi_3$=180°, $\Delta\phi_4$=270°

By capturing four intensity images under these conditions, the phase can be extracted using:

$$\phi(x,y) = \tan^{-1}\left(\frac{I_4 - I_2}{I_1 - I_3}\right) \tag{3-3}$$

In contrast, the off-axis holography method does not require four separate measurements but instead captures a single measurement without altering the phase. Off-axis holography is an interferometric imaging technique used to measure the complex amplitude (both phase and intensity) of an optical wavefront. It is widely applied in quantitative phase imaging (QPI), digital holographic microscopy (DHM), and wavefront sensing.

A recorded off-axis hologram results from the interference between the object wave

$\mathrm{E_{obj}}(\mathrm{x}, \mathrm{y})$ and the reference wave $\mathrm{E_{ref}}(\mathrm{x}, \mathrm{y})$, given by:

$$I(x, y) = \left|E_{\mathrm{obj}}(x, y) + E_{\mathrm{ref}}(x, y)\right|^2$$

$$= \left|E_{\mathrm{obj}}(x, y)\right|^2 + |E_{\mathrm{ref}}(x, y)|^2 + E_{\mathrm{obj}}(x, y)E_{\mathrm{ref}}^*(x, y) + E_{\mathrm{obj}}^*(x, y)E_{\mathrm{ref}}(x, y) \qquad (3\text{-}4)$$

Where:

The first two terms represent intensity contributions from the object and reference waves.

The last two terms represent the interference pattern, containing phase information.

Since the reference wave is tilted, the interference terms appear at nonzero spatial frequencies in Fourier space.

Taking the Fourier transform of the hologram:

$$\mathcal{F}[I(x, y)] = \mathcal{F}\left[\left|E_{\mathrm{obj}}\right|^2\right] + \mathcal{F}[|E_{\mathrm{ref}}|^2] + \mathcal{F}\left[E_{\mathrm{obj}}E_{\mathrm{ref}}^*\right] + \mathcal{F}\left[E_{\mathrm{obj}}^*E_{\mathrm{ref}}\right] \qquad (3\text{-}5)$$

A bandpass filter is applied to isolate the first-order term, after inverse Fourier transform:

I get $E_{\mathrm{obj}}^*E_{\mathrm{ref}}$. Assuming a plane wave reference $E_{\mathrm{ref}} = A_{\mathrm{ref}}e^{i\phi_{ref}}$, I obtain:

$$E_{\mathrm{obj}}(x, y) = \frac{E_{\mathrm{obj}}(x,y)E_{\mathrm{ref}}^*(x,y)}{A_{\mathrm{ref}}e^{-i\phi_{\mathrm{ref}}}} \qquad (3\text{-}6)$$

$$\phi_{obj}(x, y) = arg(E_{obj}(x, y)) \qquad (3\text{-}7)$$

B. Digital Reconstruction

After filtering out unwanted terms, an inverse Fourier transform recovers the amplitude and phase distribution of the output beam. Unlike four-step phase-shifting methods, off-axis holography acquires the necessary phase information in a single shot, reducing measurement time and mitigating potential drift.

C. Phase drift correction

To ensure accurate measurements, phase drift correction is implemented by introducing fixed patterns during the scanning process. As shown in the Figure 4-3, alternating between scanning modes and fixed reference patterns allows us to continuously monitor and correct for phase fluctuations over time. The fixed patterns serve as calibration points, enabling real-time compensation for any drift that occurs due to environmental instability, optical misalignment, or system fluctuations.

The impact of this correction is evident in the before-and-after comparison on the right. Before correction, the phase drift results in a blurred, scattered intensity pattern, while after applying the calibration-based correction, the system achieves a highly focused and stable optical output. This method significantly enhances wavefront shaping accuracy and robustness, making it essential for applications in high-resolution optical imaging, fiber-based beam delivery, and precision laser focusing.

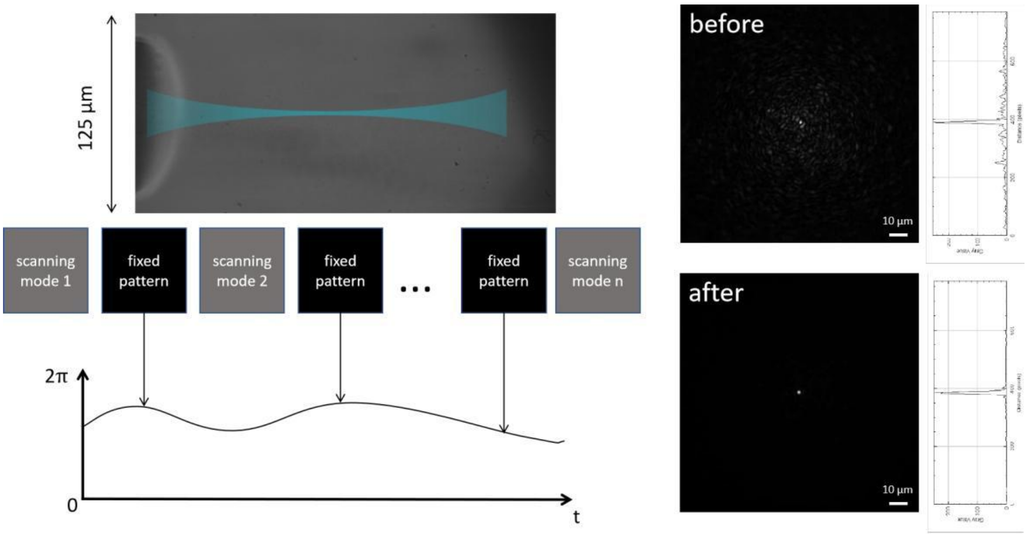

Figure 4-3. Comparison of Focused Spot Performance Before and After Phase Drift Calibration.

4.2.2 Measurement of Transfer Matrix

Here, I introduce a method for measuring the transfer matrix (TM), with the detailed process illustrated in the Figure 4-4. I model the optical field propagation from the input end of the fiber to the target output plane as a transfer matrix operation. Let the input and output optical fields be denoted as E_{in} and E_{out}, respectively. The relationship is expressed as:

$$E_{out} = TM * E_{in} \tag{3-8}$$

Conversely, for a known target output field, the required input field can be obtained by:

$$E_{in} = TM^{-1} * E_{out} \tag{3-9}$$

The TM describes the contribution of each input optical field to the output optical field and can be expressed as :

$$E_m^{\text{out}} = \sum_n k_{mn} E_n^{\text{in}} \tag{3-10}$$

If the identity matrix is used as the E_{in} measurement sequence, the measurement of the transfer matrix (TM) becomes straightforward:

$$E_{out} = TM * I = TM \tag{3-11}$$

Where I is the identity matrix, meaning that each input mode is illuminated one at a time while all others remain off. This method simplifies the measurement of TM by ensuring that each input mode directly corresponds to a column in the TM, allowing for straightforward calibration and reconstruction of the optical field propagation.

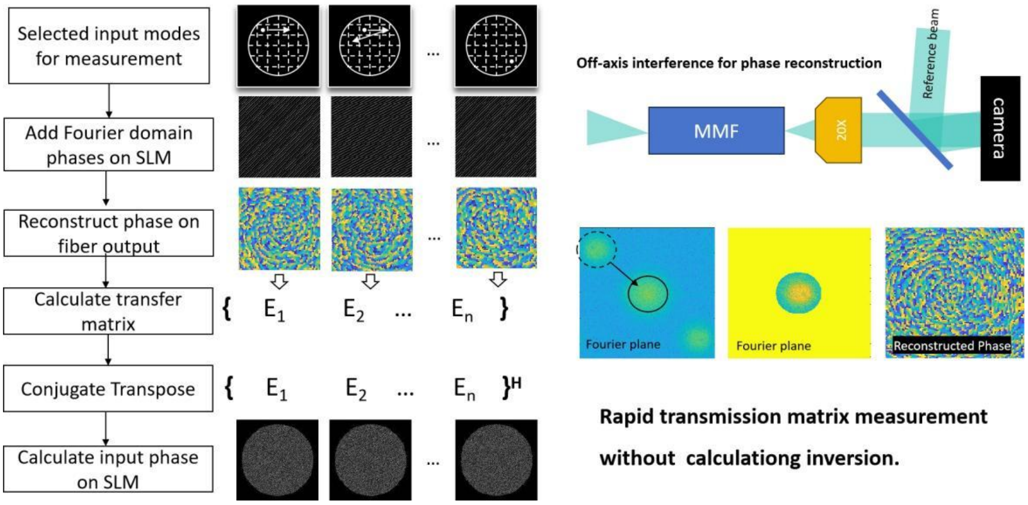

Figure 4-4. The process of measuring the transfer matrix and calculating the phase to be loaded onto the SLM.

In practical measurements, a focused single-point beam is used to scan the input optical field. The input optical field E_{in} can be regarded as a complex amplitude matrix with fully orthogonal columns, while E_{out} is not fully orthogonal. This means that the measured TM is not orthogonal.First, I need to have a clear understanding of the size of the TM. If the target output optical field has a resolution of $N \times N$ and the TM requires 1000 measurements, then the size of the TM should be $N^2 \times 1000$. This means that increasing the optical field resolution from 128 to 256 would expand the TM from $16{,}384 \times 1000$ to $65{,}536 \times 1000$, significantly increasing the computational complexity of matrix inversion. I considered that if the TM were orthogonalized, the computation would become much simpler, as its inverse would simply be its conjugate transpose. Since E_{out} corresponds to each column of the TM, I only need to select appropriate discrete points at the input to ensure that the output optical fields E_{out} satisfy the orthogonality condition.

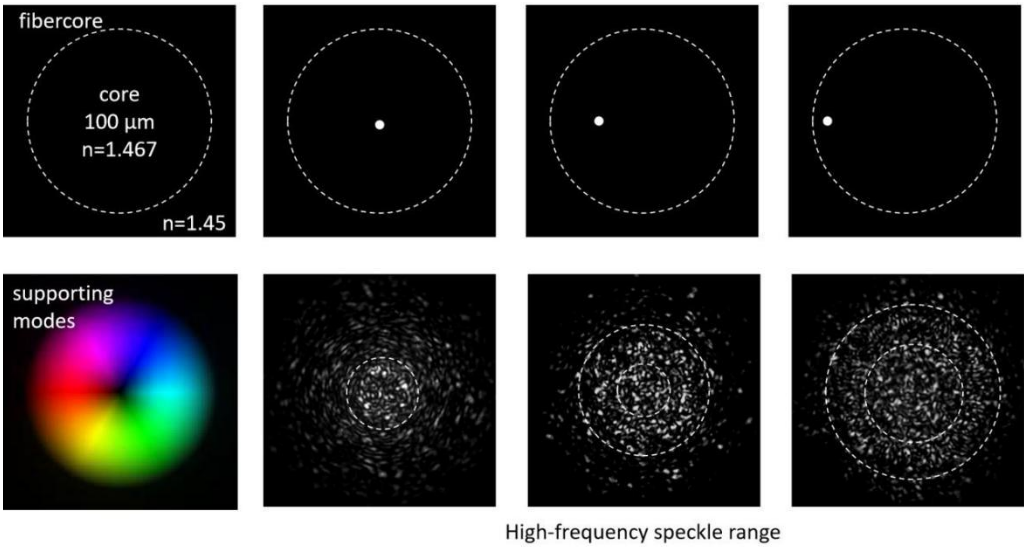

Figure 4-5. Fiber Scanning Position and Corresponding Output Speckle Pattern.

During near-end scanning of the fiber, the output speckle pattern exhibits a structured distribution. As the focal spot distance from the fiber core center changes, the distribution of high-frequency speckle regions correspondingly shifts. These output speckles represent the intensity distribution of the optical field E_{out}. The higher the spatial frequency of the speckles, the smaller the average speckle size, and the higher the achievable resolution when using them as an orthogonal basis for output optical field modulation. Therefore, to modulate the optical field at a specific output position, it is necessary to control the speckle density and frequency in the selected region when choosing the orthogonal basis. This corresponds to selecting an appropriate scanning region in the input optical field.

Our strategy involves first scanning a designated region to obtain the corresponding output optical field for each input. In theory, based on the calculated number of fiber modes, this scanning process results in oversampling. To optimize the basis selection, I apply QR decomposition to extract a subset of optical fields with the highest orthogonality, forming an orthogonal TM.

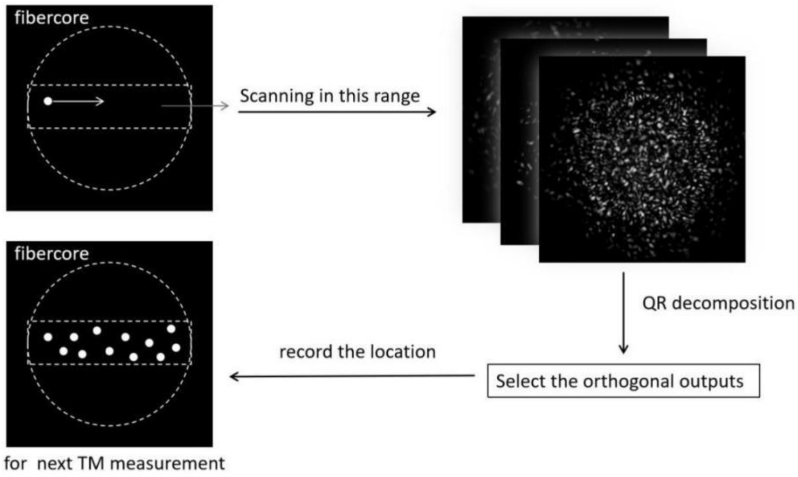

Figure 4-6. Orthogonalized transfer matrix Obtained via QR Decomposition.

The left image represents the measured TM, while the right image shows the modulus of the product of TM and its conjugate transpose. The right-side result demonstrates that after our optimization process, the transfer matrix approaches orthogonality, as indicated by the uniformity and reduced off-diagonal components. This confirms the effectiveness of our calibration, leading to improved light field control and more accurate wavefront reconstruction.

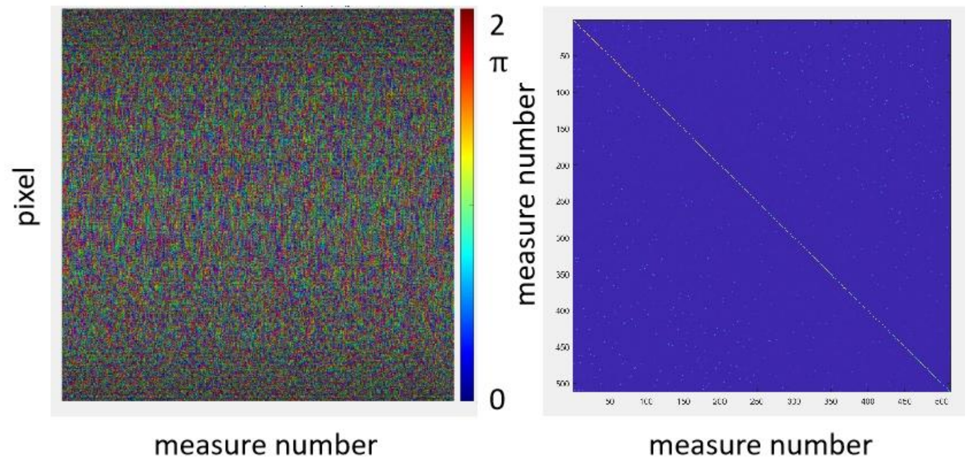

Figure 4-7. Orthogonalized Transfer Matrix Obtained via QR Decomposition.

4.2.3 The Contradiction Between Actual Measurements and Theory.

In practical operations, I encountered an issue that has been troubling me, and so far I haven't found a reasonable explanation. When measuring the transfer matrix, I serialized the input complex amplitude into an identity matrix, meaning that I performed point scanning at the near end of the optical fiber using an SLM. The complex amplitude measured at the output should correspond to the forward transfer matrix. In theory, when calculating the input complex amplitude required to produce a desired output, one should perform an inverse operation on the measured transfer matrix, using methods such as SVD algorithm.

However, what I found in practice is that taking the conjugate transpose of the measured transfer matrix (if the negative grade is applied during holographic phase extraction, the conjugate transpose is not necessary) yields a matrix that can be used directly as the inverse, and it produces even better results. In cases where the columns of the transfer matrix I selected are non-orthogonal, the computed inverse matrix fails to produce the correct phase, as shown in the ***Figure 4-8***. This result, confirmed through repeated verification, can only indicate that the transfer matrix I measured is actually the conjugate transpose of the inverse matrix. Yet, I currently cannot find a reasonable explanation for this conclusion.

Of course, this result not only does not affect the calculations but actually simplifies the process, as it eliminates the need to compute the inverse matrix when dealing with large-scale transmission matrices, greatly enhancing computational efficiency. All subsequent optical field modulations in my results are implemented using the conjugate transpose method. I hope that in the future I can find an explanation that resolves these doubts.

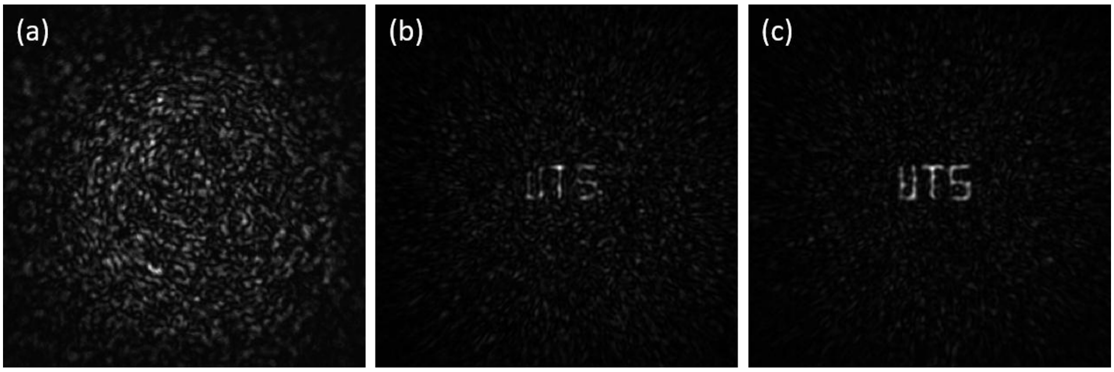

Figure 4-8. (a) The output light field obtained via the inverse matrix when the transmission matrix is non-orthogonal. (b) The output light field obtained using the inverse matrix when the transmission matrix is nearly orthogonal. (c) The output light field obtained using the conjugate transpose.

4.2.4 Output Beam Modulation

4.2.4.1 SLM Phase Calculation

After measuring the TM, and given the desired output optical field E_out, the required input field E_in can be computed using Equation 1. This involves calculating the inverse of TM. Due to the orthogonality of the optimized TM, I can simply use its conjugate transpose (Hermitian transpose) as its inverse.

Once E_{in} is obtained, it is a complex amplitude distribution located at the fiber input facet, which corresponds to the scanning plane used during the measurement process. When selecting orthogonal modes for the measurement matrix, I have already recorded the positions of the scanning spots. The computed complex amplitude matrix E_{in} with size N×1 has each element corresponding to these positions. By assigning these values to their respective positions, I obtain the required input complex amplitude plane. Finally, applying the inverse Fourier transform yields the desired complex amplitude distribution on the SLM plane.

Following the method introduced in Section 1.2.3, the complex amplitude is converted into a phase-only hologram and encoded onto the SLM. This process ensures that the target optical field is reconstructed at the output end of the MMF.

4.2.4.2 Z-Axis Optical Field Interference Modulation

In our optical system, the Spatial Light Modulator (SLM) is located in the Fourier plane relative to the proximal end of the multimode fiber (MMF). This means that the modulation applied on the SLM corresponds to spatial frequency filtering of the input field.

The SLM does not directly modulate the spatial field but rather modulates its spatial frequency content due to its placement in the Fourier plane. The relationship between the input optical field $E_{SLM}(x, y)$ and the optical field at the proximal fiber entrance $E_{in}(x, y)$ is given by a Fourier transform:

$$E_{\mathrm{in}}(x, y) = \mathcal{F}\{E_{\mathrm{SLM}}(x', y')\} \tag{3-12}$$

Where $\mathcal{F}$ denotes the Fourier transform.

By applying a ring-shaped mask on the SLM, We are effectively selecting a specific band of spatial frequencies (high spatial frequency components) while suppressing the low-frequency components typically found in Gaussian beams. This ensures that only annular wave components enter the multimode fiber.

While the transverse wavevector components (k_x, k_y) of different modes are affected by mode scrambling and modal dispersion inside the fiber, the longitudinal wavevector component k_z remains approximately preserved under paraxial conditions. This means that the energy carried by selected annular spatial frequencies is transmitted without severe phase distortion.

By applying an annular mask, I enforce a specific distribution of transverse spatial frequencies such that:

$$k_x^2 + k_y^2 = k^2 - k_z^2 \tag{3-13}$$

Where $k_x^2 + k_y^2$ is the radial wavevector component within the transverse plane. Since the fiber mainly perturbs $k_x^2$and k_y^2while keeping $k_z$relatively stable, the structured input field preferentially excites modes that maintain an axially symmetric wavefront at the fiber output. This results in the emergence of a Bessel-like beam at the distal tip, characterized by the well-known zero-order Bessel function of the first kind:

$$E_{Bessel}(r, z) \propto J_0(\sqrt{k_x^2 + k_y^2} \cdot r)e^{ik_z z} \tag{3-14}$$

Where:

J_0 is the zeroth-order Bessel function,

r is the radial coordinate,

k_z determines the axial propagation.

This Bessel beam maintains a non-diffracting property over short propagation distances, making it useful for applications such as light-sheet illumination, optical trapping, and high-resolution imaging.

4.3 System Setup

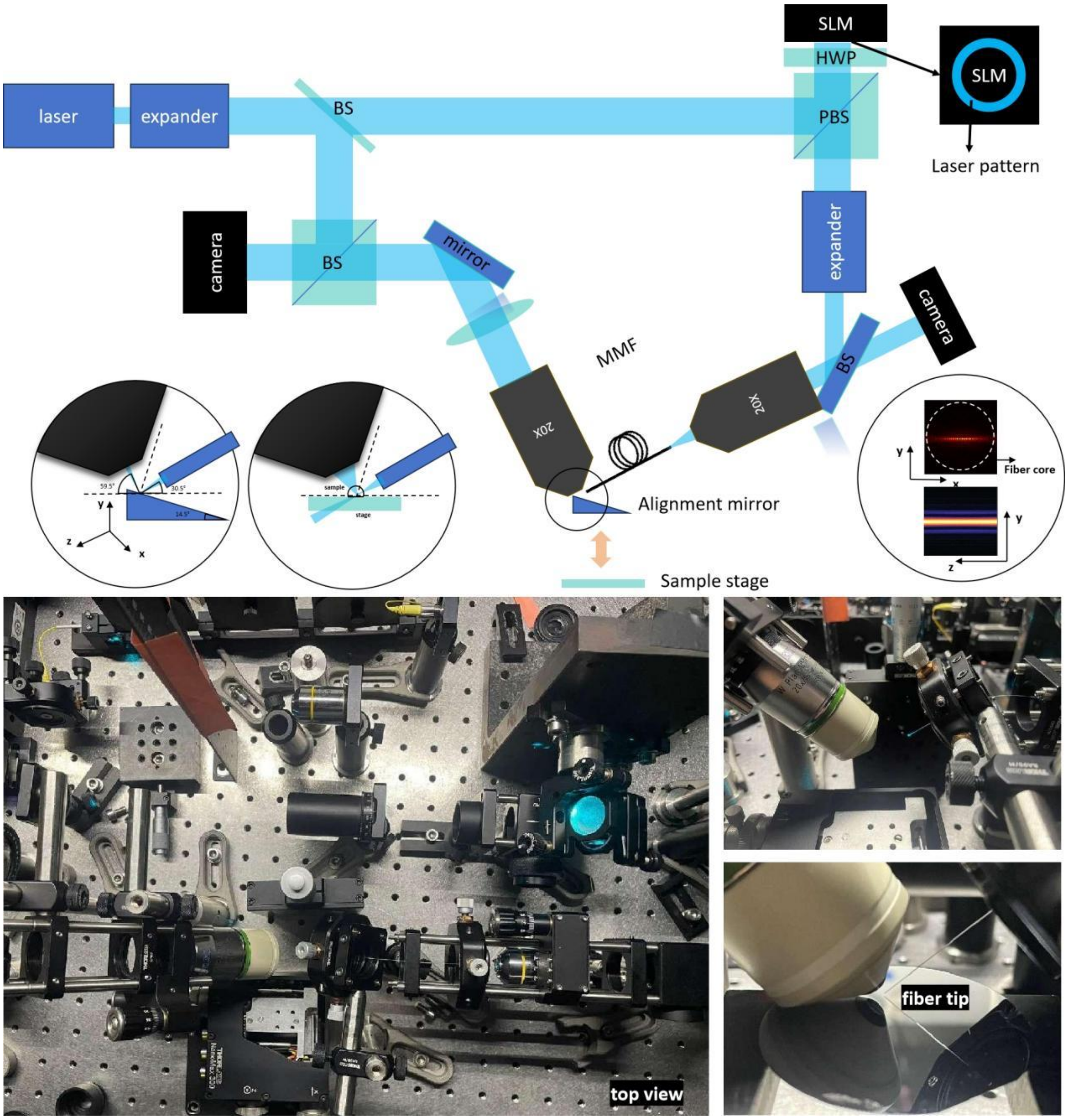

Figure 4-9. Optical path diagram of the system(up) and the actual system(down).

The optical system shown in Figure 4-9 is designed for structured light illumination and MMF imaging. The setup consists of a laser source that is expanded and directed through a beam splitter (BS) towards a spatial light modulator (SLM). A half-wave plate (HWP) and a PBS are used to control polarization before the laser pattern is projected onto the SLM. The modulated light is then expanded and directed towards the MMF via a mirror system, where the light is coupled into the fiber.

I positioned the fiber light-sheet system vertically to facilitate sample scanning, with the fiber inclined at a 30-degree angle to the horizontal plane and the imaging objective perpendicular to the fiber. This configuration helps prevent reflected light from entering the imaging system during actual imaging. When measuring the transfer matrix, I placed a 15-degree reflective mirror on the sample stage to capture the fiber's output optical field, allowing us to measure the output complex amplitude.

4.4 Result

4.4.1 Modulation of Polarization

The transmission modes of an optical fiber are influenced by polarization. However, since an SLM can only modulate a single linear polarization component, I used a phase superposition method to modulate two beams simultaneously.

To achieve this, I first converted one of the two first-order diffracted beams into an orthogonal polarization state using a half-wave plate (HWP). The two beams were then combined using a polarizing beam splitter (PBS), resulting in the superposition of two orthogonal polarization states.

When measuring the transfer matrix, I first superimposed two orthogonal gratings with diffraction directions at +45° and -45°. Each grating was then scanned separately to obtain the transmission matrices for the two polarization states.

To generate the desired target light field, I computed the required input phase using both transmission matrices. Finally, by superimposing the phase modulations of the two polarization states, I achieved full-polarization modulation.

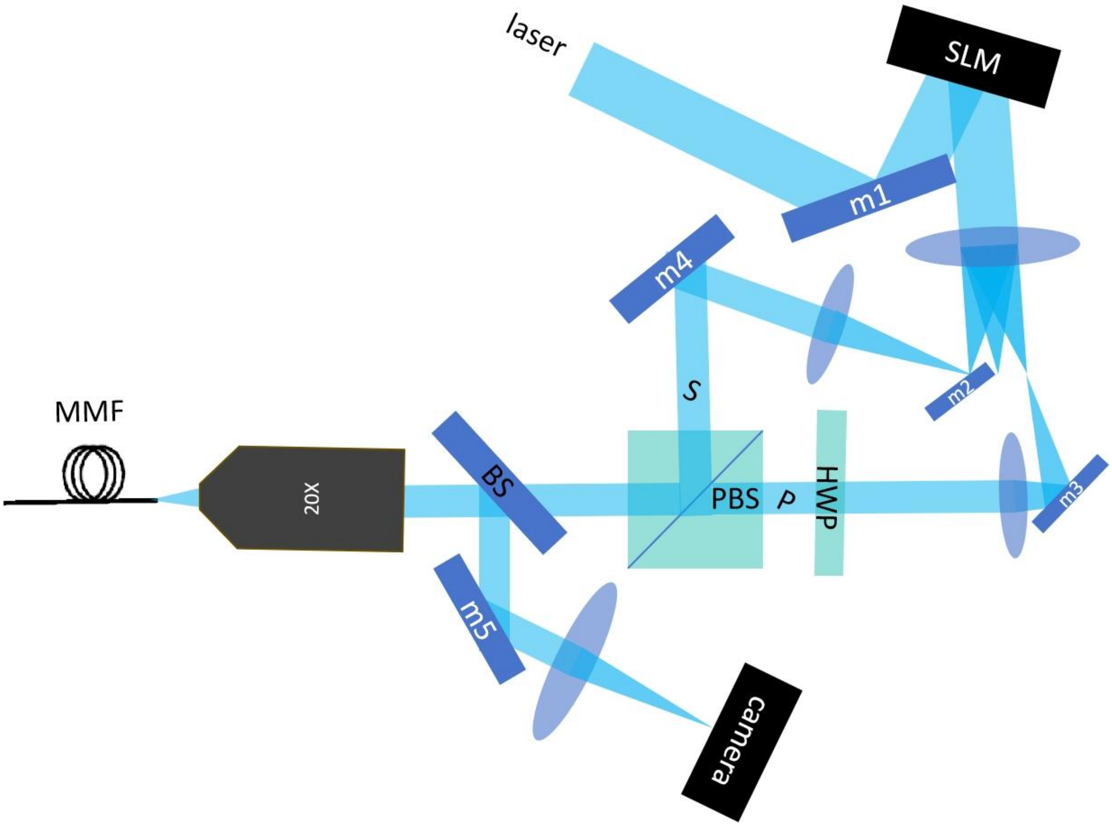

Figure 4-10. Methods of modulating both S and P polarization using SLM.

Figure 4-11. Left, middle, and right correspond to the output patterns at the fiber distal facet when modulating only S-polarized light, only P-polarized light, and both S and P-polarized light simultaneously, respectively.

As shown in ***Figure 4-11***, modulating only S-polarized or P-polarized light results in incomplete modulation in certain regions. This occurs due to interference between modes when a single polarization state is used as input. By modulating both S and P polarization simultaneously, the output modes complement each other in intensity, enabling the reconstruction of a complete target light field. The result of modulated Bessel beam array by S and P polarization is as shown in ***Figure 4-12***.

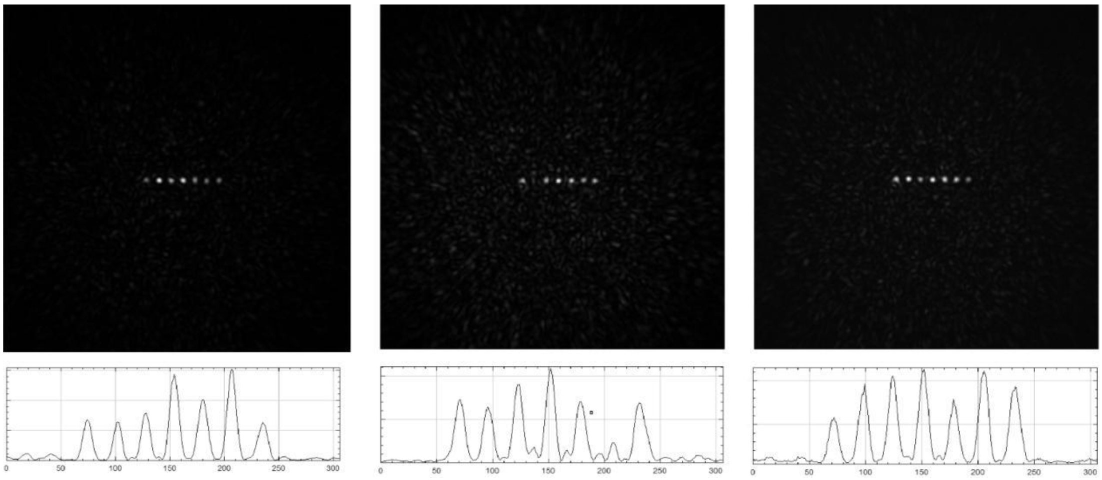

Figure 4-12.The effect of polarization state modulation on the output of multi-point Bessel light sheets.

4.4.2 Modulation of Gaussian and Bessel Optical Fields

The results presented in the Figure 4-13 compare the focusing performance of two different phase modulations applied to the SLM. On the left, a standard phase modulation is used, resulting in a focal spot with a full-width at half maximum (FWHM) of 1.81 µm. On the right, an additional annular phase mask is introduced, effectively filtering the spatial frequencies of the input light field. This leads to a tighter focal spot with an improved FWHM of 1.17 µm, indicating an enhanced focusing capability. The annular phase mask contributes to a sharper and more confined focal region, demonstrating its effectiveness in improving resolution by suppressing undesired low-frequency components in the optical field.

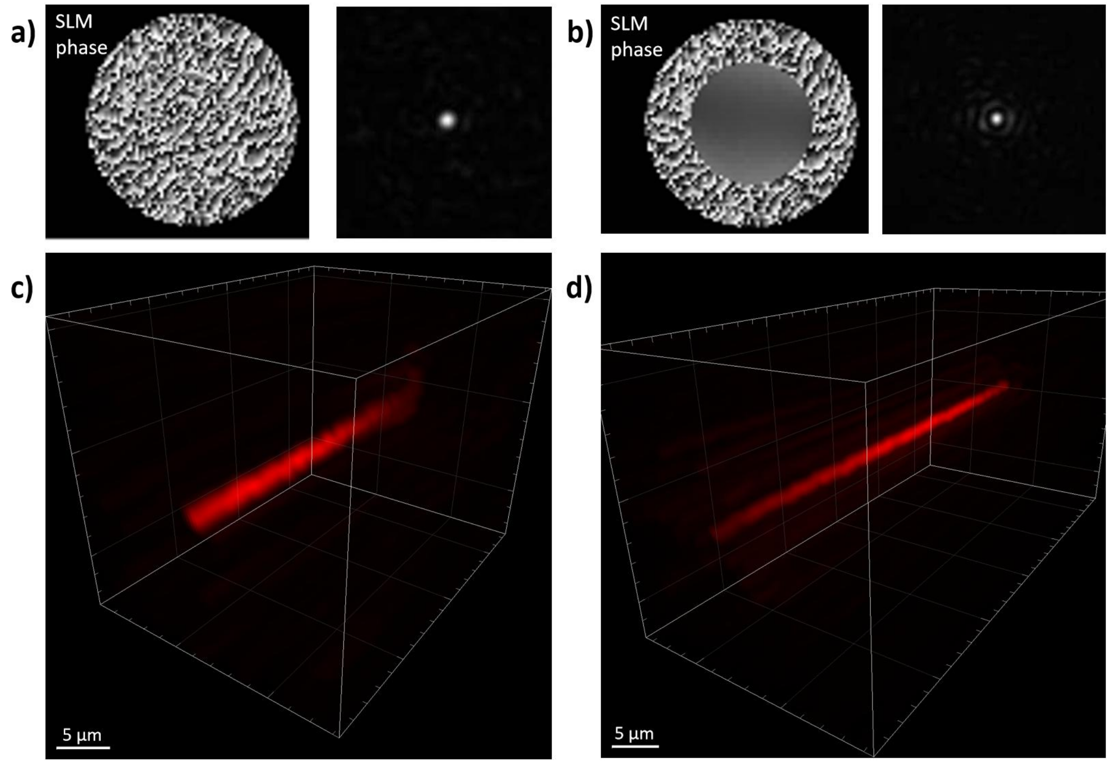

Figure 4-13. A comparison between the modulation of a Gaussian optical field and a Bessel beam using an SLM.

As shown in ***Figure 4-13*** a), a Gaussian beam is generated by applying a phase modulation pattern on the SLM, producing a focused spot with a full width at half maximum (FWHM) of 1.81 µm, as shown in the intensity profile. The corresponding 3D visualization in c) illustrates the beam propagation, where the focal region is localized with a rapid intensity drop-off along the axial direction.

In contrast, b) demonstrates the transformation of the beam into a Bessel-like optical field by applying a ring-shaped phase mask on the SLM. The resulting beam exhibits a narrower central peak with an FWHM of 1.17 µm, as shown in the intensity profile. The 3D visualization in d) highlights the extended propagation length of the beam, characteristic of Bessel beams, which maintain their central intensity over a longer distance compared to the Gaussian beam.

These results confirm that applying a ring-shaped mask to the SLM effectively modulates the output beam, improving the focal confinement and extending the propagation range, which is beneficial for applications requiring enhanced axial resolution and long-range beam propagation.

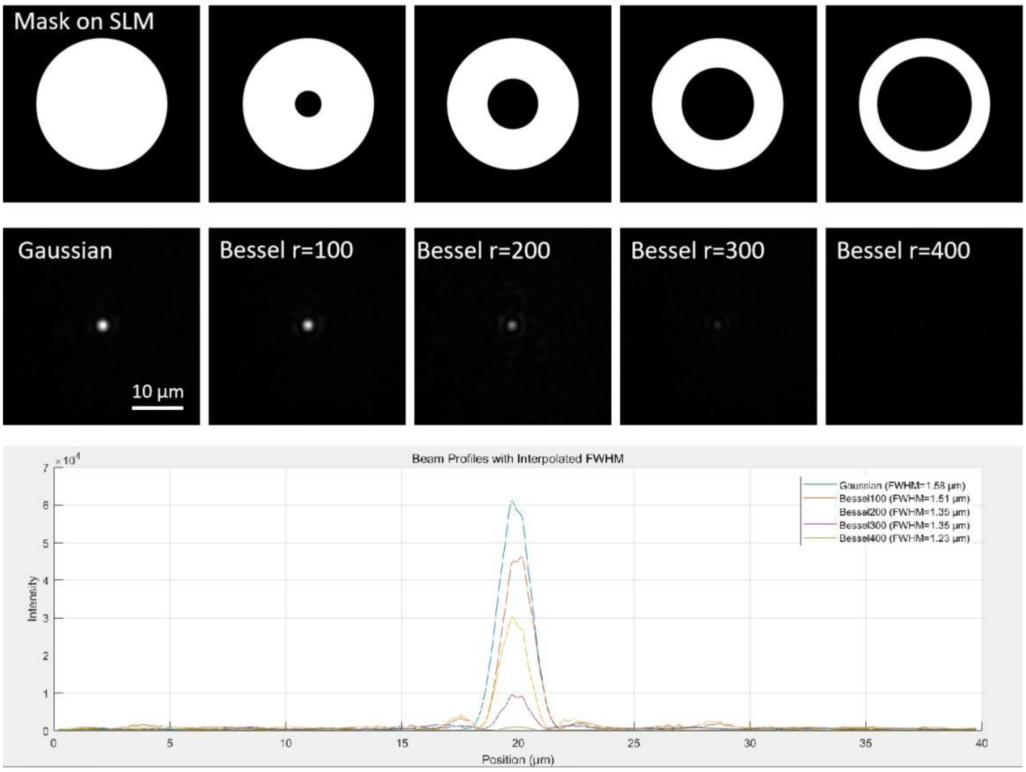

Figure 4-14. Bessel light field variation with changing masks.

In ***Figure 4-14*****,** the first row displays the SLM-applied masks used to generate different beam profiles at the fiber output. The leftmost image represents a fully open aperture, producing a Gaussian beam, while the other images show annular masks with inner radii of 100, 200, 300, and 400 pixels, designed to generate Bessel-like beams.

The second row presents the corresponding beam intensity distributions at the fiber output, revealing that the Gaussian beam produces a single diffraction-limited spot, whereas the Bessel beams exhibit a central peak with concentric rings, characteristic of non-diffracting beams.

The bottom graph shows the cross-sectional intensity profiles, highlighting that as the mask radius increases, the central peak narrows. The Gaussian beam has the widest FWHM (1.68 µm), while the Bessel400 configuration achieves the smallest FWHM (1.23 µm). These results confirm that annular masks effectively modify beam profiles, enhancing lateral resolution for precision optical applications.

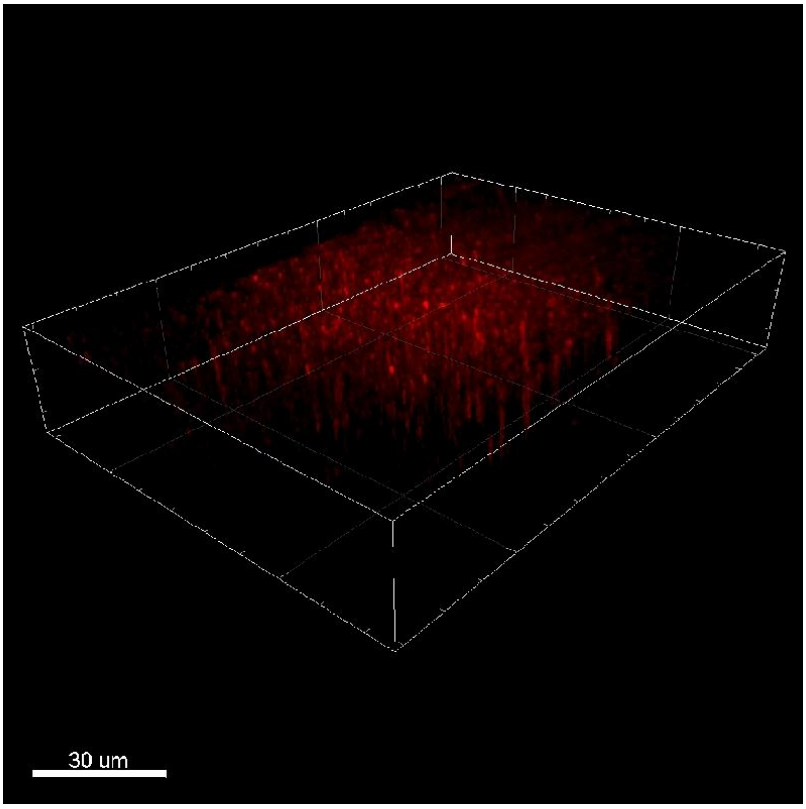

Figure 4-15. Result of Bessel light-sheet scanning fluorescence nanobeads.

Figure 4-15 shows the results of Bessel light-sheet scanning fluorescence nanobeads. The system used a 488 nm excitation laser, and fluorescence emission was collected through a 500 long-pass filter, capturing signals around 510 nm. The structured illumination provided by the Bessel beam enabled high-contrast imaging of the nanobeads, enhancing axial resolution while maintaining a thin illumination profile. This approach effectively reduced out-of-focus background fluorescence, allowing for improved signal clarity and depth penetration in fluorescence imaging.

4.4.3 Modulation of Bessel Beam Array

The modulation method for generating a Bessel beam array using fiber-optic light field control involves a two-step phase modulation process. First, after measuring the transfer matrix (TM) of the multimode fiber, the target output field is set as an array of discrete focal spots. This configuration initially produces a Gaussian beam array at the fiber output, effectively forming a structured light-sheet pattern. Next, by applying an annular mask on the spatial light modulator (SLM), each Gaussian spot is transformed into a Bessel beam, resulting in a Bessel beam array light-sheet. The spacing between the Bessel beams is optimized to match the full-width of a single beam, allowing for complete sample coverage in three-step lateral displacements. This structured approach significantly accelerates the scanning process by reducing the required number of sequential illuminations while preserving the high axial resolution and extended depth of field advantages of Bessel beam-based imaging.

A sequence of Bessel beams is displayed to take advantage of their unique propagation characteristics, particularly their non-diffracting and self-healing nature. Unlike Gaussian beams, which quickly diverge and lose intensity away from the focal plane, Bessel beams maintain a narrow central core over an extended axial distance, effectively creating a non-diffracting light sheet. This allows for illumination of a larger scanning region without compromising axial resolution. By sequentially displaying or scanning Bessel beams across the sample, one can achieve more uniform excitation, enhanced penetration depth, and reduced shadowing artifacts. This improves imaging performance, especially in thick or scattering specimens, where conventional Gaussian light sheets may fail to provide sufficient coverage or resolution.

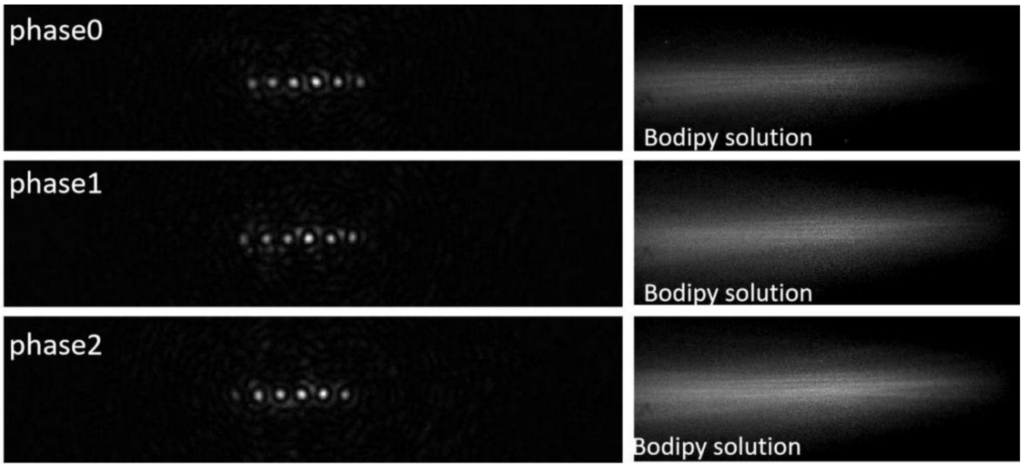

Figure 4-16. Bessel Beam Array Modulation on Fiber Tip.

Figure 4-16 illustrates the modulation of a Bessel beam array at the output of a multimode fiber. The left column shows the structured illumination at the fiber tip, where discrete focal spots are generated and phase-shifted across three steps (Phase 0, Phase 1, Phase 2). These phase shifts correspond to lateral displacements of the array, enabling full light-sheet coverage. The right column presents the corresponding fluorescence excitation in a BODIPY solution(BODIPY is a fluorescent dye known for its high photostability, sharp emission peaks, and versatility in biological imaging.), demonstrating the extended and uniform illumination achieved through Bessel beam-based structured light. The results confirm the successful generation of a tunable Bessel beam array using fiber-optic light field modulation, allowing for fast and efficient scanning in light-sheet fluorescence microscopy.

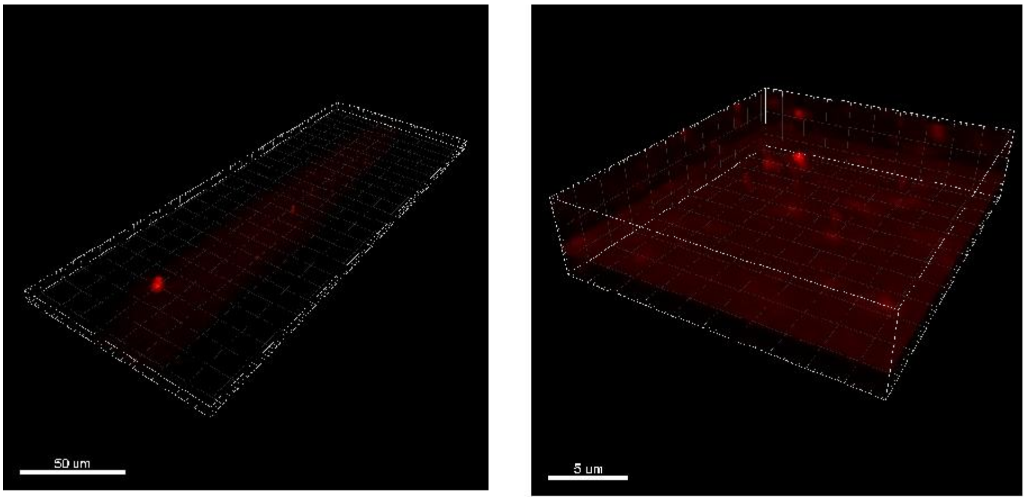

Figure 4-17. Result of Fluorescence Nanobeads Scanning by Bessel Beam Array.

Figure 4-17 presents the fluorescence imaging results of nanobeads scanned using a Bessel beam array. The left panel shows an extended illumination pattern, demonstrating the long-range propagation and uniform excitation of the Bessel beam. The right panel provides a high-resolution 3D reconstruction of the fluorescence nanobeads, highlighting their spatial distribution within the sample. The structured light pattern ensures effective excitation over a wide field of view, confirming the successful modulation and scanning capability of the Bessel beam array.

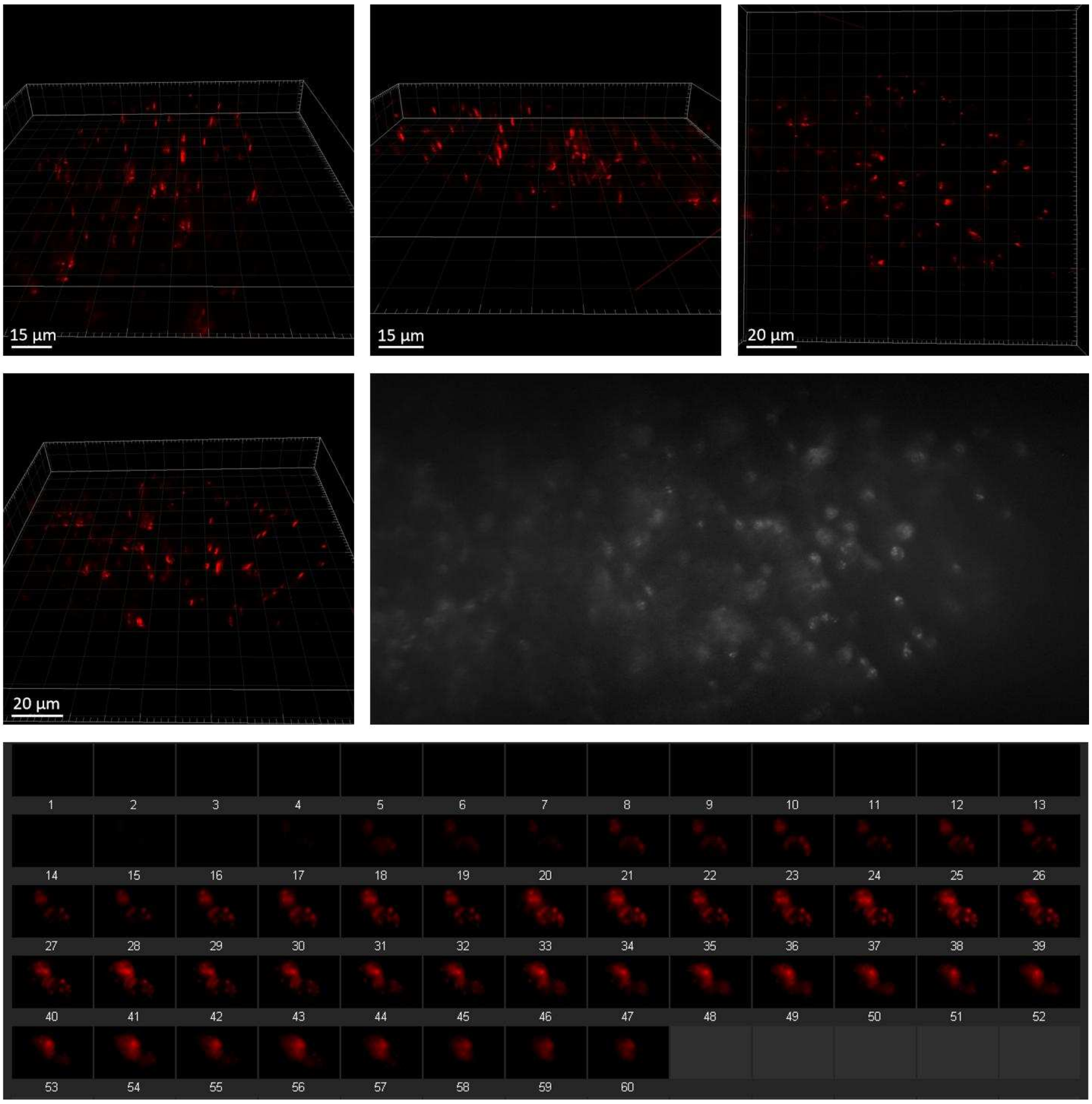

Figure 4-18. The 3D reconstruction results of yeast cells embedded in agarose, obtained through light-sheet scanning at the fiber tip.

Figure 4-18 shows the results of three-dimensional scanning of yeast cells using a fiber-based Bessel light sheet. The yeast cells were stained with BODIPY, fixed in agarose, and scanned for imaging using a translation stage.

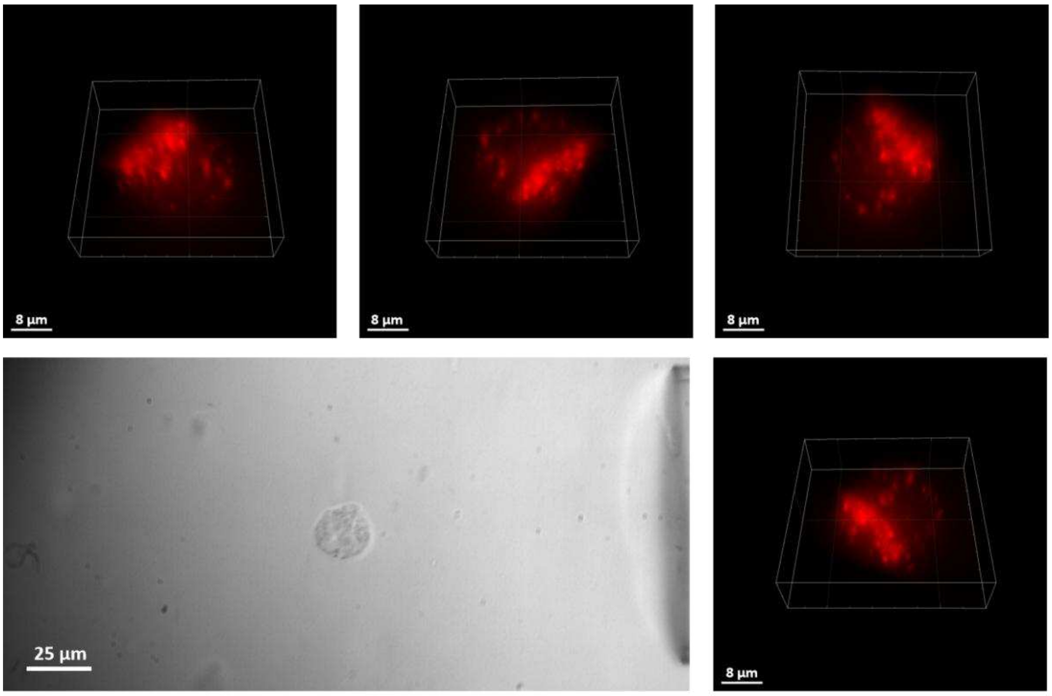

Figure 4-19. The light-sheet scanning results of a single AC-16 cell obtained through the fiber tip.

Figure 4-19 shows the three-dimensional scanning results of AC16 cells using a fiber-based Bessel light sheet.

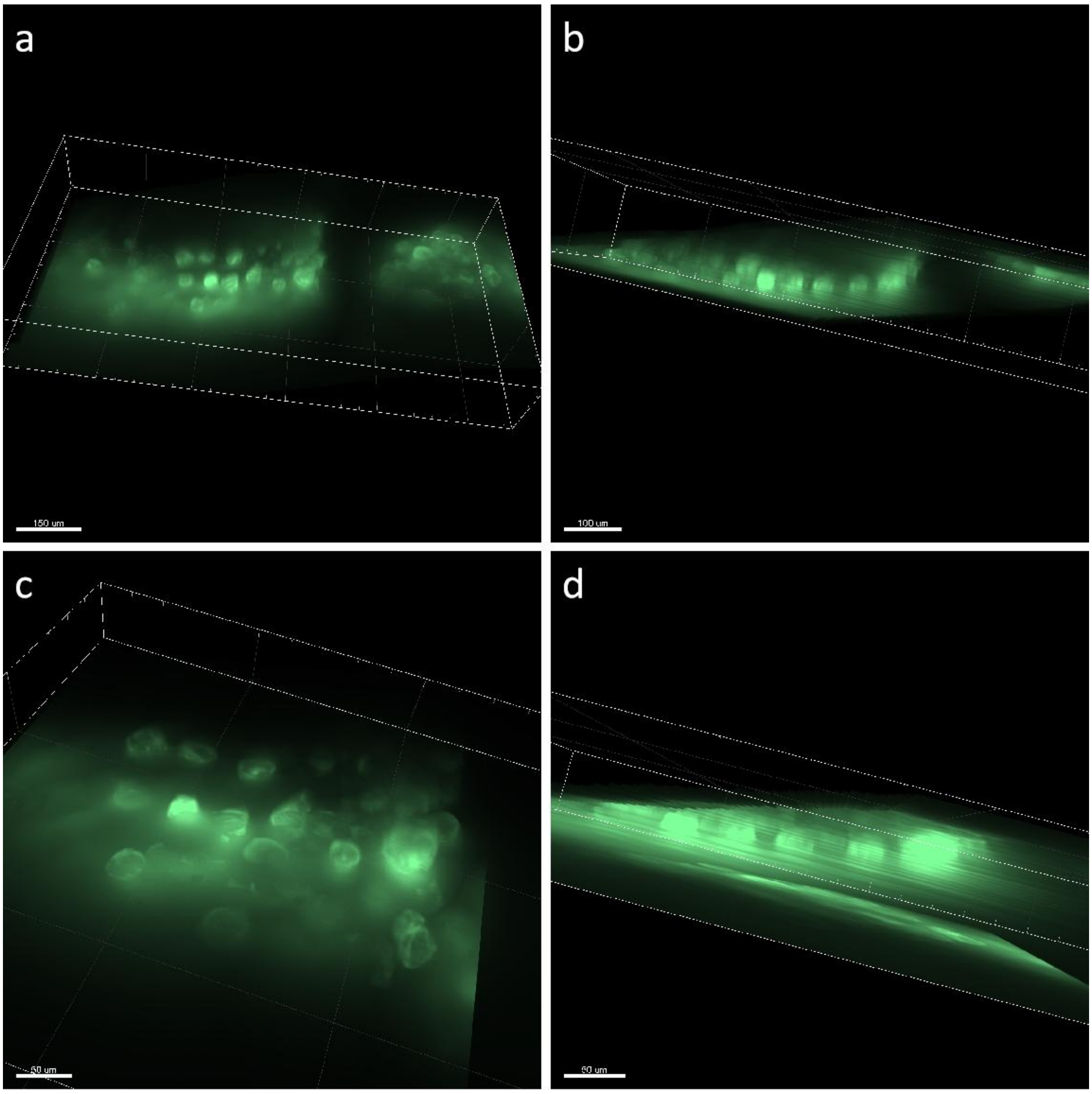

Figure 4-20 The figure shows the scanning results of organoids using a fiber-based Bessel light sheet. (a) Full-field, top view; (b) Full-field, side view; (c) Local top view; (d) Local side view.

In the fiber-based light-sheet scanning approach, the achievable resolution is determined by both the excitation characteristics and the detection configuration. Laterally, the resolution is governed by the diffraction limit of the detection objective under widefield fluorescence conditions. For 488 nm excitation, assuming a high-NA detection objective, the lateral resolution typically reaches ~250 nm. Axially, however, the resolution is constrained by the thickness of the light sheet itself. In our implementation, the light sheet is generated by scanning a Bessel beam through the sample. The central lobe of the Bessel beam determines the effective light-sheet thickness, which is approximately 1.35 µm in our case. This thinner axial profile enables improved sectioning compared to conventional Gaussian beams, which tend to diverge more rapidly and generate thicker sheets. However, the presence of side lobes in the Bessel beam may contribute to background excitation and reduced contrast, which must be managed through post-processing or two-photon excitation strategies.

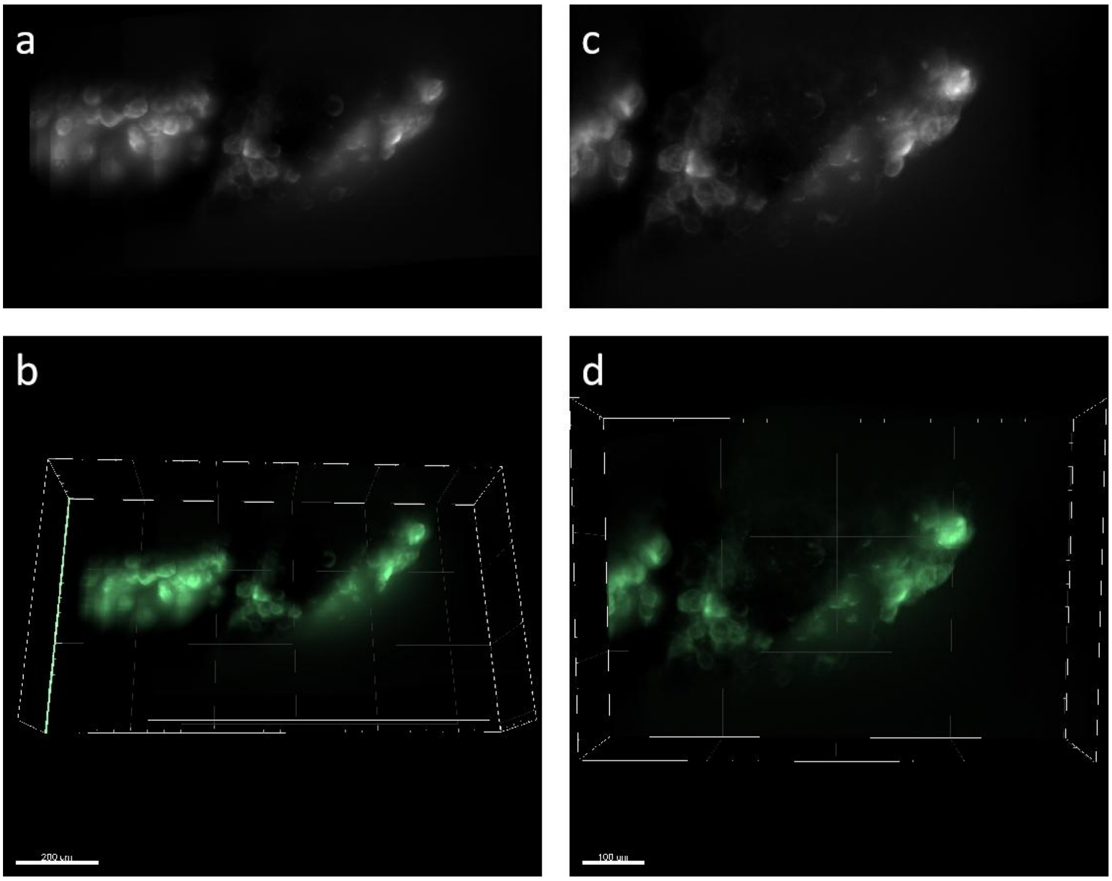

Figure 4-21.Localized 3D scanning reconstruction results of organoids: (a) Single-objective light sheet, z projection; (b) Single-objective light sheet, 3D reconstruction top view; (c) Fiber-based Bessel light sheet scanning result, z projection; (d) Fiber-based Bessel light sheet, 3D reconstruction top view.

4.5 Conclusion and Thoughts

Throughout this work, I have presented an integrated strategy for merging free-space light field modulation techniques with the spatial constraints of single MMF imaging, particularly in light-sheet microscopy. By measuring and utilizing the transmission matrix (TM) of a multimode fiber (MMF), We demonstrated the ability to generate diverse beam profiles—from Gaussian spots to Bessel arrays—using only a spatial light modulator (SLM) for both calibration and wavefront shaping. This setup simplifies the system, accelerates calibration via single-shot off-axis holography, and exploits orthogonal scanning patterns to improve resolution and reduce cross-talk.

More importantly, I employed a method to obtain the inverse transfer matrix without the need for direct matrix inversion. This approach significantly reduces computational costs, allowing more resources to be allocated for light field reconstruction. It holds great potential for applications in various holography algorithms, enhancing efficiency and scalability.

Next, I will discuss the limitations and challenges of the current single-fiber modulated light field.

4.5.1 Limited Numerical Aperture (NA)

Standard MMFs typically have a smaller NA than high-NA free-space objectives, meaning the focal spot at the fiber output cannot be made arbitrarily tight. Consequently, the achievable lateral resolution is reduced, which can be a limiting factor in high-resolution applications.

4.5.2 Fiber Deformation and Stability

Bending or twisting the fiber does not significantly alter the internal modes themselves; rather, it changes the coupling between modes, leading to variations in the effective transmission matrix. As a result, the initially measured transfer matrix may become invalid. To counteract this, frequent recalibrations or real-time correction algorithms are required, potentially increasing system complexity. Machine learning methods or robust phase-drift compensation strategies may offer practical solutions to address these coupling-induced instabilities in future designs.

4.5.3 Generation of Complex Interference Light Field

Lattice light-sheet microscopy relies on forming interference patterns using multiple k-vector components in both radial and axial directions, which provides excellent optical sectioning and reduced photobleaching. However, in a single MMF system, the 'k-space' is fundamentally constrained because only the axial wave vector (kz) is largely preserved in propagation. Achieving the multidirectional interference patterns required for true lattice beams would demand broader control over k-space than TM allow.

4.5.3.1 Potential Solutions and Outlook

Enhanced Fiber Designs: Combining the fiber with high NA optics like metasurface. While it does not increase the number of modes supported by the fiber, it enables tighter focusing, leading to enhanced axial resolution.

Adaptive Algorithms: Implementing real-time wavefront shaping that continuously updates to account for fiber perturbations may maintain stability without the need for extensive recalibration.

Hybrid Approaches: Partial free-space beam shaping prior to fiber coupling or coherent fiber bundles might open pathways to more complex multi-k vector illumination schemes, bringing lattice or other advanced structured beams closer to feasibility.

Overall, the convergence of MMF-based light-field modulation and light-sheet microscopy marks a significant step toward more compact, high-speed, and minimally invasive imaging systems. As new fiber technologies and computational methods continue to evolve, I anticipate further progress in achieving high-resolution, customizable beam patterns, potentially including lattice beams, in highly constrained environments. This will extend the utility of fiber-delivered light-sheet illumination into a broader range of biomedical and industrial applications, enabling more flexible, scalable, and efficient imaging strategies.

4.6 Reference

1. Pan, M., et al., *Dielectric metalens for miniaturized imaging systems: progress and challenges.* Light: Science & Applications, 2022. **11**(1): p. 195.
2. Zhou, P., et al., *A review of optical imaging technologies for microfluidics.* Micromachines, 2022. **13**(2): p. 274.
3. Shaker, L.M., et al., *Integrated photonics: bridging the gap between optics and electronics for enhancing information processing.* Journal of Optics, 2023: p. 1-13.
4. Paiè, P., et al., *Microfluidic based optical microscopes on chip.* Cytometry Part A, 2018. **93**(10): p. 987-996.
5. Luo, W., et al., *Synthetic aperture-based on-chip microscopy.* Light: Science & Applications, 2015. **4**(3): p. e261-e261.
6. Zheng, G., et al., *Sub-pixel resolving optofluidic microscope for on-chip cell imaging.* Lab on a Chip, 2010. **10**(22): p. 3125-3129.
7. Greenbaum, A., et al., *Imaging without lenses: achievements and remaining challenges of wide-field on-chip microscopy.* Nature methods, 2012. **9**(9): p. 889-895.
8. Heng, X., et al., *Optofluidic microscopy—a method for implementing a high resolution optical microscope on a chip.* Lab on a Chip, 2006. **6**(10): p. 1274-1276.
9. Wen, Z., et al., *Single multimode fibre for in vivo light-field-encoded endoscopic imaging.* Nature Photonics, 2023. **17**(8): p. 679-687.
10. Yu, H., et al., *All-optical image transportation through a multimode fibre using a miniaturized diffractive neural network on the distal facet.* Nature Photonics, 2025: p. 1-8.
11. Plöschner, M., et al., *Multimode fibre: Light-sheet microscopy at the tip of a needle.* Scientific reports, 2015. **5**(1): p. 18050.

5 Summary and Outlook

This thesis systematically investigates the critical role of light field modulation and illumination strategies in multi-scale imaging. It begins with a comprehensive review of the fundamental theories and methods for controlling light, including spatial, temporal, spectral, and polarization dimensions, and then details advanced techniques such as structured illumination, light-sheet microscopy, and holographic imaging. These approaches collectively break through conventional imaging limits to achieve high contrast, high resolution, and high speed volumetric imaging.

The experimental chapters demonstrate Application of Orthogonal Light-Sheet Illumination Methods in Volumetric Imaging at Different Scales and Modalities. In particular, the work presents:

First, to address the challenge of obtaining three-dimensional vascular structures with a large field of view in small-animal imaging despite high background noise, this dissertation proposes an orthogonal illumination system. This system integrates light-sheet illumination with time gating to reduce background interference, and deep learning methods are employed to enhance the vascular signal-to-noise ratio. Using this approach, I reconstructed the three-dimensional vascular network of a mouse over a large field of view, clearly demonstrating the spatial relationships between superficial blood vessels, the intestine, and other internal structures. This provides a novel imaging approach for in Vivo research.

Second, to achieve label-free three-dimensional scattering imaging at both the organoid and single-cell scales, this thesis proposes a strategy that employs rotational light-sheet illumination to extend ROCS into 3D volumetric imaging. By implementing two feasible approaches for rotating light-sheet illumination, the conventional TIRF framework is replaced with an orthogonal light-sheet illumination mode. This enables the capture of three-dimensional scattering distributions of organoids and cells. Experimental results confirm the feasibility of this method for label-free volumetric imaging, offering a fast, low-damage three-dimensional imaging solution for studying cellular structures.

Third, to enable the miniaturization and flexible integration of optical systems, I developed a miniature light-sheet illumination system that uses a single multimode fiber. By measuring the fiber′s transmission matrix and building upon existing theories of light field modulation, this research achieves control over the light transfer modes through the fiber. The desired light field can be accurately projected at the distal end without requiring inverse matrix computations. This research is intended to provide new ideas for the future development of minimally invasive endoscopes, on-chip microscopes, and holographic imaging.

Outlook

Despite these promising advancements, several challenges remain that call for further investigation. For example, environmental fluctuations and fiber bending still affect the stability of transmission matrices in multimode fiber imaging, indicating a need for more robust, real-time adaptive correction methods. Additionally, system integration and miniaturization are essential for the practical deployment of these sophisticated optical systems in clinical or portable devices. Moreover, imaging artifacts due to scattering and absorption in complex biological samples require even more refined wavefront correction and advanced deep learning algorithms.

Light-Sheet Modulation for In Vivo Imaging of Small Animals

Future work in this area should focus on further enhancing in vivo imaging performance by optimizing light-sheet properties. Key directions include improving light-sheet uniformity and thickness to boost axial resolution and penetration depth while keeping phototoxicity to a minimum. Integrating adaptive optics and multi-angle illumination strategies can help correct tissue-induced aberrations and compensate for motion artifacts inherent to live animal imaging. Additionally, real-time processing and advanced reconstruction algorithms are needed to support high-speed, volumetric imaging for dynamic biological studies.

Rotational Light-Sheet Modulation for Scattering Imaging

One of the biggest challenges in scattering imaging today is determining the structural information conveyed by the scattering field. In the future, using thinner light sheets may help suppress coherent noise to some extent; however, even with TIRF-ROCS, not all scattering signals can be fully explained. Currently, we can only assess them via fluorescence colocalization. Yet, I believe that the scattering field offers more structural information that most of which is difficult to correlate with fluorescence. This calls for future breakthroughs in algorithms that can reconstruct more structural details based on the physical characteristics of scattering signals.

In organoid research, I believe that near-infrared lasers can be applied to scattering and label-free imaging. This approach not only addresses the limitations of NIR-II dyes but also takes advantage of the deep penetration of near-infrared light to enable microscopic imaging of large-scale samples.

Light Field Encoded Fiber Illumination

For fiber-based imaging systems, future research should aim to improve both the design of the fibers and the robustness of the encoding schemes. Developing fibers with enhanced numerical aperture and transmission stability is essential to mitigate issues such as modal dispersion and fiber bending. Coupling these improvements with real-time adaptive wavefront shaping techniques, including phase conjugation and iterative phase optimization, will help stabilize the transfer matrix. Moreover, leveraging machine learning for adaptive correction can further enhance image quality, thereby extending the applicability of fiber-based systems in minimally invasive endoscopic diagnostics.

6 Support Information

6.1 Matlab Code

6.1.1 vessel_enhance

```
function I5 = vessel_enhance(I1)
% VESSEL_ENHANCE Enhances vessel-like structures in an image.
%    I5 = VESSEL_ENHANCE(I1) processes the input image I1 by analyzing local
%    intensity variations along four directions (diagonals, horizontal, and
%    vertical) within a window. The output I5 is a binary image indicating
%    potential vessel locations.

% Normalize the input image to the range [0, 255]
I1 = double(I1);
I1 = I1 / max(I1(:)) * 255;

% Define window size and half-window size
win = 11;
r = (win - 1) / 2;
[y, x] = size(I1);
I5 = zeros(y, x);

% Loop through each pixel in the valid region (avoid borders)
for j = r+1 : y - r
    for i = r+1 : x - r
        % Process only if the central pixel is non-zero
        if I1(j, i) > 0
            % Extract the local window centered at (j, i)
            A = I1(j-r:j+r, i-r:i+r);

            % Process the main diagonal (top-left to bottom-right)
            a1 = diag(A);
            baseline = linspace(a1(1), a1(end), win)'; % Linear interpolation between endpoints
            a1 = a1 - baseline;

            % Process the anti-diagonal (top-right to bottom-left)
            a2 = diag(fliplr(A));
            baseline = linspace(a2(1), a2(end), win)';
            a2 = a2 - baseline;

            % Process the horizontal line (center row)
```

```
            a3 = A(r+1, :)';
            baseline = linspace(a3(1), a3(end), win)';
            a3 = a3 - baseline;

            % Process the vertical line (center column)
            a4 = A(:, r+1);
            baseline = linspace(a4(1), a4(end), win)';
            a4 = a4 - baseline;

            % Check if the center element is the maximum in any direction
            if a3(r+1) == max(a3)
                I5(j, i) = 1;
            elseif a4(r+1) == max(a4)
                I5(j, i) = 1;
            elseif a1(r+1) == max(a1)
                I5(j, i) = 1;
            elseif a2(r+1) == max(a2)
                I5(j, i) = 1;
            end
        end
    end
end
end
```

6.1.2 Lee Hologram

```
% Parameter settings
Nx = 512;                  % Image width (number of pixels)
Ny = 512;                  % Image height (number of pixels)
[x, y] = meshgrid(linspace(-1, 1, Nx), linspace(-1, 1, Ny));    % Generate grid coordinates
% Define the target phase function phi(x,y)
% In this example, a spherical phase function is used.
phi = pi * (x.^2 + y.^2);
% Define the carrier frequency (in cycles per unit length)
fx = 20;     % Carrier frequency in the x-direction
fy = 20;     % Carrier frequency in the y-direction
% Generate the Lee hologram:
% Using the formula H(x,y) = 0.5 + 0.5*cos[2*pi*(fx*x + fy*y) + phi(x,y)]
H = 0.5 + 0.5 * cos(2*pi*(fx*x + fy*y) + phi);
% Binarization (threshold set to 0.5)
H_binary = H >= 0.5;
% Display the results
figure;
subplot(1,2,1);
imagesc(H);
title('Lee Hologram Amplitude Distribution');
```

```
axis image;
colormap gray;
colorbar;
subplot(1,2,2);
imagesc(H_binary);
title('Binarized Lee Hologram');
axis image;
colormap gray;
colorbar;
```

6.1.3 Generate scanning base

```
clc;
clear;

% Define center coordinates and distance thresholds
center_x = -200;
center_y = -200;
distance_threshold = 40;
distance_threshold2 = 0;

% Initialize counter and pre-allocate index matrix
k = 1;
index = zeros(5026, 2);

% Optionally load intensity rate data
% load intensity_rate.mat

% Loop through the x and y coordinates within the defined range around the center
for y = (center_y - distance_threshold) : 1 : (center_y + distance_threshold)
    for x = (center_x - distance_threshold) : 1 : (center_x + distance_threshold)

        % Calculate the Euclidean distance from the current point to the center
        distance = sqrt((x - center_x)^2 + (y - center_y)^2);

        % Check if the distance is within the specified thresholds
        if distance <= distance_threshold && distance >= distance_threshold2

            % Obtain the image pattern using a scanning function (assumed to return an image matrix)
            pattern = scan_function(x, y);
            % Optionally adjust pattern with a rate factor
            % pattern = pattern / 128 * rate(k);

            % Store the current (y, x) coordinates in the index matrix
```

```
            index(k, :) = [y, x];

            % Generate filenames for saving the images
            filename = sprintf('E:\\pattern0\\pattern_%04d.bmp', k);
            filename1 = sprintf('E:\\pattern0\\pattern_%04dinv.bmp', k);

            % Process the pattern: apply modulo operation
            pattern = mod(pattern, 255);

            % Mask the pattern outside a circle of radius 512 centered at (1920/2, 1152/2)
            for xx = 1:1920
                for yy = 1:1152
                    if ((xx - 1920/2)^2 + (yy - 1152/2)^2 < 0^2) || ((xx - 1920/2)^2 + (yy - 1152/2)^2 > 512^2)
                        pattern(yy, xx) = 0;
                    end
                end
            end

            % Optionally crop the pattern (commented out)
            % pattern = pattern(65:64+1024, 449:448+1024);

            % Save the processed pattern image
            imwrite(uint8(pattern), filename);

            % Read another pattern image from a specified path and save it with a different filename
            pattern1 = imread('C:\Users\Administrator\Desktop\pattern3\aa.bmp');
            imwrite(uint8(pattern1), filename1);

            % Display the current count
            disp(k);

            % Increment the counter
            k = k + 1;
        end

    end
end

% Save the index matrix to a MAT-file
save index.mat index
```

6.1.4 Off-axis hologram phase reconstruction

```
clear;
clc;
```

```
tic;
%% Define constants and load data
load phasedrift.mat;    % Load phase drift data

maskSize = 768;              % Size of the mask/image
radius = 40 * 2;            % Radius for circular mask
center = maskSize / 2; % Center coordinate for the mask

side = 256;    % Desired side length for resized images

%% Load and preprocess background image
bg = double(imread('E:\\sitong\\result\\bg.tif'));
bg = imresize(bg, [256, 256], "bilinear");

%% Create a circular mask (to be used once)
[xGrid, yGrid] = meshgrid(1:maskSize, 1:maskSize);
distanceFromCenter = sqrt((xGrid - center).^2 + (yGrid - center).^2);
mask = double(distanceFromCenter <= radius);

%% Initialize large complex matrix to store processed images
% Each column corresponds to one flattened complex field image.
complexMatrix = zeros(side^2, 5026);

%% Check if Parallel Computing Toolbox is available and start pool if needed
if isempty(gcp('nocreate'))
    parpool;    % Start a parallel pool if not already running
end

%% Set shift parameters for FFT manipulation
yShift = 185;
xShift = 159;

%% Pre-calculate reference phase and intensity from a baseline image
k = 1;
phaseFilename0 = sprintf('E:\\sitong\\phaseraw\\phase%05d.tif', 2);
P0 = double(imread(phaseFilename0));

% Compute FFT of the baseline image, apply shifts, and mask
II0 = fftshift(fft2(P0));
II0 = circshift(II0, yShift - round(maskSize / 2), 1);
II0 = circshift(II0, xShift - round(maskSize / 2), 2);
II0 = II0 .* mask;
phase0 = angle(ifft2(ifftshift(II0)));
intensity0 = abs(ifft2(ifftshift(II0)));

%% Process images using a loop (could be converted to parfor for acceleration)
for idx = 1:2:(2000 * 2)
```

```
% Load the image for phase drift compensation (next image)
phaseFilename0 = sprintf('E:\\sitong\\phaseraw\\phase%05d.tif', idx + 1);
P0 = double(imread(phaseFilename0));

% Compute FFT, apply circular shifts, and mask
II0 = fftshift(fft2(P0));
II0 = circshift(II0, yShift - round(maskSize / 2), 1);
II0 = circshift(II0, xShift - round(maskSize / 2), 2);
II0 = II0 .* mask;

% Calculate the phase and intensity from the compensated image
phase1 = angle(ifft2(ifftshift(II0)));
intensity1 = abs(ifft2(ifftshift(II0)));

% Compute phase shift and intensity scaling factor
phase_shift = phase1 - phase0;
intensity_rate = sum(intensity0(:)) / sum(intensity1(:));

% Load the actual phase image to be processed
phaseFilename = sprintf('E:\\sitong\\phaseraw\\phase%05d.tif', idx);
P = double(imread(phaseFilename));

% Process the image: FFT, shift, and apply the circular mask
II = fftshift(fft2(P));
II = circshift(II, yShift - round(maskSize / 2), 1);
II = circshift(II, xShift - round(maskSize / 2), 2);
II = II .* mask;

% Recover the complex field via inverse FFT
phase_complex = ifft2(ifftshift(II));

% Resize and adjust intensity
intensity = imresize(P, [side, side], "bilinear");
intensity = (intensity - bg) * intensity_rate;

% Adjust phase by subtracting the phase shift and resize
phase = angle(phase_complex) - phase_shift;
phase = imresize(phase, [side, side], "nearest");

% Compute the complex field combining intensity and phase information
complex_field = intensity .* exp(1i * phase);

% Flatten and store the complex field in the large matrix
complexMatrix(:, k) = complex_field(:);

disp(idx);    % Display the current index for progress monitoring
k = k + 1;
```

```
end

%% Save the complex matrix for further processing or analysis
save('complexMatrix_s.mat', 'complexMatrix', '-v7.3');
toc;
```

6.1.5 Estimate Phase on SLM

```
clc;
clear;

tic;
%% Parameters and Mask Generation
interval = 50;
imageSize = 1024;    % Image size (avoiding conflict with the built-in function "size")
% Generate an alternating ring mask (assumes createRingMask is defined)
ringMask = createRingMask(interval, imageSize);

% Display the generated ring mask
figure;
imshow(ringMask, []);
title('Alternating Ring Mask');

%% Define Circular Masks for Phase Modulation
% Define ring parameters for creating circular masks
r1_inner = 0;          % Inner radius of the first ring
r1_outer = 200;        % Outer radius of the first ring
r2_inner = 200;        % Inner radius of the second ring
r2_outer = 512;        % Outer radius of the second ring
r3_inner = 320;        % Inner radius of the third ring
r3_outer = 512;        % Outer radius of the third ring

% Create coordinate grid for mask generation
[x, y] = meshgrid(1:imageSize, 1:imageSize);
center = imageSize / 2;
dist = sqrt((x - center).^2 + (y - center).^2);

% Generate circular masks
mask = (dist >= r2_inner) & (dist <= r2_outer);
% Display one of the masks (mask2) for verification
figure;
imagesc(mask2);
colormap gray;
axis image;
title('Circular Mask (mask2)');
```

```
%% Load Complex Matrix and Compute Transmission Matrix Inverse
load complexMatrix_s.mat;    % Loads variable "complexMatrix"
% Compute the effective inverse using the conjugate transpose
TM_inv = conj(complexMatrix');

%% Load Target Field and Compute Input Field
load("E_target.mat");    % Loads variable "E_target"
E_target = reshape(E_target, [256^2, 1]);
% Calculate the input field using the transmission matrix inverse
E_in = TM_inv * E_target;

%% Map the Input Field using Index Data
% Load index data (assumed variable "index_" in file "index2000.mat")
load index2000.mat;

% Initialize an empty input field (1024x1024)
inputField = zeros(imageSize);

% Map each value from E_in to its corresponding coordinate in inputField
for i = 1:2000
    % Adjust index coordinates (offset by 512)
    y_coord = index_(i, 1) + 512;
    x_coord = index_(i, 2) + 512;
    inputField(y_coord, x_coord) = E_in(i);
end

%% Compute SLM Pattern via Fourier Transformation
% Get the intensity and phase of the input field
I = abs(inputField);
P = angle(inputField);
inputField = I .* exp(1j * P);

% Compute the SLM pattern using inverse FFT with appropriate shifting
SLM = fftshift(ifft2(ifftshift(inputField)));

% Normalize the intensity of the SLM pattern
intensity = abs(SLM);
intensity = intensity / max(intensity(:));

% Calculate phase and adjust to be positive
phi = angle(SLM) + pi;

% Resize the phase pattern to match the desired SLM dimensions
phase = imresize(phi, [imageSize, imageSize], "nearest");
phase = phase / (4 * pi) * 255;

% Apply the circular mask (mask2) to the phase pattern
```

```
phase = mask .* phase;

%% Construct Final SLM Pattern Image
% Initialize a blank pattern image (1152x1920)
pattern = zeros(1152, 1920);
% Insert the phase pattern into a subregion of the final pattern image
pattern(65:1088, 449:1472) = phase;
% Adjust the pattern values and constrain them to the range [1, 250]
pattern = mod(pattern, 250) + 1;

% Save the final SLM pattern image
imwrite(uint8(pattern), 'C:\Users\Administrator\Desktop\pattern3\bessel_s.bmp');

% Save the SLM variable for further analysis
save SLM1.mat SLM
toc;
```

6.1.6 Orthogonal TM

```
clc
clear

load complexMatrix.mat
corr = complexMatrix'*complexMatrix;
corr_sum = abs(sum(corr,1));
corr_diag = abs(diag(corr));
rate = corr_diag./corr_sum;
[~, E] = sort(rate, 'descend');
E=E(:,1);
% E=randperm(7213, 2000);
save E_sort1.mat E
```

6.1.7 Z-axis focusing

```
clc;
clear;

%% Parameters
lambda = 488e-9;       % Wavelength (m)
z = 150e-6;            % Forward propagation distance (m)
k = 2 * pi / lambda; % Wavenumber

L = 100e-6;             % Simulation window side length (m)
N = 256;                 % Number of pixels (assumed square image)
dx = L / N;            % Pixel size
```

```
%% Define source plane amplitude
% Optionally, load an intensity image and derive amplitude from it.
% For now, we use a uniform amplitude distribution.
Amplitude_Uz = ones(N);

%% Define target plane amplitude (modify as needed)
Amplitude_Target = zeros(N, N);
Amplitude_Target(128-100:128+100, 128) = 65535;    % Example: vertical line with high amplitude

%% Frequency Coordinate Definition
fx = (-N/2 : N/2-1) / (dx * N);
[FX, FY] = meshgrid(fx, fx);

%% Define Propagation Transfer Functions
% Forward transfer function (angular spectrum method)
H_forward = exp(1i * k * z * sqrt(1 - (lambda * FX).^2 - (lambda * FY).^2));
H_forward((FX.^2 + FY.^2) > (1/lambda)^2) = 0;    % Zero out evanescent waves
% Backward transfer function is the complex conjugate of the forward one
H_backward = conj(H_forward);

%% Gerchberg–Saxton Algorithm Iteration
num_iter = 100;

% Initialize field at the source plane with constant amplitude and arbitrary phase
Uz = Amplitude_Uz .* exp(1i * 2 * pi * ones(N));

for iter = 1:num_iter
    % Propagate forward to the target plane
    Uz_fft = fftshift(fft2(Uz));
    U_target = ifft2(ifftshift(Uz_fft .* H_forward));

    % Impose the target amplitude constraint (keep phase)
    U_target = Amplitude_Target .* exp(1i * angle(U_target));

    % Propagate backward to the source plane
    U_target_fft = fftshift(fft2(U_target));
    Uz = ifft2(ifftshift(U_target_fft .* H_backward));

    % Impose the source amplitude constraint (keep phase)
    Uz = Amplitude_Uz .* exp(1i * angle(Uz));
end

%% Display the Recovered Phase at the Source Plane
Recovered_phase_Uz = angle(Uz);
figure;
imagesc(Recovered_phase_Uz);
axis image;
```

```
colorbar;
title('Recovered Phase at Uz');
%% Save the Final Result
E_target = Amplitude_Uz .* exp(1i * Recovered_phase_Uz);
save('E_target.mat', 'E_target');
```

6.2 Labview code

6.2.1 SLM & Camera control

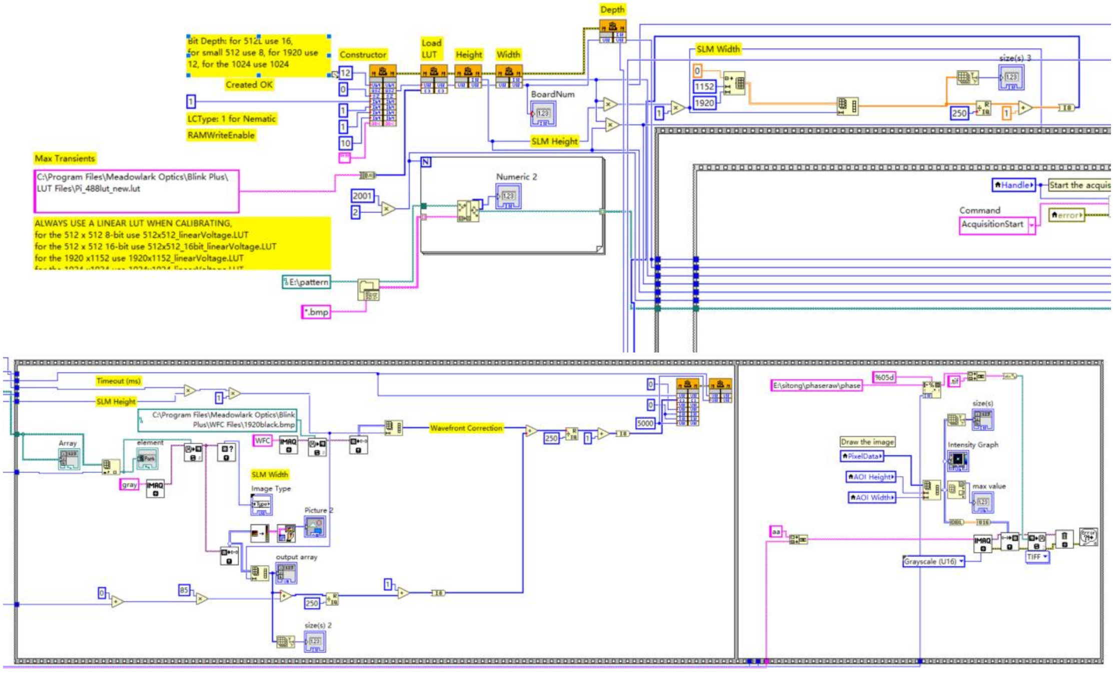
Bit Depth: for 512L use 16, for small 512 use 8, for 1920 use 12, for the 1024 use 1024

ALWAYS USE A LINEAR LUT WHEN CALIBRATING,
for the 512 x 512 8-bit use 512x512_linearVoltage.LUT
for the 512 x 512 16-bit use 512x512_16bit_linearVoltage.LUT
for the 1920 x1152 use 1920x1152_linearVoltage.LUT

C:\Program Files\Meadowlark Optics\Blink Plus\LUT Files\Pi_488lut_new.lut

C:\Program Files\Meadowlark Optics\Blink Plus\WFC Files\1920black.bmp

E:\sitong\phaseraw\phase

6.2.2 Galvo lens control

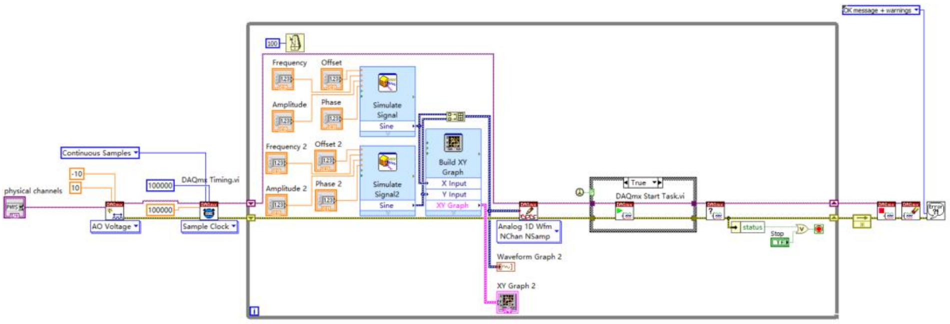

7 Acknowledgement

I would like to express my deepest gratitude to my supervisor, Professor Dayong Jin, for his patient guidance and invaluable academic support throughout my research. I am also sincerely thankful to my co-supervisors, Jiajia Zhou and Gungun Lin, for their insightful suggestions and continuous assistance.

My heartfelt thanks go to my fiancée, Dan Shao, for her unwavering support in both life and studies, as well as for providing the essential biological samples. I also greatly appreciate the support of my parents, whose encouragement has been instrumental in my academic journey.

I am indebted to my collaborators—Zhichao Yang, Xun Zhang, Chenguang Ma, and Zhiyong Guo—for their contributions and cooperation in my first project. I also wish to thank my classmates and friends, including Ming Lu, Zhichao Yang, and many others, for their camaraderie and support.

Finally, I gratefully acknowledge the institutional support provided by UTS and IBMD, which made these research possible.

8 Publication

Wu, S*., Yang, Z., Ma, C., Zhang, X., Mi, C., Zhou, J., ... & Jin, D. (2023). Deep learning enhanced NIR-II volumetric imaging of whole mice vasculature. Opto-Electronic Advances.

YANG, Z*., WU, S*., ZHANG, X., CHAO, M., LIN, G., GUO, Z., & JIN, D. (2024). Binocular Vision Fusion Enhanced 3D NIR-II in vivo Imaging of Bone and Vessel Networks. Fundamental Research.

Mi, C., Guan, M., Zhang, X., Yang, L., Wu, S., Yang, Z., ... & Yuan, X. (2022). High spatial and temporal resolution NIR-IIb gastrointestinal imaging in mice. Nano Letters, 22(7), 2793-2800.

Mi, C., Zhang, X., Yang, C., Wu, J., Chen, X., Ma, C., ... & Jin, D. (2023). Bone disease imaging through the near-infrared-II window. Nature Communications, 14(1), 6287.

Liao, J., Yang, L., Wu, S., Yang, Z., Zhou, J., Jin, D., & Guan, M. (2022). NIR-II emissive properties of 808 nm-excited lanthanide-doped nanoparticles for multiplexed in vivo imaging. Journal of Luminescence, 242, 118597.